2012-10-03

Characterization of Magneto-optical Trap For Experiments in Light-Atom Interfacing

Palittapongarnpim, Pantita

UNIVERSITY OF CALGARY

Characterization of Magneto-optical Trap

For Experiments in Light-Atom Interfacing

by

Pantita Palittapongarnpim

A THESIS

SUBMITTED TO THE FACULTY OF GRADUATE STUDIES

IN PARTIAL FULFILLMENT OF THE REQUIREMENTS FOR THE

DEGREE OF MASTER OF SCIENCE

DEPARTMENT OF PHYSICS AND ASTRONOMY

CALGARY, ALBERTA

September, 2012

Abstract

This thesis presents the study of atomic cloud density and temperature in a magneto-optical trap (MOT). The purpose is to find the method in obtaining the densest and coldest cloud the setup can produce. In steady state trap, the highest atomic density possible is that of a cloud in multiple scattering regime where a repulsive force between atoms sets a limit to the density. The number of atoms loaded into the trap is controlled by the trapping beam intensity which also changes the temperature. Therefore the trap density and temperature cannot be controlled separately. The cloud compression is studied as a method of increasing atomic density above what is possible in steady state trap without noticeable influence on the cloud temperature. Cloud compression is also found when the cloud is translated by changing the magnetic field zero-point although in a less predictable fashion than the compression.

Acknowledgments

Table of Contents

List of Tables

List of Figures and Illustrations

Chapter 1

Introduction

The concept of the magneto-optical trap (MOT) was first suggested by Jean Dalibard [1], when pioneers of the field such as Pritchard and Chu were still struggling with dipole trapping of neutral atoms. At that point, dipole traps were able to trap roughly 1000 atoms [1]. The MOT was shown to be able to trap a much higher number of atoms (on the order of 10^7 [2]), making it a preferred choice as a source of cold atoms.

A MOT uses the scattering force between photons and atoms in order to reduce the atomic momentum, effectively cooling the atoms down. The direction of the force exchanged between atom and photon is selected by tuning the frequency of the laser to be slightly red-detuned. The atom and photon can come into resonance through the Doppler effect when the atom is moving in the opposite direction to the laser propagation. This cooling mechanism is known as Doppler cooling. By introducing a linearly varying magnetic field using anti-Helmholtz coils, the scattering force varies in space due to the varying Zeeman shift. This creates a harmonic potential around the zero-point of the magnetic field which leads to trapping of atoms. The mathematical description of the trap will be provided in Chapter 2.

The MOT is a widely used technique for experiments in quantum information, as the trap can produce ultracold atomic clouds with temperatures below 100 μK [3]. In addition, the number of atoms participating in the process can be controlled using trap parameters such as the trapping beam intensity and the magnetic field gradient. The lower temperature prolongs the time the atoms remain within the same field, thus prolonging the coherence of the quantum information process. For general discussion, a longer coherence time is considered more preferable. The limit of coherence time re-

quired depends on the specific process involved. It could be microseconds – such as in information processing [4], or seconds as in optical memories [5, 6]. In experiments regarding light-atom interactions, long coherence times alone might not be beneficial if the interaction is too small to be observed. Therefore, the trap also needs to provide a large number of atoms for the experiment, as it will increase the strength of the interaction. This is not the case if the beam transverse size – and therefore the interaction region – is smaller than the cloud size. In the latter case, the atomic density is more relevant. Since having a high number of atoms in the cloud is not directly correlated with having high atomic density, the decision on whether to optimize for maximum number of atoms or atomic density depends on the application researchers have in mind.

To determine which cloud properties we will focus on in the characterization process, we have to consider the application we have in mind. A particular interest of our group is to demonstrate enhancement of optical nonlinearities. Optical nonlinearities are nonlinear interactions between light fields mediated by a material, such as second harmonic generation or self-phase modulation. The nonlinear interactions are difficult to observe in nature because of the minuscule interaction strength compared to that of linear optical phenomena such as absorption or dispersion. It is possible to observe nonlinear interactions with the use of a medium specially designed to enhance the nonlinear effects along with high power lasers with intensities of several W/cm^2. In quantum information, the level of optical power in the system is that of a few photons – often only one or two photons. One of the primary interests in the field is to create a two-photon logic gate which is required for performing universal quantum computing with photons [7]. The most sought after gate is the controlled-phase gate where the phase of one photon is shifted by π due to the presence of another photon. While this phenomenon of cross-phase modulation (XPM) has been observed, the result is far from the desired π phase shift [8]. XPM is often hindered by the absorption of the field making the result even

more obscured.

Various schemes have been developed to enhance optical nonlinearities for quantum information [9, 10, 11, 12]. Schmidt and Imamoğlu [13] proposed a scheme to create large XPM based on electromagnetically induced transparency (EIT). This scheme is shown theoretically to allow the creation of arbitrarily large XPM without the hindrance of absorption. It has been discussed that the phase shift is in fact limited by the effect of the pulse bandwidth [14] and its transverse mode [15]. This stems from an idea initially proposed by Shapiro [16, 17] which points out the role of the non-instantaneous response function in limiting the imparted phase on photon pulse. This is not to say that a large XPM close to π is impossible. This argument does not take into account enhancement of nonlinearity by using the large dipole moment of Rydberg atoms which increases nonlinear susceptibility, enhancement of field intensity, or the increase in interaction strength due to the increase in number of atoms participating in the process which also increases the susceptibility involved in the process.

The increase in field intensity can be accomplished by focusing the light beam while it travels through the medium. However, there are two major problems to this approach. Firstly, focusing a beam to the size of a micron or less, as required to achieve high intensity with single-photon beam, is technically challenging. This is because the minimum beam size at the focal point increases with decreasing numerical aperture as found in short focus lenses. Secondly, the more tightly focused the beam, the shorter the Rayleigh range, the length along the optical axis where the beam is considered to remain tightly focused. Therefore, the range where nonlinear interaction is pronounced is significantly reduced with the tightly focused beam and limits the number of atoms participating in the process.

Instead of using lens systems, one can use tapered nanofibers (TNF) as a method of focusing light. TNF are commercial fibers which are heated and pulled until the heated

region reaches a transverse size of a few hundred nanometers. The length of the tapered region can be as long as a few millimeters which is much longer than the Rayleigh length of a beam focused to the same transverse size. Since the waist of the fiber is smaller than an optical wavelength, the fiber will be surrounded by an evanescent field. This field is highly intensified compared to the input field due to the adiabatic decrease in the size of the guided mode. In the experiment by Nayak [18] *et al.* for instance, the transverse diameter of the fiber typically decreases from 120 μm to around 400 nm . EIT due to atoms interacting with the evanescent field of a TNF has been shown in hot Rubidium vapor [19], demonstrating optical nonlinearity at nanowatt optical power. The same demonstration has not yet been done with cold atoms; it has only been shown theoretically possible by Le Kien and Hakuta [20].

The intensity of the evanescent field is shown theoretically to decrease with the distance from the fiber surface and disappears within a wavelength [21, 22]. This means the interaction region between light and atoms is very small in the TNF setup. The number of participating atoms is then affected by atomic density rather than the total number of atoms. Therefore, the characteristics of the MOT cloud that we are interested in are temperature and atomic density which depend on four main parameters: trap intensity, trap detuning, magnetic field gradient, and number of atoms. Depending on the interplay between the trap parameters, the MOT cloud can exhibit different features. There are four regimes for the steady state MOT corresponding to different features of atomic density [23]. The temperature limited regime is the regime with the least number of atoms. Here, the density increases with an increasing number of atoms. The multiple scattering regime is where the atomic density becomes constant with changes in the number of atoms. The two-component regime is where the atoms spill outside the harmonic trap and form a low density cloud around the trap center. The optically-thick regime has the highest number of atoms where a large, dense cloud is formed. The last two regimes are

sometimes mentioned in the literature but not extensively discussed as a MOT generally produces a cloud in the first two regimes. A more detailed discussion for the first two regimes will be presented in Chapter 2.

One system that can produce an atomic cloud with higher density than the steady state MOT and with extremely low temperature is the Bose-Einstein Condensate (BEC). The atoms in this system share the same wave function leading to a macroscopic quantum state [24]. While this is a system with great potential in quantum information, a BEC is not necessary for demonstrating giant optical nonlinearities and the preparation of a BEC will greatly complicate our setup. We are interested in a particular technique used to prepare a high density atomic cloud called the compressed magneto-optical trap. The atoms are first collected in a trap at low magnetic field gradient, and then the cloud is compressed by increasing the gradient in steps. This technique has been reported to give transient increase in atomic density [25].

The increase in the number of participating atoms in the atom-light interaction due to the transient compression can be estimated by considering the TNF system. Let the radius of the fiber be a_0 with the penetration depth of the evanescent field being a. The length of the tapered region (region in which the fiber waist can be approximated as a_0) is assumed to be much longer than the cloud radius r. Assuming that the intensity of the evanescent field is azimuthally symmetric, the volume where the field intersects with the atomic cloud is given by $V = 2\pi(a^2 - a_0^2)r$. This leads to the number of participating atoms being $N = n \cdot 2\pi(a^2 - a_0^2)r$, where n is the atomic density. The ratio between the number of atoms in the volume during compression N_2 and the number in steady state N_1 is

$$\frac{N_2}{N_1} = \frac{n_2}{n_1}\frac{r_2}{r_1}.$$

(1.1)

We note here that this ratio does not depends only on the ratio between the atomic

densities but also ratio between the sizes of the cloud. It will not be the case if the tapered region is smaller than the cloud size. In that case, the ratio between the number of participating atoms will only depend on the atomic density. Therefore, the evaluation or discussion of the result pertaining towards its use with atom-light interaction will always depend on the geometry of the system. In this thesis, I will use the TNF model discussed here in order to evaluate the experimental results.

The dependence on model is also true for the evaluation of preferable cloud temperature, or rather the averaged velocity. This is because the coherence time of a process is limited by either the time the atoms spend in the light beam or the coherence time of the excited state which is the fundamental limit of an atomic system. The worst case scenario is where an atom escape using the shortest path between the fiber surface and the edge of the evanescent field. This distance is the transverse distance $a - a_0$. We only need the atoms to evolve coherently within the beam. Therefore, the atoms can decay right at a which corresponds to an atom of velocity $v = (a - a_0)\Gamma$, where Γ is the decay rate of the transition. If this is the average velocity of the ensemble, the preferable temperature of the ensemble corresponding to this velocity is $T = \frac{m}{k_B}(a - a_0)^2\Gamma^2$. Again, this estimation is according to our model of the system. For other systems, the preferable cloud temperature will be different.

The rest of my thesis is detailed as follows. After reviewing the relevant theories in Chapter 2, I will describe the setup and the methods used in the experiment in Chapter 3. In Chapter 4, I will show the experimental results of three major parts of the characterization. In the first part, I explore the trap parameter space available in our setup and show how different parameters of the MOT affect atomic density and cloud temperature. The result includes the transition of the MOT cloud from the temperature limited to the multiple scattering regimes where the atomic density is the highest in a steady state trap. The density in this regime has been reported to be on the order of

roughly 10^{10}cm^{-3} [26] and often not more. The temperature of the cloud is shown to increase with the trap intensity. In the second part, I investigate the compressed MOT as a way to transiently increase the atomic density while not significantly affecting the temperature. In the third part, I will investigate the translation of the cloud by moving the zero-point of the magnetic field. This allows the cloud to be formed outside the influence of the TNF as the fiber significantly alters the shape and temperature of the cloud [27, 28]. Appendix A will be used to describe the basics of atom-light interaction and the forces on the atom. The result of this appendix will be used throughout the theoretical discussion of the MOT.

Chapter 2

Magneto-Optical Trap

The main cooling mechanism of the MOT is Doppler cooling which uses the Doppler effect to shift red-detuned light fields into resonance with atoms that are moving in the opposite direction of the field propagation. By incorporating a linearly varying field from an anti-Helmholtz coil, a harmonic trap can be formed to obtain a cloud of millions of atoms. The temperature of the cloud, however, can be lower than the limit predicted by Doppler cooling. The observation of sub-Doppler temperature by Lett *et. al.* [3] led to the discovery of an additional cooling mechanism called polarization gradient cooling, and it is now widely used to describe the phenomenon.

A steady state MOT has different regimes of operation where the cloud shows different features. The most widely discussed are the temperature limited regime and the multiple scattering regime. The properties of the cloud in these two regimes are quite well-known, although most relations are described in semi-empirical forms due to the complexity of the system. I will describe the common knowledge in the field regarding these two regimes and specifically how the atomic density and temperature behave.

Since the maximum atomic density of a steady state MOT cloud is limited to what is achievable in the multiple scattering regime, I will also investigate a technique to achieve densities beyond this limit. The compressed magneto-optical trap is a technique used to prepare high density clouds for BECs by increasing the magnetic field gradient after a steady state MOT is achieved. The effect of a change in magnetic field gradient to steady state clouds, as observed and discussed in literature, will be reviewed in this chapter and used as a baseline for the discussion of transient behavior during compression in Chapter 4.
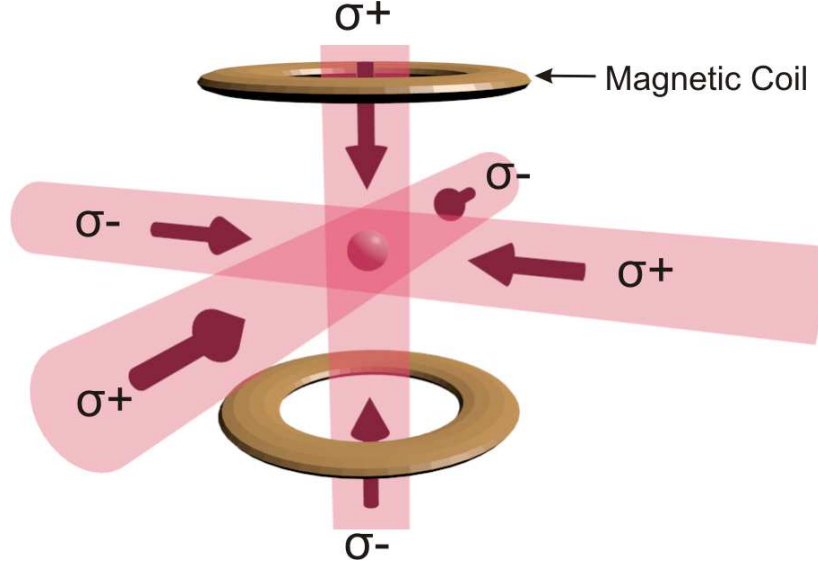
Figure 2.1: Schematic of magneto-optical trap. The bronze rings represent the magnetic field coils in an anti-Helmholtz configuration. The white ball in the middle represents the atomic cloud. The pink stripes are the laser beams arranged in counterpropagating pairs of mutually orthogonal polarization.

2.1   Overview: Conceptual Description of the MOT

In order to trap a large ensemble of atoms, the atoms need to be cooled and confined to a specific location. In a MOT, the momentum of an atom is modified by exchanging momentum with photons through resonant scattering. Since the photons scatter into random directions, the average momentum transferred over several cycles is largely in the direction of the cooling laser.

The MOT setup consists of three pairs of counterpropagating red-detuned laser beams arranged in three perpendicular directions as shown in Fig. 2.1. The polarization of each pair is chosen to have mutually orthogonal polarization. In our setup, the polarizations are σ_+ and σ_- which allow atoms to transition into Zeeman sublevels with the change of $\Delta m = 1$ and $\Delta m = -1$, respectively. Without the magnetic field, these beams only create friction forces since they will come into resonance with atoms that are moving in the opposite direction of the wave's propagation and thus decelerate those atoms.

Therefore, the configuration is known as an optical molasses. This cooling process is called Doppler cooling due to the use of the Doppler effect in decelerating the atoms.

To apply position-specific forces and create a trap, the magnetic coils are set in an anti-Helmholtz configuration creating a magnetic field zero-point at the center of the crossing beams with linearly varying magnetic field. The varying magnetic field shifts the magnetic sublevels depending on the position of the atom. The one-dimensional scheme in Fig. 2.2 use the $F = 0 \rightarrow F' = 1$ as an example. The magnetic field shifts the excited sublevel $m = +1$ closer to the ground state when the magnetic field is in the negative direction which is when $z < 0$. This will bring the atom closer to resonance with the σ_+ beam which has a positive k-vector. The Doppler effect will brings the atom with $v < 0$ into resonance with the beam and push the atom towards the center of the trap. A similar mechanism happens at $z > 0$ to atoms of $v > 0$. Therefore, the atom will always be pushed back towards the zero-point, and a cold atomic cloud is formed at the center. A detailed discussion of the cooling and trapping force will be addressed in Section 2.2.

For real atoms, there are generally many hyperfine levels F, where $\hat{\mathbf{F}} = \hat{\mathbf{I}} + \hat{\mathbf{J}}$ as discussed in Section A.1, which can be chosen to be the ground state. The transition of interest to this work, the D_2 transition of Rubidium 87, has two hyperfine levels $F = 1$ and $F = 2$. The atoms can decay into any of the F levels with the probabilities dictated by the Clebsch-Gordan coefficients. The trapping transition is chosen to be $F = 2 \rightarrow F' = 3$ with the majority of the atoms decaying back to their original states since it is a cyclic transition, allowing the atoms to be addressed by the trapping beams for many consecutive cycles. A small portion of the atoms will decay into the dark state $F = 1$ which is not addressed by the trapping laser. These atoms will experience no trapping forces and eventually escape. To keep the trap from losing atoms, this level is addressed by another field called the repumping field whose function is to excite the
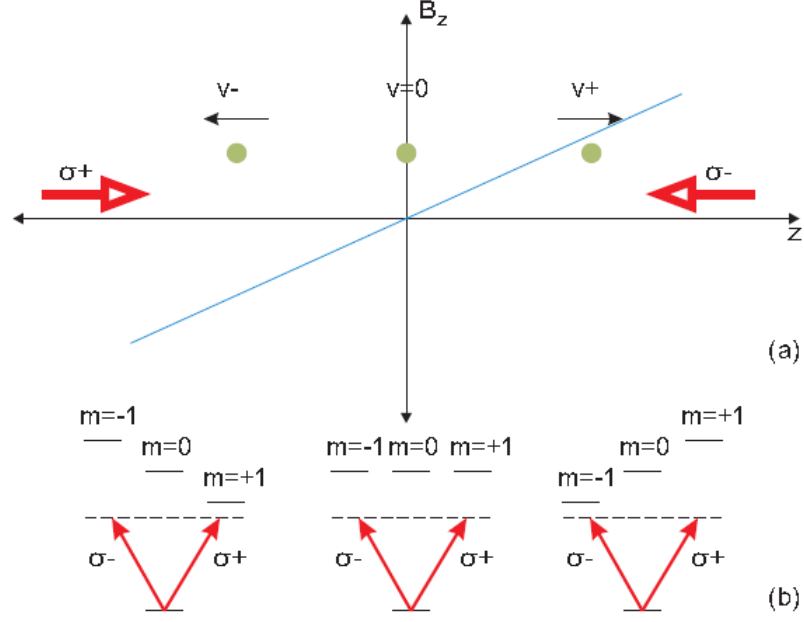
Figure 2.2: (a) Conceptual schematic for a one-dimensional trap. The blue line is the magnetic field strength B_z. (b) The magnetic sublevels of $F = 0$ (ground state) and $F' = 1$ (excited state) in various positions along z-axis.

atoms in the dark state to $F' = 3$ and let them decay back into $F = 2$ where they will be cooled and trapped.

2.2 Cooling and Trapping Mechanisms

The main cooling mechanism, as stated previously, is Doppler cooling. Combined with the Zeeman shift of the magnetic sublevels, the Doppler effect also provides the trapping force. There is also an additional cooling mechanism at the center of the trap called polarization gradient cooling which allows us to cool the atomic ensemble below the limit of Doppler cooling. The mechanism of this additional cooling force depends on the polarization of the light field and the internal structure of the atomic species.

2.2.1 Doppler Cooling and Trapping

We will first consider how the presence of the magnetic field shifts the magnetic sublevels. For the purpose of illustrating the trapping force we will consider the force on axis of an anti-Helmholtz coil. Since the magnetic field changes linearly in space around the magnetic field zero-point, we can describe our field as $B_z = \frac{\partial B_z}{\partial z} z$.

An atom in a magnetic field **B** will experience Zeeman energy splitting due to the interaction between the atom's magnetic moment and the magnetic field. This interaction is described by the Hamiltonian $-\vec{\mu} \cdot \mathbf{B}$, where $\vec{\mu}$ is the total atomic magnetic moment. Following the description in [29], the total magnetic momentum is defined to be, $\vec{\mu} = \mu_B(g_l\hat{\mathbf{L}} + g_s\hat{\mathbf{S}} + g_I\hat{\mathbf{I}})$ where $\hat{\mathbf{L}}$ is the orbital angular momentum operator, $\hat{\mathbf{S}}$ is the spin, and $\hat{\mathbf{I}}$ is the nuclear spin. Therefore, this Hamiltonian signifies the coupling of the magnetic field to the total angular momentum. The strength of this coupling is governed by the Bohr magneton $\mu_B = e\hbar/2m_{\text{electron}}$ and the Landé g-factors g_i.

In a MOT, the states participating in the trapping process are the magnetic sublevels m_F of the same hyperfine level F. The magnetic field is generally very weak at the center; i.e. the Zeeman splitting due to the external field is smaller than the hyperfine splitting. The magnetic Hamiltonian is approximated to be $\hat{H}_B = \mu_B g_F \hat{F}_z B_z$ [29]. The first-order energy shift calculated from time-independent perturbation theory is $\Delta E_{F,mF} = \mu_B g_F m_F B_z$. Values of g_F, which is a combination of g_l, g_s, g_I and l, s, F, can be found in Ref. [30] for rigorous calculations.

When considering a transition between two levels, we have to take into account that both levels are shifted by the magnetic field. Therefore, the energy shift for a particular transition is the difference between the energy shifts for individual levels introduced by the Zeeman splitting:

$$\Delta E_{F',mF'} - \Delta E_{F,mF} = (g_{F'}m_{F'} - g_F m_F)\mu_B \frac{\partial B_z}{\partial z} z. \qquad (2.1)$$

To illustrate the workings of the MOT, we use the hypothetical transition of $F = 0 \rightarrow F' = 1$. These hyperfine levels have one and three magnetic sublevels respectively. Following the setup illustrated in Fig. 2.2, the detuning to the level $m_{F'} = +1$ will decrease only if $z < 0$ while the opposite is true for $m_{F'} = -1$. Since $m_F = 0$ and $g_{F'}$ for all $m_{F'}$ are the same [30], we can write the frequency shift as

$$\Delta\omega_0 = m_{F'}\frac{g_{F'}\mu_B}{\hbar}\frac{\partial B_z}{\partial z}z = m_{F'}\beta z \tag{2.2}$$

with $\beta = \frac{g_{F'}\mu_B}{\hbar}\frac{\partial B_z}{\partial z}$.

The Doppler shift in frequency comes from the atomic velocity along the axis of the wave's propagation. If the atom is at rest, the electromagnetic wave at its position is $\mathbf{E} = \vec{\mathcal{E}}_0\cos(\omega t)$. If the atom moves at velocity $\mathbf{v}$, the field in the atomic frame becomes $\mathbf{E} = \vec{\mathcal{E}}_0\cos(\omega t - \mathbf{k}\cdot\mathbf{r}_{atom}) = \vec{\mathcal{E}}_0\cos\left((\omega - \mathbf{k}\cdot\mathbf{v})t\right)$. Therefore, $\mathbf{k}\cdot\mathbf{v}$ is the frequency shift due to the Doppler effect.

For a stationary atom with resonance frequency ω_0, the detuning between the light field and the atomic resonance is $\Delta = \omega - \omega_0$. Incorporating both the Doppler and Zeeman shift, the description of total detuning becomes $\Delta_d = \Delta - \mathbf{k}\cdot\mathbf{v} + m_{F'}\beta z$. For each dimension of the trap, we have two counterpropagating beams of polarization σ_+ and σ_- with $\mathbf{k}_\pm$ signifying the propagation direction of each beam. We assume the two beams to be perfectly counterpropagating, that is $\mathbf{k}_- = -\mathbf{k}_+$ and $|\mathbf{k}_+| = |\mathbf{k}_-| = k$ as they have the same wavelength. In our scheme, a particular atom of velocity $\mathbf{-v}$ will come into resonance with the σ_+ beam which addresses the $m_F = +1$ level when it is in the $-z$ position. Therefore, the detuning in the atomic frame for the σ_+ beam is $\Delta_{d+} = \Delta + kv + \beta z$. Similarly, the very same atom will observe the σ_- beam having the detuning of $\Delta_{d-} = \Delta - kv - \beta z$.

The force responsible for cooling is the scattering force as discussed in Appendix A

which has the form

$$\mathbf{F}_{\sigma\pm}(\Delta_d) = \hbar\mathbf{k}_\pm\frac{\Gamma}{2}\left(\frac{\Omega^2/2}{\Delta^2 + (\Gamma/2)^2 + \Omega^2/2}\right). \tag{A.22}$$

where $\Omega = d\mathcal{E}_0/\hbar$ is the Rabi frequency, and Γ is the decay rate of the transition. Along a pair of counterpropagating beams, the total force is the sum of the scattering force due to the σ_+ and σ_- beam:

$$\begin{aligned}\mathbf{F}_{\mathrm{MOT}} &= \mathbf{F}_{\sigma+}(\Delta_{d+}) + \mathbf{F}_{\sigma-}(\Delta_{d-})\\ &= \hbar\mathbf{k}_+\frac{\Gamma}{2}\left(\frac{\Omega^2/2}{\Delta_{d+}^2 + (\Gamma/2)^2 + \Omega^2/2}\right) + \hbar\mathbf{k}_-\frac{\Gamma}{2}\left(\frac{\Omega^2/2}{\Delta_{d-}^2 + (\Gamma/2)^2 + \Omega^2/2}\right).\end{aligned} \tag{2.3}$$

Since the energy shift due to Doppler effect and Zeeman effect is small ($\beta z + kv \ll \Delta$), we find the first order approximation using Taylor series expansion [29, 31]. The force will have linear dependence on these frequency shifts and takes the form of

$$F_{\mathrm{MOT}} = -\hbar k\Gamma\Delta\frac{\Omega^2/2}{(\Delta^2 + (\Gamma/2)^2 + \Omega^2/2)^2}(\beta z + kv). \tag{2.4}$$

By defining $\alpha = -2\hbar k^2\Gamma\Delta\frac{\Omega^2/2}{(\Delta^2+(\Gamma/2)^2+\Omega^2/2)^2}$ which is positive for red-detuned field, we can write the force on an atom in the MOT as

$$F_{MOT} = -\alpha|v| - \kappa|z| \tag{2.5}$$

where $\kappa = \frac{\alpha\beta}{k}$. This force takes the same form as that in a damped harmonic oscillator. The friction term $-\alpha v$ is the cooling force while the harmonic term $-\kappa z$ creates the trap.

The force on other axes can be derived in the same fashion with the possibility of having different magnetic field gradients (the axial gradient is half that on the axis) and trapping beam intensities (hidden in the Rabi frequency Ω). This means the cooling force might not be the same along the x, y and z axes. There is also heating of the atoms, partly due to spontaneous emission which gives rise to equal heating in all directions. Therefore, the average velocity of the cloud $\langle v_i^2\rangle$ along a particular dimension can vary

14

from dimension to dimension under the competition between cooling and heating. Because of the anisotropic velocity components, it is more beneficial for characterization purposes to define the temperature for each dimension separately with $\langle v_i^2 \rangle$, rather than with the average speed over three dimensions $\langle v^2 \rangle$. This definition of temperature is not equivalent to the thermodynamic definition but is a commonly used jargon which is used to put the result of the cooling into perspective with a usual atomic gas. It also makes keeping track of the changes in the cloud due to the changes in parameters easier, and therefore this will be the definition we use throughout this thesis.

2.2.2 Doppler Limit

The limit to Doppler cooling is estimated by considering the ensemble in steady state of energy exchange. Since the trapping mechanism does not cool, only the friction term is taken in account. The cooling force in one dimension of the trap is $-\alpha \mathbf{v}$ where $\mathbf{v}$ is assumed to be on the axis of field propagation. The energy that is used to cool the atom is equal to the work on the atom from the friction force:

$$E\big|_{\text{cooling}} = \mathbf{F} \cdot \mathbf{r}. \tag{2.6}$$

The cooling rate is the derivative of Eq. (2.6). If the force is taken to be constant over an infinitesimal time period, the cooling rate is

$$\frac{dE}{dt}\bigg|_{\text{cooling}} = \mathbf{F} \cdot \mathbf{v} = -\alpha v^2. \tag{2.7}$$

In the steady state, the cooling rate is equal to the heating rate. There are two processes that contribute to the heating of the atomic cloud: one is spontaneous emission which adds random momentum in three dimension to the ensemble, and the other is fluctuations in the number of absorbed photons as pointed out in Ref. [31].

To calculate the heating rate, we will first calculate the change of $\langle v_i^2 \rangle$ with time. For an ensemble of atoms under the influence of a light field, the spontaneous emission comes

form the population in the excited state $\rho_{ee} = \frac{1}{2}\frac{(\Omega)^2/2}{(\Gamma/2)^2+\Delta^2+2(\Omega)^2/2}$ (Eq. (A.20)) and occurs at the rate of Γ. Assuming the the intensity of the field is small such that $\Omega \ll \Gamma$, the excited state population in a MOT is six times more populated than it would have been under the influence of one beam. Each emission gives a random velocity kick $\mathbf{v}_{rec} = \hbar\mathbf{k}/m$ to the atom which is distributed equally over three dimensions. Therefore, the change in $\langle v_i^2 \rangle$ for just one dimension is

$$\frac{d\langle v_i^2 \rangle}{dt}\bigg|_{scat} = \frac{6v_{rec}^2\Gamma\rho_{ee}}{3} \tag{2.8}$$

$$= 2v_{rec}^2\Gamma\rho_{ee} \tag{2.9}$$

as derived in Ref. [32]. The 6 corresponds to the number of beams. The 3 corresponds to the number of dimensions the fluorescence photons are scattered into.

The other source of heating is the fluctuations in the number of scattered photon. Since the process is random, the momentum transferred to the atom in any given period of time will have a variance. C. J. Foot reasons in Ref. [31] that this randomness is due to the laser having random number of photons. Therefore, the variance of the momentum transferred also follows the same statistics as the laser.

Since a laser has Poissonian photon statistics, the variance in photon number of the laser beam is $\text{Var}(N_p) = N_p$ where N_p is the average number of photons in the laser field. The change in $\langle v_i^2 \rangle$ during the time dt is

$$d\langle v_i^2 \rangle = v_{rec}^2\text{Var}(N_p) = v_{rec}^2 N_p. \tag{2.10}$$

The average number of photons interacting with the atoms can be written as $N_p = \Gamma\rho_{ee}dt$. There are two beams equally participating in the scattering which leads to a variance of $2N_p$ and a change in $\langle v_i^2 \rangle$ as follows:

$$\frac{d\langle v_i^2 \rangle}{dt}\bigg|_{abs} = v_{rec}^2 2\Gamma\rho_{ee} \tag{2.11}$$

16

The total heating rate can be found by adding the heating rate from both processes

$$
\begin{aligned}
\left.\frac{dE}{dt}\right|_{\text{heating}} &= \frac{1}{2}m \left.\frac{d\langle v_{\text{i}}^2 \rangle}{dt}\right|_{\text{scat}} + \frac{1}{2}m \left.\frac{d\langle v_{\text{i}}^2 \rangle}{dt}\right|_{\text{abs}} \\
&= 2mv_{\text{rec}}^2 \Gamma \rho_{\text{ee}} \\
&= \frac{\hbar^2 k^2 \Gamma}{m} \frac{\Omega^2/2}{\left(\Gamma/2\right)^2 + \Delta^2 + \Omega^2/2}
\end{aligned}
\tag{2.12}
$$

In steady state, the cloud is also in thermal equilibrium. There is no net heat transfer, and therefore

$$
\left.\frac{dE}{dt}\right|_{\text{cooling}} + \left.\frac{dE}{dt}\right|_{\text{heating}} = 0
\tag{2.13}
$$

Substituting the cooling and heating rate, $\langle v_{\text{i}}^2 \rangle$ can be found from

$$
\begin{aligned}
\alpha \langle v_{\text{i}}^2 \rangle &= \frac{\hbar^2 k^2 \Gamma}{m} \frac{\Omega^2/2}{\Delta^2 + (\Gamma/2)^2 + \Omega^2/2} \\
\langle v_{\text{i}}^2 \rangle &= \frac{\hbar}{2m} \frac{\Delta^2 + (\Gamma/2)^2 + \Omega^2/2}{|\Delta|}
\end{aligned}
\tag{2.14}
$$

for $\Delta < 0$. This expression is only valid if the laser is red-detuned; i.e., the light cools the atoms. While heating from spontaneous emission remains the same for any dimension we wish to examine, if the trapping beam intensity varies from dimension to dimension, the average velocity in a dimension will be different. We find the temperature using the equipartition theorem which leads to the relation: $k_B T/2 = m \langle v^2 \rangle/2$. Thus the condition for steady state temperature is

$$
T = \frac{\hbar}{2k_B} \frac{\Delta^2 + (\Gamma/2)^2 + \Omega^2/2}{|\Delta|}.
\tag{2.15}
$$

In case of low intensity where $\Omega \ll \Gamma$, $\Omega^2/2$ is negligible, and the minimum temperature occurs at $\Delta = -\Gamma/2$ (negative sign coming from the red-detuning). This gives us the limit of Doppler cooling:

$$
T_{\text{D}} = \frac{\hbar \Gamma}{2k_B}.
\tag{2.16}
$$

17

2.2.3 Polarization Gradient Cooling

It was reported in 1988 by Lett *et. al.* [3] that a cloud with sub-Doppler temperature could be obtained from a MOT which led to a discovery of additional cooling mechanisms. This was confirmed and explained by Jean Dalibard and Claude Cohen-Tannoudji a year later [33] and collectively called polarization gradient cooling. It should be noted here that there are other suggested mechanisms such as in Refs. [34, 35, 36]. I choose to present only polarization gradient cooling as it is the most widely accepted explanation.

There are two distinct mechanisms in polarization gradient cooling which happen in different settings, and both result from polarization changes in space. The first, and more frequently discussed, is Sisyphus cooling which happens in a MOT with counter-propagating linearly polarized light. The other does not have any specific name and appears in the system of counterpropagating circularly polarized light. Although we use the spin-orbit state throughout this discussion following the derivation in Ref. [33], the same procedure can be applied to the hyperfine levels.

Sisyphus Cooling

In the case where the counterpropagating fields are orthogonally linearly polarized, we write the total electric field as

$$\mathbf{E}_{\text{total}}(z,t) = \frac{\vec{\mathcal{E}}^+(z)}{2}\exp\{-\imath\omega t\} + c.c. \tag{2.17}$$

where $\vec{\mathcal{E}}^+(z) = \mathcal{E}_0\vec{\epsilon}_x\exp\{\imath kz\} + \mathcal{E}_0'\vec{\epsilon}_y\exp\{-\imath kz\}$. The beam with $\vec{\epsilon}_x$ polarization propagates in the positive direction, and $\vec{\epsilon}_y$ polarization beam propagates in the negative direction. If the two beams have exactly the same amplitude, the superposition of the electric fields is

$$\mathbf{E}_{\text{total}} = \frac{\mathcal{E}_0}{\sqrt{2}}\left(\frac{\vec{\epsilon}_x + \vec{\epsilon}_y}{\sqrt{2}}\cos(kz) + \imath\frac{\vec{\epsilon}_x - \vec{\epsilon}_y}{\sqrt{2}}\sin(kz)\right)\exp(\imath\omega t) + c.c. \tag{2.18}$$

The helicity of the field polarization changes between linearly polarized and circularly polarized depending on the position. For a state with only one ground state sublevel – for instance, $J_g = 0$ – the dynamics of the atomic states under the influence of the light field will not be perturbed by the change in polarization since the atoms always decay back to the same ground state. If the ground state is $J_g = 1/2$, which has two magnetic sublevels, the two sublevels will experience different Stark shifts at different positions in space. For example, at $z = 0$, the atoms are under the influence of linearly polarized light, and the ground state sublevels are degenerate. The population of the atoms are equally distributed over the sublevels. At $z = \lambda/8$, the polarization of the field becomes σ_-. Under this field, the $m_g = -1/2$ sublevel is shifted by $-\Omega^2/4\Delta$ as a result of the AC-Stark shift [31] while $m_g = 1/2$ is shifted by $+\Omega^2/4\Delta$. The different shifts between the energy sublevels cause a redistribution of atomic population to have more atoms in $m_g = -1/2$. At $z = \lambda/4$, the polarization returns to linear, and the two sublevels are degenerate once again. This pattern continues in a sinusoidal fashion over space, creating potential hills with alternating crests and troughs for $m_g = -1/2$ and $m_g = 1/2$ as shown in Fig. 2.3.

An atom in a particular ground state sublevel moving in this sinusoidal potential will be like a ball moving up and down a set of hills. An atom going up a hill loses kinetic energy by converting it to potential energy which it regains when rolling down hill. If the atom is interrupted while moving up the hill by being excited to another level, it will continue moving along the same path but no longer subjected to the change in potential energy. If we take the transition from $J_g = 1/2 \rightarrow J_e = 3/2$, we can see from Fig. 2.3 that an atom in the $m_g = -1/2$ sublevel will be excited by the $\sigma+$ beam at the top of its potential hill. This will take it to the $m_e = 1/2$ sublevel of the excited state. The Clebsh-Gordon coefficient of the transition favors a decay into the $m_g = 1/2$ state. If timed correctly, the atom will decay into the trough of the $m_g = 1/2$ potential, releasing
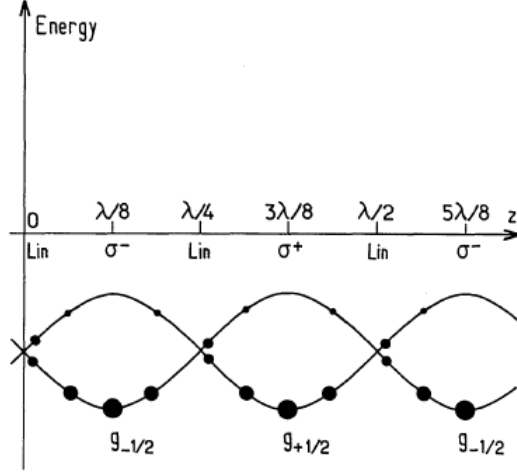
Figure 2.3: AC-shifted ground state energy levels (lines) and populations (dots) for $J_g = 1/2$ in lin $\perp$ lin configuration and its variation along z-axis as shown in Ref. [33]. The labels at the bottom indicate the ground state that is at the lowest energy at the particular position.

any potential energy gained from climbing the $m_g = -1/2$ hill into the fluorescence photon. Therefore, the kinetic energy the atom once possessed is reduced by the process.

In order for this process to work efficiently, the velocity of the atom must be such that the excitation always happens when the atom is climbing up hills. This limits the range of atomic velocities that can be significantly affected by Sisyphus cooling. To find the velocity that maximizes this process and subsequently find the order of magnitude of the friction coefficient, we define $\tau_p = 1/\Gamma'$ as the time the atom takes to be transferred between ground state sublevels which have a maximum energy separation of Δ'. The maximum energy dissipated from the process is then $\hbar\Delta'$. In order to have the highest efficiency, the atom must travel from the potential trough to the nearest crest which is $\lambda/4$ away in the time τ_p before decaying into a potential minimum of the other sublevel. Therefore, the maximum friction force will occur if

$$
\begin{aligned}
v\tau_p &= \lambda/4 \\
v &= \frac{\lambda\Gamma'}{4}.
\end{aligned}
\tag{2.19}
$$

20

The power dissipated is

$$\begin{aligned} P &= \frac{\hbar\Delta'}{\tau_p} \\ &= \hbar\Delta'\Gamma'. \end{aligned} \tag{2.20}$$

Assuming the friction force to take the form $F = -\alpha'v$, the power dissipated is

$$P = -\mathbf{F}\cdot\mathbf{v} = -\alpha'v^2. \tag{2.21}$$

Comparing Eq. (2.20) and Eq. (2.21), we find the friction coefficient α':

$$\begin{aligned} \alpha' &= -\frac{\hbar\Delta'\Gamma'}{v^2} \\ &= -\frac{16\hbar\Delta'}{\lambda^2\Gamma'} \\ &\sim -\hbar k^2\frac{\Delta'}{\Gamma'} \end{aligned} \tag{2.22}$$

The energy separation between the ground state sublevels is estimated by using the energy shift between the ground and the excited state due to AC-Stark shift which is $\delta = \Omega^2/2\Delta$. Γ' is stated in Ref. [33] to have the form $\Gamma' \sim \Omega^2\Gamma/\Delta^2$ which leads to

$$\alpha' \sim -\hbar k^2\frac{\Delta}{\Gamma} \tag{2.23}$$

A more rigorous calculation using quantum mechanics yields the friction coefficient of Ref. [33]

$$\alpha' = -3\hbar k^2\frac{\Delta}{\Gamma}. \tag{2.24}$$

This additional cooling allows the temperatures of the clouds to to drop below the Doppler limit as it increases the friction coefficient while it does not change the heating process. However, the limit to this cooling has been observed to be inconsistent with theoretical derivation. The actual limit and some possible causes of this discrepancy will be discussed in Section 2.2.4.

Polarization Gradient Cooling in σ_+/σ_- Configuration

In the case where the two beams are circularly polarized, the superposition of the fields leads to $\vec{\mathcal{E}}^+(z) = \mathcal{E}_0\vec{\epsilon}_{\sigma+}\exp\{\imath kz\} + \mathcal{E}_0^*\vec{\epsilon}_{\sigma-}\exp\{-\imath kz\}$ with polarization vectors

$$\vec{\epsilon}_{\sigma+} = -\frac{1}{\sqrt{2}}(\vec{\epsilon}_x + \imath\vec{\epsilon}_y) \tag{2.25}$$

$$\vec{\epsilon}_{\sigma-} = \frac{1}{\sqrt{2}}(\vec{\epsilon}_x - \imath\vec{\epsilon}_y). \tag{2.26}$$

The σ_+ beam is propagating in the positive direction, and the σ_- beam is propagating in the negative direction. The total field is

$$\mathbf{E}_{\text{total}} = \left(\frac{\mathcal{E}_0' - \mathcal{E}_0'}{2\sqrt{2}}[\vec{\epsilon}_x\cos(kz) - \vec{\epsilon}_y\sin(kz)] - \imath\frac{\mathcal{E}_0' + \mathcal{E}_0}{2\sqrt{2}}[\vec{\epsilon}_x\sin(kz) + \vec{\epsilon}_y\cos(kz)]\right)\exp\{-\imath\omega t\} + c.c. \tag{2.27}$$

In the case where the amplitude of the two counterpropagating waves are equal, as in the MOT, the first term in Eq. (2.27) disappears. The polarization becomes linear with rotating direction along the z-axis. Without the change in helicity in space, Sisyphus cooling no longer applies. The atomic frame in this case will be moving with the velocity of the atoms and rotating such that the polarization of the light is constant. The rotation of this frame is also governed by the speed of the atom. Since the polarization rotates around the z-axis, the rotation operator is $\hat{T}(t) = \exp\{-\imath kvt\hat{J}_z/\hbar\}$, kvt being the phase gained with time, and J_z is the atom's total angular momentum. This transformation is proven to bring $\mathbf{d}\cdot(\vec{\epsilon}_x\sin(kz) + \vec{\epsilon}_y\cos(kz))$ to simply $\mathbf{d}\cdot\vec{\epsilon}_y$ with a result of adding another term of $H_{\text{add}} = kv\hat{J}_z$ to the usual atom-light Hamiltonian stated in Eq. (A.4).

The eigenstates of the atom-light interaction, disregarding H_{add}, can be found by choosing the $\vec{\epsilon}_y$ in the rotating frame to be the quantization axis. For the purpose of illustrating the process, we will assume that the transition is $J = 1 \rightarrow J = 2$ which has three ground state sublevels as discussed in Ref. [33]. The energy of these levels are shifted from the unperturbed states by the presence of the field. The $m_g = 0$ level has the lowest energy with a Stark shift of Δ_0'. The $m_g = -1$ and $m_g = 1$ levels are equally shifted by

22

the linear polarized light by Δ_1' which can be expressed in terms of Δ_0'. The eigenstates of the ground states are denoted as $|g_i\rangle_y$ where y signifies the quantization axis. The eigenstate of the full Hamiltonian, including H_{add}, can be calculated using the first order approximation of time-independent perturbation theory with H_{add} as the perturbation term. The eigenstates from this approximation are $|\bar{g}_i\rangle_y = |g_i\rangle_y + \sum_{k \neq i} \frac{kv_y\langle g_k|J_z|g_i\rangle_y}{\hbar(\Delta_{ik}')}|g_k\rangle_y$ where Δ_{ik}' is the energy difference between ground state i and k which can be found in terms of Δ_0' by calculating the Stark shift.

While the eigenstates of $|\bar{g}_1\rangle_y$ and $|\bar{g}_{-1}\rangle_y$ are equally shifted, $|\bar{g}_1\rangle_z$ and $|\bar{g}_{-1}\rangle_z$ are not. The asymmetry can be checked by calculating $\langle J_z\rangle$; if $\langle J_z\rangle = 0$, then the state is symmetrical. The calculation shows that $\langle J_z\rangle = \frac{40}{17}\frac{\hbar kv}{\Delta_0'}$ [33] leading to a population imbalance in the z-dimension of

$$
\begin{aligned}
\Pi_{+1} - \Pi_{-1} &= \frac{\langle J_z\rangle}{\hbar} \\
&= \frac{40}{17}\frac{kv}{\Delta_0'}
\end{aligned}
\tag{2.28}
$$

where $\Pi_i = \langle\bar{g}|\bar{g}_i\rangle_z$ is the state population. The friction force associated with this imbalance is

$$
\hbar k(\Pi_{+1} - \Pi_{-1})\Gamma' = \frac{40}{17}\frac{\hbar k^2\Gamma'}{\Delta_0'}v
\tag{2.29}
$$

where $\hbar k\Gamma'$ is the force of one photon. This imbalance has direct dependence on the velocity of the atom. If $v > 0$, the state $m_g = -1$ has higher population ($\Delta_0' < 0$ since the laser is red-detuned). The force in this case is negative due to the favored exchange of momentum between the atoms in $m_g = -1$ and σ_- beam by the Clebsh-Gordon coefficients, and the atoms are pushed in the opposite direction of their velocities. A similar process happens for atoms moving in the $v < 0$ direction. Therefore, the mechanism gives rise to a cooling force.

For an order of magnitude calculation with $\Gamma' \sim \Gamma$ and $\Delta_0' \sim \frac{\Omega^2}{\Delta}$, the friction coefficient

is

$$\alpha' = -\frac{40}{17}\frac{\hbar k^2 \Gamma \Delta}{\Omega^2}.$$

(2.30)

A more rigorous calculation using quantum mechanics in Ref. [33] shows that the force does not in fact depend on the amplitude of the field. The actual friction coefficient is in fact

$$\alpha' = \frac{120}{17}\frac{-\Delta\Gamma}{5\Gamma^2 + 4\Delta^2}\hbar k^2.$$

(2.31)

The fact that the force depends on the population imbalance poses restrictions to the ground states in which this phenomenon can be observed. The atoms must have ground state sublevels that allow for population imbalance through optical pumping, and therefore needs at least three magnetic sublevels to operate.

Polarization Gradient Cooling in More Than One Dimension

The treatments described previously are for a one dimensional trap since we have discussed before that each dimension of the trap can have different strengths of the cooling force making the trap condition nonisotropic. It also allows us to reduce greatly the complexity of the derivation. This reduction has a great flaw when it comes to describing polarization gradient cooling as the mechanism depends on the change of polarization in space due to interference of the trapping beams. In one dimension, we assume the beams to perfectly counterpropagate which results in a field that has either varying helicity or a rotating linear polarization. In a more realistic case, the beams are slightly misaligned; i.e., $\mathbf{k}_-$ is not perfectly $-\mathbf{k}_+$. The resulting polarization is now much more complicated because $|\mathbf{k}_- \cdot \hat{\mathbf{k}}_+|$ is no longer k. For example, the polarization of the σ_+/σ_- configuration will no longer be a rotating linear polarization such as when the amplitude of the fields are equal. This effect can be minimized by adjusting the alignment.

A more complicated scenario happens when two or more dimensions are taken into account. Even with perfect alignment, the interference between the two or three pairs of

beams will produce various degrees of polarization helicity depending on (1) the phase difference between each pair of trapping fields ϕ_{ij}, for i, j being the dimension, and (2) the position inside the field. This allows Sisyphus cooling to exist even in a trap with σ_+/σ_- configuration. The strength of the force depends on the light shift of the ground state sublevels which is related to the helicity of the total light field. It has been shown by Mølmer in Ref. [37] for the case of linearly polarized optical molasses that the change in helicity can create an average friction force that depends on ϕ_{ij}. Steane *et.al.* numerically showed that small misalignment of the beam can cause interference patterns in the atomic distribution. Similar to the case of Sisyphus cooling in one dimension, the amount of Stark shift varies with helicity of the field polarization in the three dimensional case. In ideal case, the variation will be that of sinusoidal pattern with the period of $\pi/2$. If one of the beam is misaligned, the Stark shift is shown to have a beat pattern [38]. The varying Stark shift translates into varying 'stickiness' in the molasses causing varying rates of atomic diffusion inside the trap. This leads to an interference pattern in the atomic distribution which is also observable in the MOT.

2.2.4 Temperature Limit of Polarization Gradient Cooling

The MOT clouds have been known to reach temperatures approaching the recoil limit [3]. This limit is where we assume the momentum of the atom is equal to that of a fluorescence photon. For every cooling or trapping scheme that involves constant photon scattering, this is the fundamental limit of the trap temperature.

Using the relationship between temperature and kinetic energy of the atom from equipartition theorem $\frac{1}{2}k_B T_{\text{recoil}} = \frac{p^2}{2m}$ where p is the momentum of a fluorescence photon, the recoil limit is

$$T_{\text{recoil}} = \frac{\hbar^2 k^2}{2k_B m}. \tag{2.32}$$

A theoretical derivation of this limit from polarization gradient cooling is attempted

in Ref. [33] using the method discussed in Ref. [39]. The method yields a result that does not fit with the experimental observation. This is probably because the calculation is based on a one-dimensional cooling force. A calculation for the limit of a higher dimension trap was attempted in Ref. [37]. They used the semi-classical model for the light-atom interaction and therefore cannot obtain the recoil limit. To the best of my knowledge, this limit is imposed with no connection to the nature of the cooling force.

2.3   Steady State MOT

The characteristics of a MOT cloud, such as the size of the cloud and the atomic density, depend strongly on the cloud's regime. There are four distinct regimes for a steady state cloud. The easiest way to picture the cloud's transition between these regimes is to keep the trapping conditions constant and consider only a change in the number of trapped atoms. The regimes are as follows:

1. The temperature limited regime is the regime where the cloud has the least number of atoms. This is where all the mechanisms of cooling and heating previously discussed hold.

2. The multiple scattering regime is where the cloud has become dense enough that a significant portion of fluorescence photons are re-absorbed by the atoms in the trap. The re-scattering results in a repulsive force between atoms, limiting the atomic density in this regime.

3. The two-component regime is where the number of atoms is too high to be packed into the harmonic part of the trap and the atoms spill out into the shallower potential well around the harmonic trap. The approximation of the trap as a damped harmonic oscillator no longer holds. The cloud

will appear to have two different density components with the denser part residing inside the harmonic potential.

4. The optically dense (or optically thick) regime is where the shallow part of the trap is also filled. It has the highest number of atoms of the four regimes.

A MOT cloud is most often reported to be in either temperature limited or multiple scattering regime. Therefore, we will disregard the two-component and the optically thick regimes and focus the discussion on the properties of the cloud in these two regimes.

The properties of the cloud depend on four main parameters, but they also depend on the beam alignment, the beam intensity profile, and the background pressure from hot atoms. An imperfection in beam alignment can reduce the trapping and cooling forces. Any non-uniformity in the transverse intensity causes the trap condition to change from position to position. Collisions with hot atoms affect the trap lifetime which in turn affects the number of atoms in the steady state trap. In the following discussions, the trap is assumed to have perfect alignment and perfectly uniform intensity profile. The experimental results still follow the trends predicted by theory but might not match quantitatively.

2.3.1 The Forces

The distinction between the temperature limited and the multiple scattering regime is a difference in the forces involved. In the temperature limited regime, the forces are simply the trap forces calculated in previous sections. Assuming spherical symmetry over the trap for simplicity, the force in the radial direction is $F_r(r, v_r) = -\alpha v_r - \kappa r$.

The cloud in the multiple scattering regime has two additional forces due to the cloud having higher atomic density than in the temperature limited regime. One is a repulsive

photon-pressure force due to the re-scattered trapping field. The other is an attractive force due to an attenuation of the trapping beam intensity as it passes through. To derive the expression for the force, we first consider an atom at position $\mathbf{r}'$ scattering photons from the laser beam with scattering rate

$$\mathcal{R}_{scat} = \frac{\Gamma}{2}\left(\frac{\Omega^2/2}{\Delta^2 + (\Gamma/2)^2 + \Omega^2/2}\right). \tag{A.22}$$

These scattered photons fly off in every direction. Another atom at position $\mathbf{r}$ with a cross-section for re-absorbing photons σ_R will see the photon flux Φ_{photon} described by

$$\Phi_{photon} = \frac{\Gamma}{2}\left(\frac{\Omega^2/2}{\Delta^2 + (\Gamma/2)^2 + \Omega^2/2}\right)\frac{\sigma_R}{4\pi|\mathbf{r} - \mathbf{r}'|^2}. \tag{2.33}$$

The total force due to re-scattering experienced by the atom at $\mathbf{r}$ is the sum of the forces contributed by every atom in the ensemble which can be written as [40]

$$\mathbf{F}_R = \hbar k \frac{\Gamma}{2}\left(\frac{\Omega^2/2}{\Delta^2 + (\Gamma/2)^2 + \Omega^2/2}\right)\frac{\sigma_R}{4\pi}\int n(\mathbf{r}')\frac{\mathbf{r} - \mathbf{r}'}{|\mathbf{r} - \mathbf{r}'|^3}dr'^3 \tag{2.34}$$

where $n(\mathbf{r}')$ describes the spatial distribution of the atoms in the cloud. The form of the force here is similar to the electrostatic force experienced by an electron inside an insulator filled with negative charges. This force satisfies the inverse-square law and has a divergence of $\nabla \cdot \mathbf{F}_R = \hbar k \frac{\Gamma}{2}\left(\frac{\Omega^2/2}{\Delta^2 + (\Gamma/2)^2 + \Omega^2/2}\right)\frac{\sigma_R}{4\pi}n(\mathbf{r})$ [40], indicating an outward component. Assuming the cloud to have spherical symmetry and uniform atomic density, we can use Gauss's Law to calculate the force at a distance r from the center of the trap.

Despite the similarity, there is a major distinction between the electrostatic force and the photon-pressure force. Unlike the electrostatic force, the photon-pressure force needs a mediator – the optical photon – to make the momentum exchange. Therefore, the receiving atom will experience a force coming from one atom at a time. This is different from the electrostatic force in which the electron experiences the net force contributed by all charges at all times. Using this argument, we can write a simplified form of the

28

photon-pressure force force on an atom residing at r as

$$\begin{aligned}
\mathbf{F}_R &= \hbar k \frac{\Gamma}{2} \left(\frac{\Omega^2/2}{\Delta^2 + (\Gamma/2)^2 + \Omega^2/2} \right) \frac{\sigma_R}{4\pi r^2} \hat{\mathbf{r}} \\
&= \frac{I\sigma_L}{c} \frac{\sigma_R}{4\pi r^2} \hat{\mathbf{r}}
\end{aligned} \tag{2.35}$$

where $\sigma_L = \frac{\hbar\omega}{I} \frac{\Gamma}{2} \left(\frac{\Omega^2/2}{\Delta^2 + (\Gamma/2)^2 + \Omega^2/2} \right)$ is the laser scattering cross-section.

Generally, σ_R is larger than σ_L or else the effect of the photon-pressure force will be shadowed by another attractive force due to attenuation of the trapping beam. This force is calculated in Ref. [40] as being a result of the shadow in the laser cast by the atoms. The final form of the force is

$$\mathbf{F}_A = -\frac{I\sigma_L^2}{c4\pi r^2} \hat{\mathbf{r}}. \tag{2.36}$$

The extra forces found in the multiple scattering regime have the combined form of

$$\mathbf{F}_R + \mathbf{F}_A = \frac{I\sigma_L^2}{c4\pi r^2} \left(\frac{\sigma_R}{\sigma_L} - 1 \right). \tag{2.37}$$

According to Ref. [38], the calculation for the explicit form of σ_R has to take two scattering process into account: elastic scattering (Rayleigh scattering) with a scattering cross section of σ_L, and inelastic scattering (fluorescence) which has a scattering cross-section of photon at resonance σ_{L0}. The scattering cross section of the inelastic part can be written in terms of σ_L as

$$\begin{aligned}
\sigma_{L0} &= \frac{\hbar\omega\Gamma}{2I} \left(\frac{\Omega^2/2}{\Omega^2/2 + \Gamma^2/4} \right) \\
&= \sigma_L \left(\frac{\Delta^2 + \Gamma^2/4 + \Omega^2/2}{\Omega^2/2 + \Gamma^2/4} \right).
\end{aligned} \tag{2.38}$$

The ratio between the intensity of elastic I_{el} and total scattering intensity $I_{\text{total}} = I_{\text{el}} + I_{\text{inel}}$ is calculated by Mollow [41] to be

$$\frac{I_{\text{el}}}{I_{\text{total}}} = \frac{\Delta^2 + \Gamma^2/4}{\Delta^2 + \Gamma^2/4 + \Omega^2/2}. \tag{2.39}$$

29

This ratio leads to a total re-scattered intensity of

$$
\begin{aligned}
I_{\text{input}}\sigma_R &= I_{\text{input}}\frac{I_{\text{el}}}{I_{\text{total}}}\sigma_L + I_{\text{input}}\left(1 - \frac{I_{\text{el}}}{I_{\text{total}}}\right)\sigma_{L0} \\
\sigma_R &= \frac{I_{\text{el}}}{I_{\text{total}}}\sigma_L + \left(1 - \frac{I_{\text{el}}}{I_{\text{total}}}\right)\sigma_{L0} \\
&= \frac{I_{\text{el}}}{I_{\text{total}}}\sigma_L + \left(1 - \frac{I_{\text{el}}}{I_{\text{total}}}\right)\left(\frac{\Delta^2 + \Gamma^2/4 + \Omega^2/2}{\Omega^2/2 + \Gamma^2/4}\right)\sigma_L
\end{aligned}
\tag{2.40}
$$

which gives

$$
\frac{\sigma_R}{\sigma_L} - 1 = \left(\frac{\Omega^2/2}{\Omega^2/2 + \Delta^2 + \Gamma^2/4}\right)\left(\frac{\Delta^2}{\Omega^2/2 + \Gamma^2/4}\right).
\tag{2.41}
$$

This equations shows us that $\sigma_R > \sigma_L$ as mentioned before. We replace $\frac{\sigma_R}{\sigma_L} - 1$ in Eq. (2.37) with Eq. (2.41) whenever we want to calculate the strength of the additional forces in multiple scattering regime.

2.3.2 Capture Velocity

When the trap is first turned on for the first time in the day, the initial cloud is very faint. Given time, the MOT will be slowly filled up with more atoms and the cloud becomes brighter, although no parameters in the trap has changed. Some time is needed to cool the hot atoms from hot Rubidium gas to the capture velocity. The capture velocity is defined to be the velocity of an atom entering the trap that can be decelerated to zero when the atom reaches the center of the trap [38]. This is only a convenient definition which gives an estimate without the need for complicated calculations or simulations of the actual dynamics of the atoms.

A more mathematical definition can be derived by imagining an atom entering a trap of radius r_0 with kinetic energy $\frac{1}{2}mv_c^2$. The atom will experience a cooling force from its point of entry to the center of the trap. In Ref. [38], the cooling force is defined to be half the maximum scattering force, or $\hbar k\Gamma/4$, which corresponds to a work of $\hbar k\Gamma r_d/4$ done on the atom. Since the atom comes to a stop at the center of the trap, conservation of energy

dictates that the work done on the atom is equal to the atom's initial kinetic energy. Therefore, $v_c = \sqrt{\hbar k \Gamma r_d / 2m}$ which corresponds to a temperature (for one dimension) of $T_c = \hbar k \Gamma r_d / 2k_B$. This temperature is used as a measure of trap depth and is not the temperature of the cloud. The trap depth is an estimate of the highest temperature of the hot atoms that the trap can capture. A very rough estimation using our trap parameters shows $T_c = 15K$, much lower than the room temperature, which is the reason why the atoms must be left to cool before it can be properly trapped. Because the scattering force is a dispersive force which cannot be described as a potential, capture velocity is sometimes a preferred measurement to the trap depth [26].

2.3.3 Number of Atoms and Trap Lifetime

The change in the number of atoms inside the trap is due to three mechanisms: loading of the trap, loss due to collision with background atoms, and loss due to collision with other trapped atoms. The equation for the number of trapped atoms follows the approximation [38]

$$\frac{dN}{dt} = R - \frac{N}{\tau} - \beta \frac{N^2}{V}. \tag{2.42}$$

The first term R is the loading rate of trap. This quantity will not be discussed in detail here due to its complex dependence on several parameters such as background pressure, trapping beam intensity, trap volume, alignment, detuning, etc. The second term, which is the first order loss term, is the loss due to collisions with hot atoms and usually dominates the losses in a typical MOT. The trap lifetime τ gives an estimate of the time an atom spend in the trap. The third term is due to the internal collisions and depends on density. This term is negligible in a MOT because the density is usually not high enough to offset β. Therefore, the equation for the change in number of atoms with time is

$$\frac{dN}{dt} = R - \frac{N}{\tau}. \tag{2.43}$$

The solution to this inhomogeneous differential equation is

$$N(t) = N_0(1 - \exp\{-t/\tau\}) \tag{2.44}$$

where $N_0 = R\tau$ is the steady state number of atoms. The trap's loading profile is governed by τ which gives us the convenience of measuring the trap lifetime.

2.3.4 Cloud Radius and Atomic Density

In the temperature limited regime, the force in the trap is that of a damped harmonic oscillator. Although we do not usually assign a potential to the trap due to the dissipative damping force, the harmonic term can be considered to be a result of a harmonic potential which gives rise to the relation between the cloud radius and the temperature due to equipartition theorem

$$\frac{1}{2}\kappa_r \langle r^2 \rangle = \frac{1}{2}k_B T. \tag{2.45}$$

This indicates that in the first regime the size of the cloud depends only on the temperature and not on the number of atoms in the trap. Hence, the atomic density is proportional to the number of trapped atoms given that the spring constant κ remains unchanged. The spring constant is different for different directions even in the ideal case where the intensity of all trapping beams are equal, since the magnetic field gradient on the transverse plane is half that of the gradient on the axis. In this case, the shape of the cloud is more like that of a pumpkin with $r_T \equiv r_z = r_{x,y}/\sqrt{2}$. This yields an average atomic density of

$$n = \frac{3N}{\pi(2r_T)^3}. \tag{2.46}$$

If we assume the cloud to have spherical symmetry for simplicity of further discussion, then

$$n = \frac{3N}{4\pi r_T^3}. \tag{2.47}$$

In the multiple scattering regime, the radius is no longer determined by the temperatures of the cloud but rather by the number of atoms in the trap as a result of having repulsive forces between atoms at higher trap densities. Ignoring the cooling term as it no longer determines the trap size, the density of the cloud in steady state is such that the trapping force balances the repulsive forces given by Eq. (2.37). We assume the cloud to have spherical symmetry for simplicity. For an atom at distance r from the trap center, with N atoms residing within a sphere of radius r, the total force on the atom is

$$\sum F(r) = -\kappa r + N \frac{I \sigma_L \sigma_R}{c 4 \pi r^2} - N \frac{I \sigma_L^2}{c 4 \pi r^2} = 0. \tag{2.48}$$

With some algebra, Eq. (2.48) leads to an average atomic density of

$$n = \frac{N}{4/3 \pi r^3} = \frac{3 c \kappa}{I \sigma_L^2} \frac{1}{(\sigma_R / \sigma_L - 1)}. \tag{2.49}$$

The density in this regime no longer depends on the number of atoms, only on the spring constant and trapping intensity. Therefore, the more atoms in the trap the larger the cloud.

The different behaviors of the atomic density in the temperature limited regime and multiple scattering regime give us a convenient and readily observable way to distinguish between the two regimes.

2.3.5 Temperature

The temperature of the MOT cloud is determined from the average speed of the trapped atoms. However, this is under the assumption that the cooling and trapping forces in all dimensions are the same. As discussed in Section 2.2.1, the forces can be different for different dimensions due to the difference in the friction coefficient α. Therefore, each dimension is subject to its own trap parameters. For the purpose of characterizing the trap, each dimension will be treated separately so as to not obscure the degree of change in one dimension by the other.

To simplify the following discussion, we think of the trap as having symmetry in all directions. For small clouds, i.e. those in the temperature limited regime, the magnetic field can be considered negligible. Therefore, the temperature should not depend on the magnetic field gradient – similar to optical molasses. Neglecting polarization gradient cooling for the moment, the steady state temperature of the cloud follows Eq. (2.15) which is often written as Eq. (2.50)

$$k_B T = \hbar \frac{\Delta^2 + (\Gamma/2)^2 + \Omega^2/2}{|\Delta|} \tag{2.15}$$

$$\frac{k_B T}{\hbar \Gamma} = \frac{1}{2} \frac{\Omega^2}{|\Delta|\Gamma} + \frac{1}{2} \frac{(2\Delta/\Gamma)^2 + 1}{2|\Delta|/\Gamma} \tag{2.50}$$

In reality, polarization gradient cooling can play a significant part in determining the cloud temperature and render Eq. (2.50) incomplete. However, polarization gradient cooling does not depend on the trapping beam intensity. This can be seen from the friction coefficients given by Eq. (2.24) and (2.31). Therefore, the presence of polarization gradient cooling should not affect the scaling of the temperature with trapping beam intensity. Due to the complexity in mathematically incorporating the effect of polarization gradient cooling into the derivation, Eq. (2.50) is generally stated in semi-empirical form:

$$\frac{k_B T}{\hbar \Gamma} = C_{\sigma+/-} \frac{\Omega^2}{|\Delta|\Gamma} + C_0 \tag{2.51}$$

where $C_{\sigma+/-}, C_0$ is found by performing linear regression on the experimental data. The validity this equation is shown in experimental results in Refs. [42, 43]. $C_{\sigma+/-}$, which is the constant for Doppler cooling, depends on detuning in a real MOT [43]. In that reference, the temperature is also shown to increase with magnetic field gradient at the gradient of below 1 G/cm before it reaches a plateau. This has been associated with the change in atomic density in the multiple scattering regime because the size of the cloud in this regime depends on the number of atoms. Therefore, the cloud can be large enough that the effect of the magnetic field cannot be ignored any longer. It was also observed in

Ref. [44] where the gradient is on the order of a hundred G/cm that the temperature of the cloud will decrease due to a decrease in capture velocity. The effect of the magnetic field gradient on the temperature will be discussed in more detail in Section 2.4.1.

2.4   Compressed Magneto-optical Trap

Some applications of the MOT, such as the preparation of BECs and atomic ensembles for cold collisions, require atomic densities that are higher than the $\approx 10^{10} \text{cm}^2$ normally obtained in the steady state MOT. One well-known technique is called the dark MOT. It is similar to an ordinary MOT with the repumping laser being blocked at the center of the trap, which allows the atoms to go into a dark state. Without being constantly excited and de-excited, there is no photon pressure to limit the atomic density and therefore allows the dark MOT to obtain high atomic densities. However, without the atoms being actively cooled this can limit how cold the cloud can be. It was shown that a steady state dark MOT works well for smaller atoms [45] but not for heavy alkalis such as cesium [46]. This is because the center of the trap, which generally provides polarization gradient cooling, is not used. A common technique for creating a dark MOT is to shut off the center of the repumping laser after a steady state MOT has been achieved. In this case, the atoms in the center region of the trap are already sufficiently cooled and will maintain high density and low temperature.

Implementation of a dark MOT is not necessary if a transient increase in density is what we are interested in. A transient compression by increasing the magnetic field gradient has been demonstrated by Petrich *et.al.* [25] in a regular MOT. A similar procedure is applied to the dark MOT in Ref. [47]. This is a very attractive alternative as it does not require any modification of the setup aside from an electronic control to allow instantaneous and arbitrary change to the coil current.

2.4.1   Magnetic Compression

To obtain a high atomic density with this method, we start with a trap at a low gradient which allows more atoms to be loaded. Once the trap is in its steady state, the magnetic field gradient is increased to compress the trap. To interpret the result, we will first discuss the theory and observation of the steady state MOT with a change in magnetic field gradient.

Atomic Density and Regime Transition

The steady state density and its response to the change in field gradient are different for the temperature limited and multiple scattering regimes. For the temperature limited regime, the density is $n_{\text{TL}} = \frac{3N}{4\pi r_T^3} = \frac{3N}{4\pi} \frac{\kappa^{3/2}}{(k_B T)^{3/2}}$ (Eq. (2.47)) while the multiple scattering regime has a density of $n_{\text{MS}} = \frac{3c}{I\sigma_L^2} \frac{\kappa}{(\sigma_R/\sigma_L - 1)}$ (Eq. (2.49)). The density in the temperature limited regime is more sensitive to the change in spring constant than the multiple scattering. Equating the density gives us the value of κ at which the change in regime occurs.

$$\kappa^{1/2} = \frac{4\pi c}{N I \sigma_L^2} \frac{(k_B T)^{3/2}}{(\sigma_R/\sigma_L - 1)}. \tag{2.52}$$

If at any point the trap compression requires the change of κ above this value, the trap will transition from the temperature limited to the multiple scattering regime. It is possible that the transient increases in atomic densities observed in [25, 47] are a result of crossing this limit.

Trap Depth and Temperature

The trapping force in a MOT will be extended up to the position where the Zeeman shift is comparable to the detuning; i.e., $\mu_B \frac{\partial B_z}{\partial z} r_d \approx \hbar |\Delta|$ [44]. The distance from the center

of the trap to a such point is written as a function of the trap parameters

$$r_d \approx \frac{\hbar |\Delta|}{\mu_B} \frac{\partial B_z}{\partial z}^{-1}$$
$$\approx \frac{\Delta \alpha}{k \kappa}. \tag{2.53}$$

As discussed in Ref. [44], this radius is approximated under the assumption that the laser beams are infinitely large; therefore, the volume where all the six beams cross is also infinitely large. In reality, the laser beams have finite sizes which defines the spatial limit from the trapping force. A simple calculation using parameters from our MOT ($\Delta = -15$ MHz, $\frac{\partial B_z}{\partial z} = 10$ G/cm) gives $r_d \approx 0.95$ cm which is slightly smaller than the 1.25 cm expected from the trapping beam. Given that the transverse intensity profiles usually tapers out significantly before they reach 1.25 cm, r_d can be approximated as the radius of the beam. For higher magnetic field gradients which yield r_d smaller than the beam radius, the trap depth is determined by r_d, and this gives the trap potential of $U_c = \frac{\hbar k \Gamma}{4} r_d = \frac{\hbar \Gamma}{4} \frac{\alpha \Delta}{\kappa}$ corresponding to $T_c = \frac{\hbar \Gamma}{2 k_B} \frac{\alpha \Delta}{\kappa}$. On the other hand, a reduction in magnetic field gradient widens the trapping area as can be seen from Eq. (2.53). If r_d is larger than the beam radius, the trap depth is $U_c = \frac{\hbar k \Gamma}{4} L$ where L is the radius of the beam corresponding to $T_c = \frac{\hbar k \Gamma}{2 k_B} L$. According to this estimation, the increase in magnetic field gradient will not affect the trap depth until $r_d \leq L$.

The reduction in trap depth implies that the temperature of the atomic cloud decreases with the increase in gradient. It also implies that less atoms will be loaded into the trap as the velocity of the atom that can be trapped is reduced. At high gradient, a drastic decrease on loading rate is reported in Ref. [48]. The reduction in trap depth is also used to obtain a single atom MOT in [44] by using a gradient of 350 G/cm. Another way of reducing the trap depth is by reducing the beam size as used in Ref. [49] to trap a single atom.

Chapter 3

Experimental Setup and Methods

A MOT setup was previously built in our lab for the propose of demonstrating EIT in a cloud of a few atoms. In that stage, we did not have instantaneous control of trap parameters, such as the trapping beam intensity, the trapping beam detuning, the magnetic field gradient, and the number of atoms. Control of these parameters is necessary for characterization of the MOT cloud. For this reason, the setup has been modified to provide the control necessary for measurements to be performed on the cloud. In this chapter, I will first detail the setup, the components we use, and their functions. I will also briefly describe the optimization process before measurements can be performed. I will end this chapter with a description of the methods for measuring the number of atoms, the cloud radii, and the temperatures. These are the methods used in characterizing the MOT for every experiment to follow.

3.1 Components of Experimental Setup

3.1.1 Atomic Species and Transitions

The atomic species used in the experiment is Rubidium 87 with the D_2 transition ($F = 2 \rightarrow F' = 3$) used as the trapping transition. This corresponds to an optical wavelength of 780.246 nm. This is also a cyclic transition with a small probability of atoms de-exciting into the dark state $F = 1$. We address this with a repumping laser set to the $F = 1 \rightarrow F' = 3$ transition, corresponding to 780.232 nm, in order to pump the atoms back to $F = 2$. These transitions are shown in Fig. 3.1

Detailed information on the D_2 transition including Clebsch-Gordan coeffecients can

be found in Ref. [30]. I recap the crucial information in Table 3.1.

Properties	Symbol	Value
Mass	m	$1.44316060(11) \times 10^{-25}$ kg
D_2 Decay Rate/ Natural linewidth	Γ	$2\pi \times 6.065(9)$ MHz
D_2 Doppler Temperature	T_D	$146 \ \mu$K
Dipole Moment $\sigma^\pm$	$d_{(m_F=\pm2\rightarrow m_{F'}=\pm3)}$	$2.534(3) \times 10^{-29}$ C $\cdot$ m
Saturation Intensity $\sigma^\pm$	$I_{sat(m_F=\pm2\rightarrow m_{F'}=\pm3)}$	$1.669(2)$ mW/cm^2
Resonant Cross Section $\sigma^\pm$	$\sigma_{0(m_F=\pm2\rightarrow m_{F'}=\pm3)}$	2.907×10^{-9}cm^2

Table 3.1: Rubidium 87 Properties
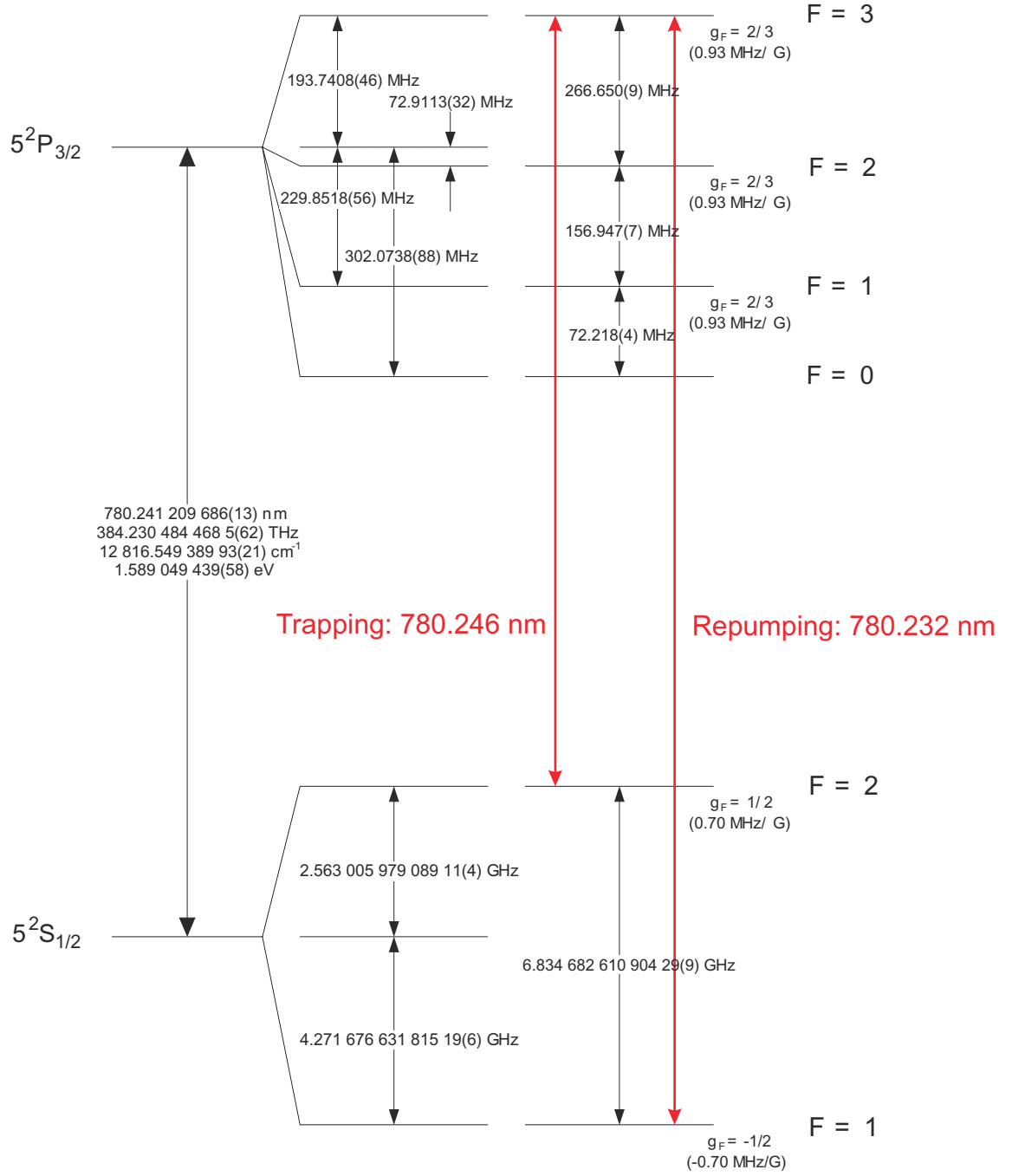
Figure 3.1: Energy levels of Rb^{87} D_2 transition as shown by Steck [30] with the trapping and repumping transitions.
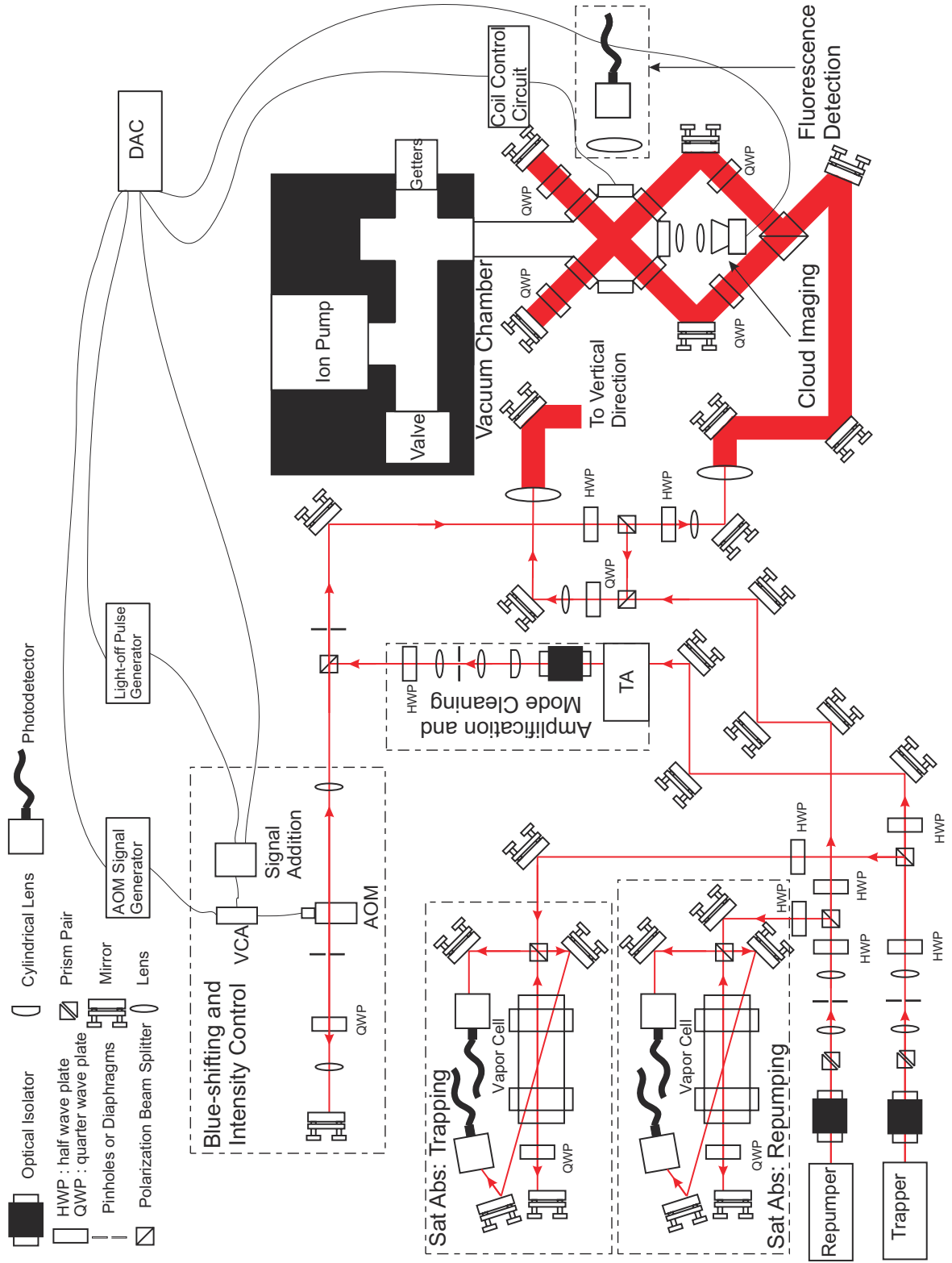
Figure 3.2: Schematic of experimental setup.

41

3.1.2 Optical Components

External Cavity Diode Lasers

Both our repumping laser and trapping laser are diode lasers from homemade units (principle of design described in Ref. [50]). The temperature and the current are regulated by Thorlabs ITC102 units which have both a proportional-integral-derivative (PID) temperature controller and a current limiting circuit. Temperature sensors (AD590) are attached in the diode housings to provide reading for the PID controllers, which in turn control the current going through Peltier elements to cool or heat the diode. The output of the diodes are incident on diffraction gratings to create an external cavity, allowing tunability of laser frequency by adjusting the optical feedback into the diode. Coarse frequency selection is done by adjusting two screws, one located directly behind the grating for horizontal angle control and the other, attached to the platform underneath the grating, for vertical angle control. The horizontal screw is also connected to a piezoelectric element which allows scanning of the laser frequency over a GHz range. The scan range is generally limited by the mode-hop-free range. The piezo signal is provided by a homemade controller circuit generating a ramping signal of roughly 60 V range (adjustable). Diode current and temperature can also be used to tune the frequency of the laser. The zeroth-order diffraction from the grating is reflected off a mirror to the output port while the first-order is reflected back into the diode to provide optical feedback.

Saturated Absorption Spectroscopy

Since the cooling and trapping forces are sensitive to detuning from the atomic transitions, the range of detuning in which a MOT cloud can be formed is limited to about -20 MHz. A frequency locking circuit is needed to prevent the trapping laser from drifting. The laser frequency can be electronically locked to a particular transition using an absorption profile. In a hot gas system, the absorption line is broadened due to the
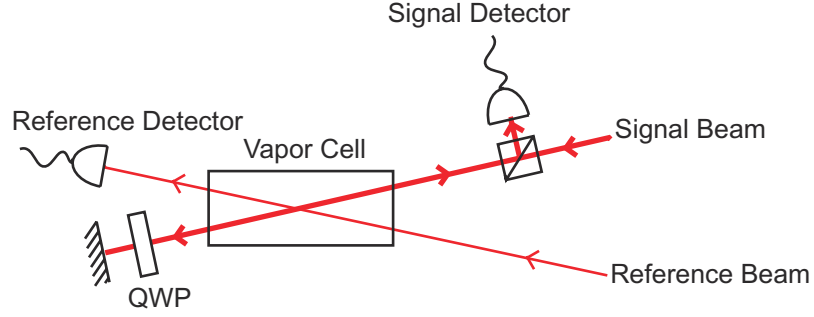
Figure 3.3: Schematic of saturated absorption spectroscopy as used in setup (Fig. 3.2). Two beams are injected into the hot vapor cell at an angle with one another. The absorption profile is detected by the reference detector after a single passing to provide reference of the Doppler broadening. The other beam is retro-reflected, passing through a quarter-wave plate twice which changes the beam polarization from horizontal to vertical. The outgoing beam is reflected off a polarizing beam splitter, allowing separation between incoming and outgoing beam, and the saturated absorption profile is detected from the outgoing port.

Doppler effect resulting in a broadened linewidth causing a loss in frequency resolution.

To counter the effect of Doppler broadening, we use saturated absorption spectroscopy to better resolve the hyperfine lines. This technique is done by passing a laser beam through a hot vapor cell, then reflecting it back along the same path. Each beam on its own will be in resonance with a set of velocity groups. If a velocity group can be addressed by both, it will absorb the forward beam which has a more intense component around the transition frequencies. This creates a transparency window for the back-reflected beam.

Given the counterpropagating configuration, there are two types of velocity groups that can be addressed by both beams. The first is $v = 0$, which will be addressed by the resonance frequencies of the hyperfine transitions. The second is the velocity group that brings the light field into resonance (ω_1) of a transition through red-shift while being in resonance with another transition (ω_2) through blue-shift. In this case there is a velocity group that gives $\omega = \omega_1 + kv$ and $\omega = \omega_2 - kv$ simultaneously, creating a transparency at the frequency $\omega = \frac{\omega_2 - \omega_1}{2}$ between two resonances. The width of these transparencies is determined by hole burning (reduction of the ground state population due to a strong

43
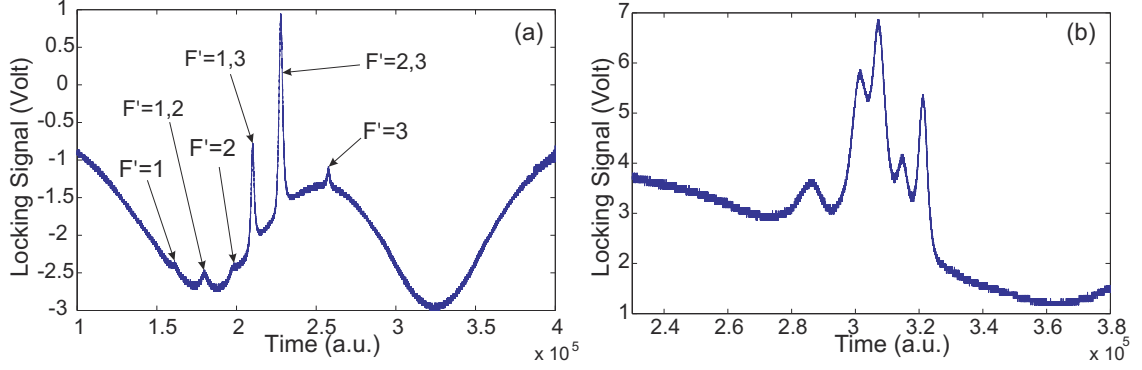
Figure 3.4: Saturated absorption signal from D_2 transition. (a) is the $F = 2 \to F'$ (trapping beam). (b) is the $F = 1 \to F'$ (repumping beam).

pump beam) and is given by [31]:

$$\Delta\omega_{hole} = \Gamma \left(1 + \frac{I}{I_{sat}}\right)^{1/2} \tag{3.1}$$

where I is the intensity of the pump beam and $I_{sat} = \frac{\pi}{3} \frac{\hbar c \Gamma}{\lambda^3} = 2 \left(\frac{\Omega}{\Gamma}\right)^2$ as defined in Appendix A.

Because the crossover peaks have stronger signals, the setup is designed such that it will lock on the crossover peak $F' = 2, 3$, which is the strongest signal among the $F = 2 \to F'$ transitions, as opposed to a hyperfine line. An acousto-optical modulator (AOM) is used to create a frequency difference between the trapping beam and the spectroscopic beam (details of the AOM setup are given in a later part of this section). The schematic of the setup used is shown in Fig. 3.3. Another beam is injected into the cell at a different angle and its absorption profile is detected as a Doppler-broadened reference. The lock takes the saturated absorption signal and subtracts it from the Doppler broadened reference signal. The results of the subtractions are shown in Fig. 3.4. The circuit locks to a positive slope around the zero voltage (the offset level of the signal is adjustable) and gives a small correction signal to the laser's piezo element depending on how far and in which direction the signal deviates from zero. If the laser drifts towards blue-detuning and the signal becomes positive then the circuit will apply a voltage to

44

contract the piezoelectric element and shift the laser towards red-detuning, and vice versa. This design is a slight variation from the typical locking on the differential signal which allows locking directly on resonance, a commonly used technique described in Ref. [51].

Tapered Amplifier (TA)

A Tapered amplifier is a semiconductor diode in which a gain medium amplifies an external coherent field. Thus, the tapered amplifier requires similar temperature and current control system to the diode laser only with higher capacity (the TA diode current limit is 2 A, an order of magnitude or so higher than a normal laser diode). We free-space inject a 20 mW field from the trapping laser to create an output of field 600 mW. Due to its rectangular spatial mode, the beam is subjected to mode cleaning through a series of lenses and pinholes which results in a net output power of 380 mW. The schematic of the setup is labeled in Fig. 3.2.

Acousto-optic modulator (AOM)

An AOM is a device which shifts the laser frequency using acoustic waves in a crystal. The output pattern is that of a diffraction pattern, which allows the users to pick the order of frequency shift as needed. In our experiment, the AOM is set up to create approximately 130 MHz difference between the spectroscopic beam and the trap beams, allowing us to lock on the side of a crossover peak.

There are two ways of setting up the AOM to achieve this effect. The first configuration uses two 70-MHz AOMs working at the same frequency. One is placed in the beam path before the saturated absorption spectroscopy setup to create a red-shift. The other is placed after the TA mode-cleaning to a create blue-shift. This configuration reduces the optical loss by passing the trapping beam only once through the AOM, which results in a total trapping beam power of 150 mW. This level of optical power allows investigation into both the temperature limited and multiple scattering regimes. The disadvantages
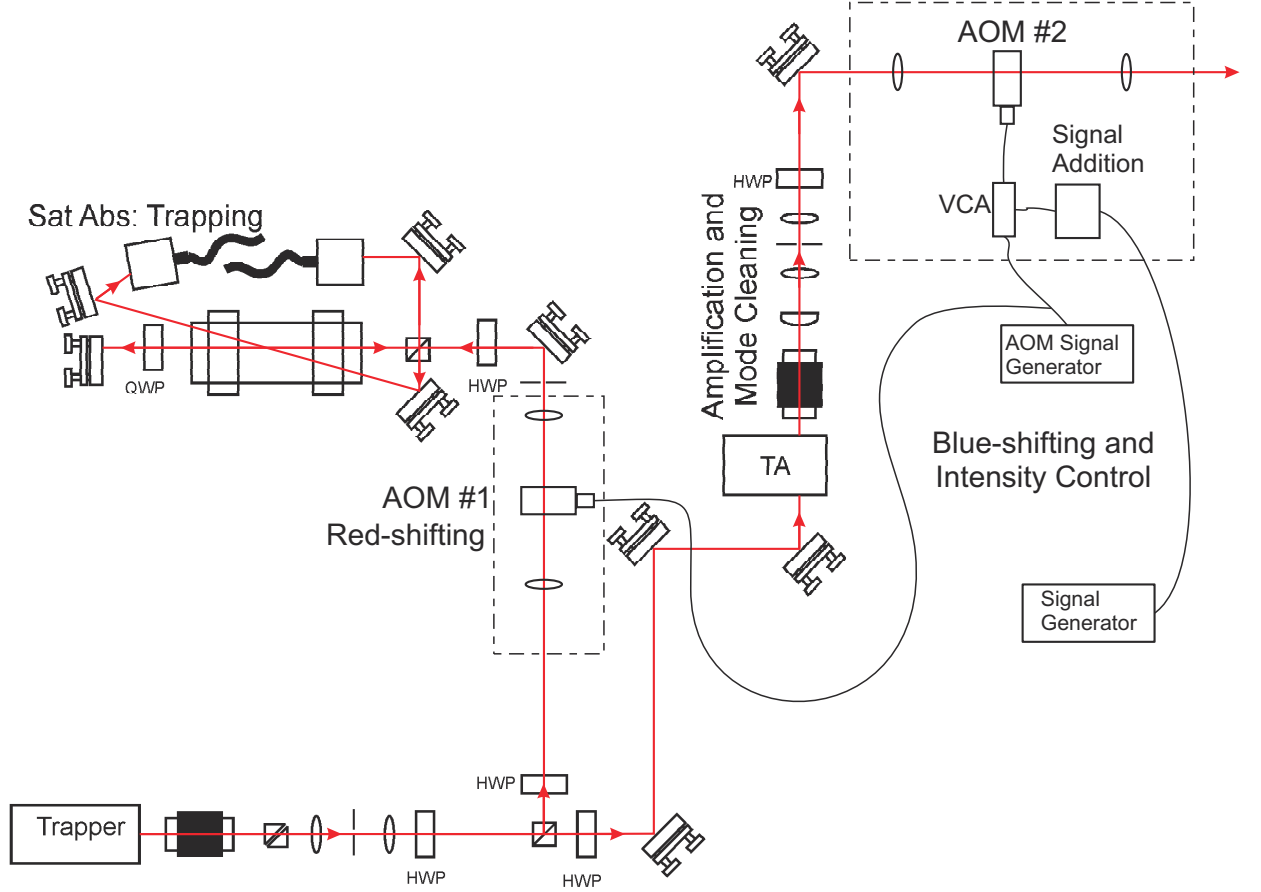
Figure 3.5: The positions and setups of the two AOMs used to create steady state MOT cloud.

of this configuration are the distortion in the trapping beam intensity profile and the angular shift in beam path dependent uopn the frequency of the AOM signal. In this configuration, the detuning of the trapping beam has to be fixed during the experiment because of the latter effect.

To allow instantaneous change in detuning needed for the investigation of atomic cloud compression, another configuration is used. Here, the selected mode from an AOM is reflected back into the AOM to form a double-pass configuration (shown in Fig. 3.2). The beam path of the output beam is insensitive to any frequency change in the AOM signal, allowing detuning of the trap beam up to -15 MHz without significant distortion of the spatial mode. Further detuning is limited mainly by the change in intensity profile as

the beam position deviates upon making the second pass through the AOM. The biggest disadvantage is the limited trapping beam power which goes up to 70 mW. However, due to a better intensity profile, the cloud in general is colder and less susceptible to beam alignment than the first configuration.

Since the cloud formation is less sensitive to the repumping laser, I do not use any AOMs in the beam path and lock the laser on the positive slope of one at the $F = 1 \rightarrow F'$ transitions generates the brightest cloud.

3.1.3 The Anti-Helmholtz Magnetic Coils

Our magnetic coils are made from shielded wire looped tightly to create a 4 cm radius ring with one hundred loops on each coil. The resistance is 0.03 Ω each. The coils are put inside a cylindrical brass casket for water-cooling. However, since our experiment does not require operation at high current for a long duration of time, the water-cooling system is not used. The two coils are then placed 12 cm apart in order to accommodate the vacuum chamber and connectors to the water-cooling system. The two coils are connected to a high-current source which can supply up to 100 A. With the coil-controlling circuits, only 35 A is presently achievable.

The exact form of the magnetic field from anti-Helmholtz coils (Fig. 3.6), can be found by integrating the vector potential $\mathbf{A}$ over each loop, then applying the curl to get the fields $\mathbf{B} = \nabla \times \mathbf{A}$. The details of the magnetic field calculation can be found in textbooks on electromagnetism such as Ref. [52]. In cylindrical coordinates, there is an azimuthal symmetry in the field and therefore only two components of the magnetic field need be considered: the on-axis field (B_z) and the radial field (B_ρ). The exact solutions for magnetic field components for when $I_1 = I_2$ are

$$B_z = \frac{\mu I}{2\pi} \frac{1}{[(R + \rho)^2 + (z - A)^2]^{(1/2)}} [K(k^2) + \frac{R^2 - \rho^2 - (z - A)^2}{(R - \rho)^2 + (z - A)^2} E(k^2)] \qquad (3.2)$$

47
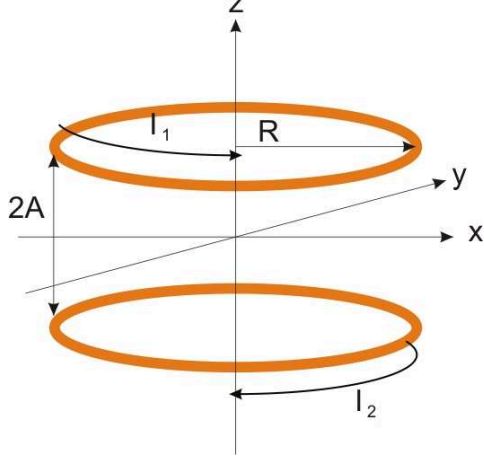
Figure 3.6: Schematic of an anti-Helmholtz coil pair with radius R and separation of $2A$. The current running through the coils are in opposite direction which creates opposing magnetic fields. Thus the configuration has a zero-point in between the coils. The exact position of the zero-field depends on the ratio between the current I_1 and I_2.

$$B_\rho = \frac{\mu I}{2\pi\rho} \frac{z - A}{[(R + \rho)^2 + (z - A)^2]^{(1/2)}} [-K(k^2) + \frac{R^2 + \rho^2 + (z - A)^2}{(R - \rho)^2 + (z - A)^2} E(k^2)] \qquad (3.3)$$

where $E(k^2)$ and $K(k^2)$ are elliptic integrals and $k^2 = \frac{4R\rho}{(R+\rho)^2+(z-A)^2}$, A is the distance of the coils from the center, R the radius of the coil. The solution is convenient when the z-component of the magnetic field at $\rho = 0$ is of interest. The magnetic field calculated for our experimental configuration is shown in Fig. 3.7(a) with the gradient change as a function of total coil current shown in Fig. 3.7(b).

Close to the center of the trap, the exact solution for B_ρ breaks down. The magnetic field close to this region can be calculated using the series approximation found in Ref. [53]. This method is used in the magnetic field numerical simulations. The result from the simulation is compared to the measured result from the coil setup (without the vacuum chamber) for validation since we cannot directly measure the magnetic field gradient once the vacuum chamber is in place. The simulation is also used to predict the change of the gradient around the zero-point with the current input.

The best separation between coils for steepest and most linear gradient is when $2A = R$. However, if our concern is with the linearity of the gradient at the center, the condition

48

is much more lenient since the atomic cloud is rarely larger than 1 or 2 mm and the gradient is approximately linear over a few centimeters. Therefore, a separation of 12 cm is suitable for the experiment.
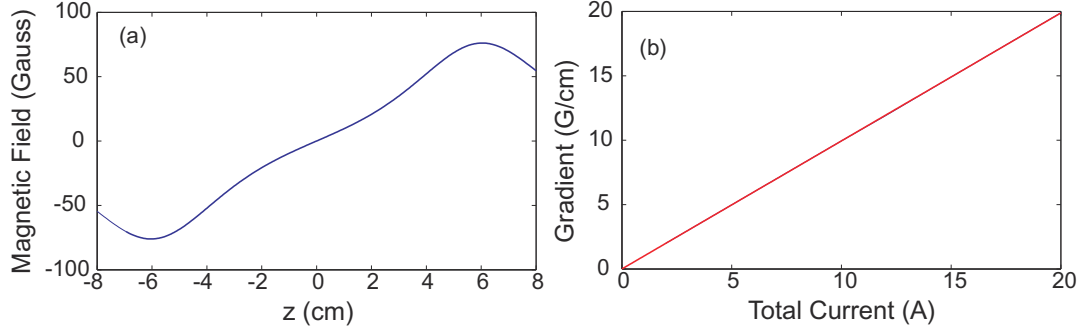
Figure 3.7: (a) The B_z field for a total current of 10 A and a separation of $2A = 12$ cm. (b) The change in B_z gradient around the center of the trap with the total current in the coils.

A shift in the zero-point of the magnetic field can be used to move the atomic cloud. We have evaluated two methods both with simulation and experiment. One is using an additional coil which is found to be ineffective due to distance between this extra coil and the center of the trap which is about 10-15 cm. The current is limited by the available current source and by heating of the coil, therefore limiting the magnetic field that can be generated. A shift of only a fraction of a millimeter is achievable with this method. The other method is to introduce a current imbalance into the anti-Helmholtz coils. The current imbalance is identified as a percentage of the current in one coil when the current in evenly distributed. The simulation shows that for a total current of 10 A, the cloud would move 6 mm for every 10% of current imbalance. We generally focus on moving just a few millimeters to ensure that the trapping condition does not change too drastically. The simulation also shows that the gradient deviates from the initial value by only 0.4% if the current imbalance is kept within 10% of the average value, giving us another operational limit.

3.1.4 The Vacuum Chamber
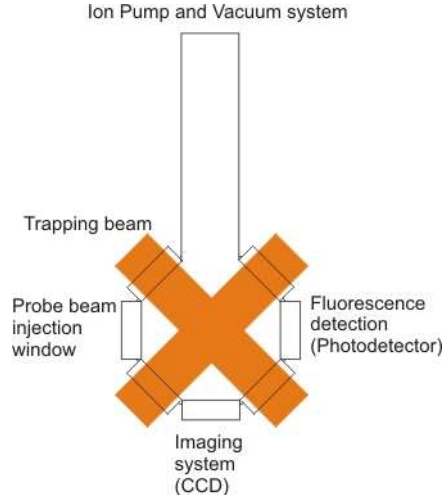
Figure 3.8: Schematic of the vacuum chamber and the function of each port.

The MOT chamber is made of glass and is 5.5 cm in height and 7 cm in diameter. Attached are nine windows, seven with a diameter of 2.5 cm and two with a diameter of 5.0 cm on the vertical ports. The function of each port is shown in Fig. 3.8. This chamber is attached to a four-way cross by a glass tube. One side of the cross leads to Rb/NF/3.4/12/FT10+10 Alkali Metal Dispenser (getters) from SAES. The getters are wired to a DC high current power supply which heats the rubidium salt coated on the getters and releases neutral ^{87}Rb gas. Another side of the cross leads to a three way cross in which the ion pump and a right-angle valve are attached. The pressure of the chamber is measured by the ion pump gauge which can show the pressure down to 10^{-8} Torr. The pressure is usually below this limit and therefore the exact number is unknown.

3.1.5 Electronics and Computer Control

In addition to laser locking, we need electronics to control the current in the magnetic coils and to adjust the power of the AOM signal to allow simultaneous changes on the trapping conditions.

50

Magnetic Coil On-Off Switch

This circuit was previously designed and built for simple on-off operation, allowing fast shutdown of the magnetic coil current in 200 μs. The circuit has two transistors to control an industrial grade insulated gate bipolar transistor (IGBT), which is the gate for the high current (Fig. 3.9). The magnetic coils are connected in parallel to the IGBT. This circuit is used in characterization of steady state atomic cloud.
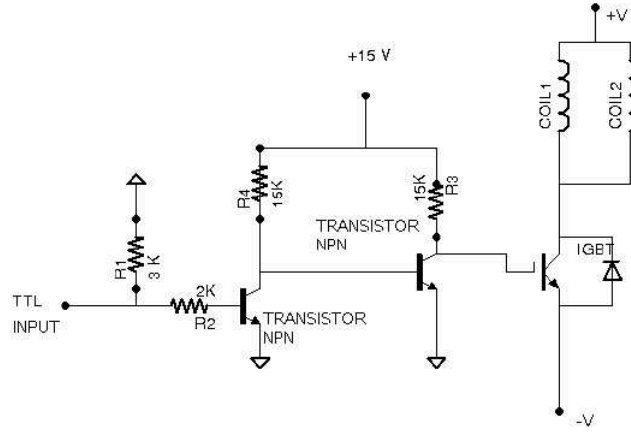
Figure 3.9: Schematic of magnetic coil on-off switch designed by Lucia Duca [54]. This circuit is used in characterization of steady state atomic cloud where only on-off operation is needed.

Magnetic Coil Current Control Circuit

In order to compress and translate the cloud, the current in each coil has to be controlled individually. The following circuit is used to provide continuous control over a single coil current using an electronic signal programmed by a computer. The transistors in the schematic (Fig. 3.10(a)) are a MOSFET and an industrial grade IGBT. The advantage of the IGBT is the high power tolerance that is not found in a typical MOSFET which allows it to operate at a current of tens of amperes for a long period of time without being destroyed. The increase in coil current is found to be linear with the controlling voltage, which is convenient to operate. It should be noted that the region of linear

response depends on the supply voltage and it should be checked prior to performing the experiment (Fig. 3.10(b)). This circuit replaces the on-off switch.
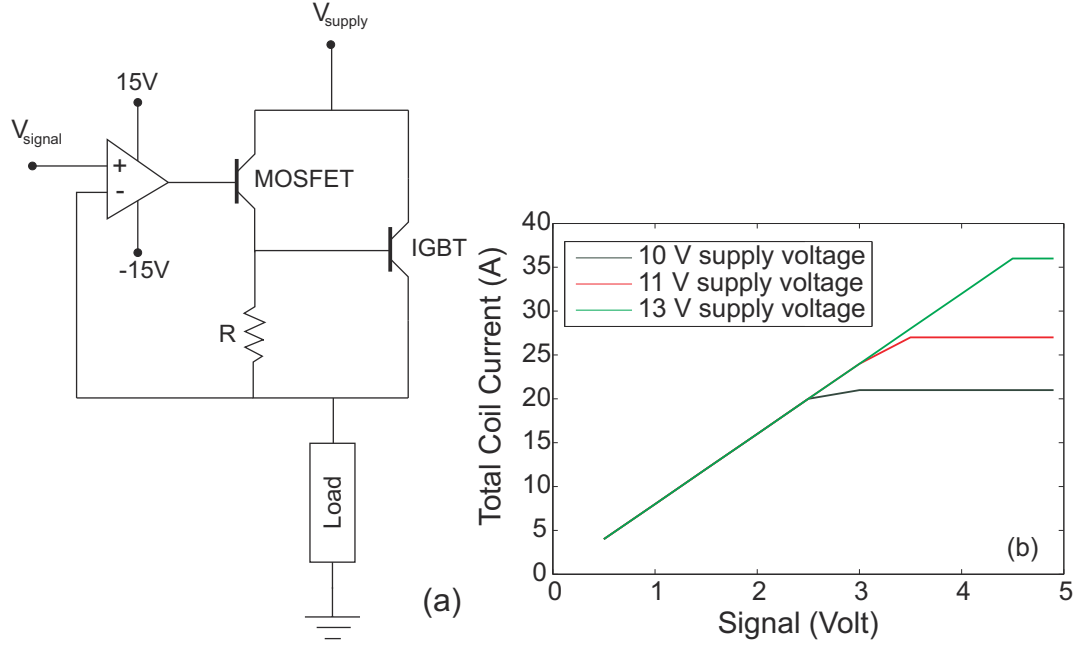
Figure 3.10: (a) Schematic of the continuous current controller. The load in this schematic is one of the coils. (b) The total coil current as a function of controlling voltage.

AOM Power Control

The intensity of trapping field is controlled by adjusting the power of the frequency signal going into the AOM. This can be done by varying the signal amplitude coming from the function generator. However, I found that the control is limited since the function generator is digital and therefore the attenuation needs to be preprogrammed. The minimum amplitude is also limited by the device, leading to no change in the trapping beam intensity over the allowed range. To gain better control, I use a voltage controlled attenuator (VCA) to vary the signal amplitude. The amount of attenuation changes in response to the voltage applied to the device. The attenuation can be varied over tens of dB, allowing a range of control on the trap intensity from complete shutdown of the trapping light to passing of about 50% of the input. For the study of the cloud

regime, the voltage controlling the VCA comes from another function generator. For cloud compression and translation, the signal comes from a digital-to-analog card (DAC) due to the more complex sequence required.

During temperature measurement, the time interval for shutting down the trapping beam needs to be accurate to a hundredth of millisecond in order to minimize the error in synchronization with the CCD camera. I use a function generator to provide the shutdown signal since its time resolution is much better than a DAC. This signal is added to the intensity control signal via a subtraction circuit (Fig. 3.11) with a potentiometer, allowing variation on the strength of the shutdown signal to make certain that the AOM is completely turned off.
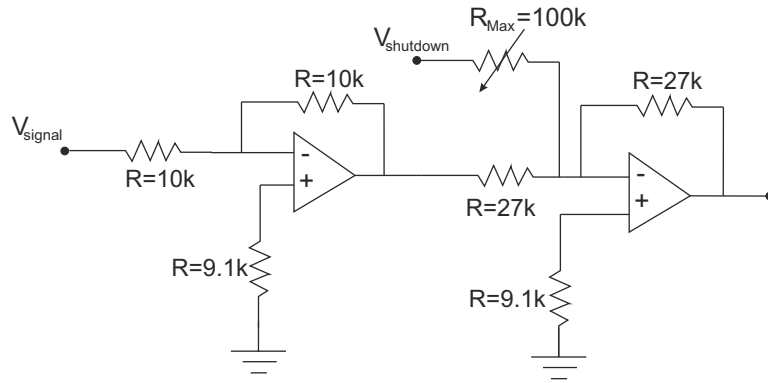
Figure 3.11: Schematic for VCA control circuit.

Digital-to-Analog Card (DAC) for Computer Control

While experimental parameters of the MOT can be controlled by combining signals from analog function generators, the compression and translation sequences require more complex waveforms and better synchronization than the signal generators can provide. DAC is used instead to provide the signals to different parts of the setup where accuracy of a millisecond is acceptable. It also allows both analog and digital control of the electronics.

The DAC used is an Acces I/O PCI-DA12-8 card with a PCI connection for fastest possible communication between the card itself and the computer. The card also has IRQ

functionality which allows the waveform to be saved and continuously repeated until the card receives an end signal. However, this function is not necessary at the moment as the required outputs are mostly square waves or a series of stepping functions.

The program for controlling the DAC is written using Microsoft Visual C++ Express (2008) with two parallel threads for running the GUI input form (Fig. 3.12) and the output signal simultaneously. The program is designed to operate in different modes corresponding to different operations on the cloud. The steady state (or DC) mode gives constant voltages in all required channels to create a steady state cloud. The compression mode creates a signal that will increase in equal steps until it reaches the programmed final value. The same signal is fed to the control circuits of the magnetic coils. The translation mode does the same operation as the compression mode but with one of the magnetic coil signal being reduced in equal steps as the other increases. An example of the signal is shown in Fig. 3.13. There are also two trigger channels from the card, signaling the beginning and the end of the compression period.

3.2 Alignment and Optimization

In the first alignment of the MOT, the position of the magnetic field zero-point must be determined. Without the vacuum chamber, the magnetic field is measured using a Gaussmeter. The point is marked by an LED which also serves as a mock cloud for aligning the imaging system. After the image is properly focused onto the CCD camera with some allowance for of what to re-focus if necessary, the trapping beams are aligned to cross at the LED.

The trapping laser – after being amplified, frequency shifted, and mode cleaned – is split into three beams. These beams are expanded to about an inch in diameter and sent through the three dimensions of the trap, each with a quarter wave plate to control the
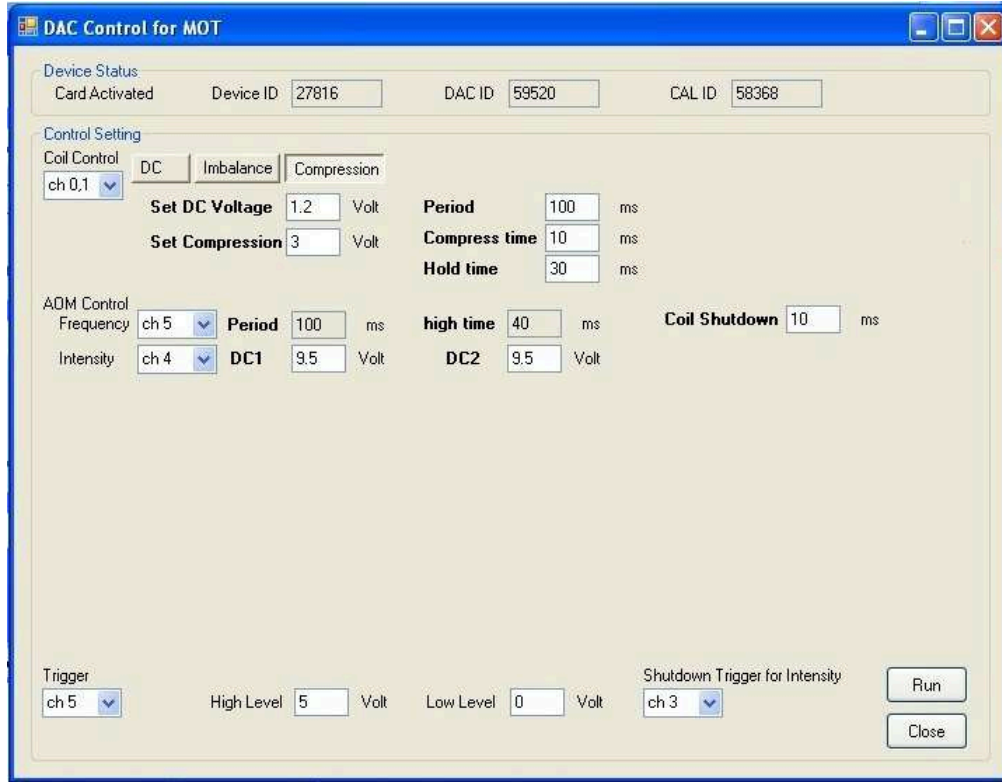
Figure 3.12: The GUI of the DAC control program.

polarization of the beam. After aligning the beams to cross at the magnetic field zero-point, the beams go through another set of quarter wave plates and are retroreflected back along the same path using metallic mirrors. As the beam are generally of the same size as the optics, the quarter wave plates and mirrors are used for marking the beam path for the retroreflected beams.

At this point, the LED is taken out of the system and the vacuum chamber is placed back between the coils. Care must be taken to ensure that the edge of the windows does not clip any part of the beams. The trap is turned on and, if everything is aligned correctly, a cloud should be clearly observable after some time. One mistake that can be made is when the trap is turned on for the first time during the day. The cloud will be rather faint, and the experimenter may be tempted to re-adjust the beams immediately. It might actually be that the gas inside the chamber is too hot to be captured right away.
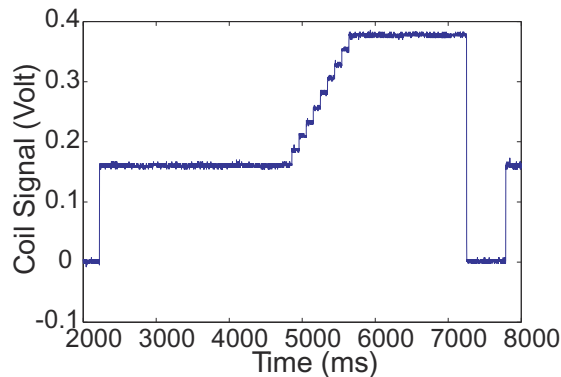
Figure 3.13: Example of a coil controlling signal for trap compression coming from the DAC.

The experimenter should allow some time for the atoms to accumulate inside the trap. This might take up to half an hour to reach steady state, but after ten minutes it should be possible to tell whether the trap is working properly and what kind of adjustment should be done.

The balance in trapping beam intensities on all dimensions should be checked before further optimization. Imbalance of the trapping beam intensities, aside from introducing anisotropic temperatures, is observed to limit the number of atoms in the trap. Once this is done, we can proceed to optimize the alignment. The beams might not be exactly counterpropagating or crossing each other at right angles on the first try. The latter can result in fringes in the atomic distribution as discussed at the end of Section 2.2.3. The fringes are actually a very useful guideline as the increase in the fringe width indicates that the alignment is moving closer to ideal. The experimenter needs to systematically adjust the alignment of each pair of beams until the fringes are no longer visible.

In the case where the intensity of the trapping beam is uniform throughout the transverse profile, the cloud profile should be Gaussian. In the experiment, the beams ideally have Gaussian profiles, and they are distorted by components such as the TA and AOM. This distortion of the beam profile results in a varying trap condition over space and gives a distorted cloud. This is more readily observed in traps with low trapping force

such as when the magnetic field gradient is low (5 G/cm instead of 10 G/cm or higher) or with low intensity (4 mW/cm^2 per beam instead of 6 mW/cm^2 or higher). With higher forces the cloud is often observed to have a nearly Gaussian profile with some distortion which can be corrected by small adjustments in the alignment. Once a Gaussian-shaped MOT cloud is formed, the measurements can begin.

3.3   Measurement Methods

The two properties of the MOT cloud that we are most interested in are the atomic density and the temperature and how they behave in different regimes. The temperature data can be used to ascertain the existence of polarization gradient cooling. The change in density with number of atoms can be used to distinguish between the temperature limited and the multiple scattering regime. To measure these properties, we need methods to measure the cloud size, the number of atoms, and the expansion of the cloud. Examples given in this section are for the purpose of illustrating the procedure. The experimental results will be given in Chapter 4.

3.3.1   Number of Atoms

The number of atoms inside the trap is measured by looking at the optical signal coming from either the fluorescence from the trapped atoms or the absorption of a probe beam. The fluorescence signal is due to the photons scattered from the trapping beams and therefore is directly proportional to the number of trapped atoms. This is the same signal used in imaging the cloud but is gathered from a separate port of the vacuum chamber onto a photodiode to allow analogue measurement of the optical power. The absorption method uses another weak laser beam as a probe and is aligned to pass through the cloud and is collected on a photodiode.

I usually choose one method for gathering data for an experiment depending on the

57

nature of the experiment. Fluorescence detection is used when the cloud has the potential to move such as when the magnetic field gradient is changed. This choice is due to the wide active area of the photodiode I use – approximately 3×3 mm^2. A millimeter displacement will not move the cloud outside of the detector's active area, but it can end up partially outside the probe beam resulting in an error on the measured number of atoms. This problem can be prevented by increasing the size of the probe. However, there is no way to observe how the probe and the cloud intersect, and the absorption signal will be reduced if most of the probe does not pass through the cloud. The absorption method is more favored when the cloud remains at a certain position and the fluorescence signal is compromised by background light.

Fluorescence Detection

A fluorescence image of the cloud is captured by a highly sensitive photodetector with an active area of 3×3 mm^2, large enough for a MOT cloud of 1 mm diameter. I use a lens of 50 mm focal length and 1.5″ diameter to gather fluorescence photons. The lens is placed approximately 10 cm away from the trap center. The number of photons gathered from the imaging system is determined by converting the response of the photodetector from voltage to power using the calibration graph of the particular detector in Fig. 3.14.

To find the total power emitted by the cloud, we must first find the ratio between the solid angle of our detection system, or more precisely the solid angle of the lens, and the solid angle of a sphere. The solid angle of a cone is $\Omega(\theta) = 2\pi(1 - \cos\theta)$ where θ is half the apex of the cone. Using this formula, we find the total solid angle of a sphere to be $\Omega(\theta = \pi) = 4\pi$ which gives us the ratio

$$\frac{\Omega(\theta)}{\Omega(\theta = \pi)} = \frac{1 - \cos\theta}{2}. \tag{3.4}$$

Each photon has an energy of $E = \hbar\omega = hc/\lambda$. The number of photons scattered from
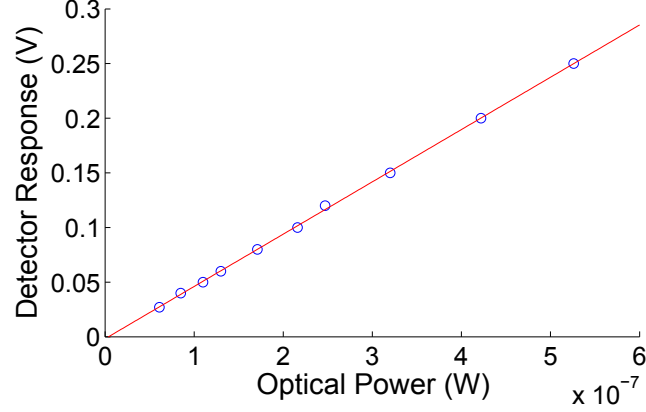
Figure 3.14: The detector's response to optical power with a linear regression. The best fit line is $y = 4.96 \times 10^5 (V/W)x + 0.0018(W)$.

each atom per unit time is the scattering rate

$$\mathcal{R}_{\text{scat}} = \frac{\Gamma}{2} \left(\frac{I_{\text{t}}/I_{\text{tsat}}}{1 + 4(\frac{\Delta}{\Gamma})^2 + I_{\text{t}}/I_{\text{tsat}}} \right) \tag{A.23}$$

where I_t is the total trapping intensity (6 beams combined) and I_{tsat} is the saturation intensity of the trapping beam. The number of atoms calculated from the data is

$$N_{\text{atom}} = \frac{P}{hc/\lambda} \frac{2}{(1 - \cos\theta)} \frac{1}{\mathcal{R}_{\text{scat}}}. \tag{3.5}$$

where P is the optical power of the fluorescence signal.

Absorption Detection

The other way of determining the number of atoms in the trap is by measuring the absorption of a probe injected into the cloud. Since the ensemble is one of cold atoms, the linewidth of the absorption is relatively narrow; i.e., ≈ 6 MHz. This creates a challenge in locking the laser to the right frequency. One way to get around this difficulty is to use a scanning laser instead. By scanning over the absorption line, we can determine the absorption at resonance and calculate the number of participating atoms. The size of the probe beam is set to a diameter of 2 mm to cover the entire cloud in order to give accurate readings.

59

The probe power is very weak so to not disturb the trap mechanism. However, we must take into account that the probe will be competing with the trapping beam. The atoms absorbing the probe is the portion that is not participating in the cooling process. Since the trapping intensity is much higher than the probe intensity (around 36 mW/cm^2 in total compared to 0.4 mW/cm^2), I assume that the cooling process is not disturbed by the presence of the probe. The absorption signal then comes from the probe's interaction with the ground state population $\rho_{gg} = 1 - \rho_{ee}$.
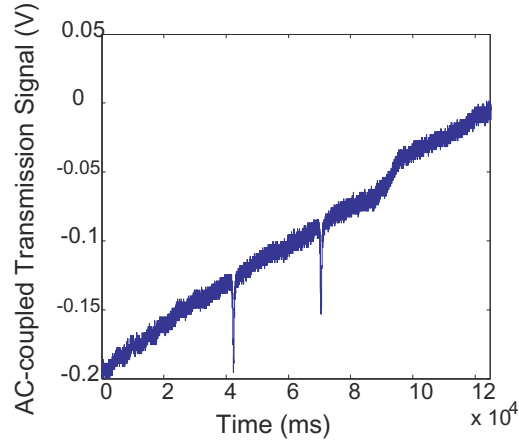
Figure 3.15: An example of absorption profile of an ^{87}Rb MOT cloud taken using an AC-coupled oscilloscope. The slope seen here is the change in input intensity with the scanning of the laser. This is only detectable because we are detecting at the μW optical power level. The two absorption lines correspond to two different hyperfine levels in the excited state.

The transmission of a medium follows the Beer-Lambert law which states that the transmitted signal follows the relation

$$T = \frac{I}{I_{\text{in}}} = \exp\{-\sigma ln\} = \exp\{-\frac{\sigma}{A}N\} \tag{3.6}$$

where I is the transmitted intensity, I_{in} is the input intensity, σ is the scattering cross section of one atom given by Eq. (A.24), l is the length of the medium which the light passes through, and n is the mean atomic density over the laser beam area A. For an accurate measurement, the entire cloud has to reside inside the probe beam. For N being

60

the number of atoms participating in the absorption and N_0 the number of trapped atoms, $N = N_0 \rho_{gg} = N_0(1 - \rho_{ee})$ where ρ_{ii} is the probability or population of the atoms in a state. The calculation for the expression is derived in Appendix A. We can replace the density with $n = \frac{N}{Al}$.

The signal recorded from the experiment is in fact the power of the transmitted beam. With the beam collimated along the length of the cloud, the transmission can be written as ratio of output to input power. The absorption shows up as a dip in the signal as the laser scans across the resonant frequencies. The size of this dip is easier to measure than the total signal, as I can use the AC-coupling mode of the oscilloscope to zoom into the signal. The reference level is measured separately using the DC-coupling. The transmission signal is shown in Fig. 3.15. The transmitted optical power can be written as $P = P_{in} - P_{dip}$ and the number of atoms participating in the absorption is

$$N = -\frac{A}{\sigma} \ln\left(1 - \frac{P_{dip}}{P_{in}}\right). \tag{3.7}$$

where $\sigma = \frac{\hbar\omega\Gamma}{2(I_p + I_{psat})}$ for resonant light is used. N is assumed to be the number of atoms in the ensemble in the ground state during the cooling process. The total number of atoms is related to N by

$$N_0 = \frac{N}{\rho_{gg}} \tag{3.8}$$

$$= -\frac{A}{\sigma} \ln\left(1 - \frac{P_{dip}}{P_{in}}\right) \frac{2(1 + 4(\Delta/\Gamma)^2 + 2I_t/I_{tsat})}{2(1 + 4(\Delta/\Gamma)^2) + I_t/I_{tsat}} \tag{3.9}$$

Compared with the fluorescence method, there can be a discrepancy in number of atoms of about 25%. For instance, the number of atoms indicated by fluorescence detection is 1.5×10^6 while the number from absorption detection is $\approx 1.9 \times 10^6$. The cloud size for this case is less than 0.5 mm and typically gives a cloud with density of in the order of $10^9 - 10^{10} cm^{-3}$. This discrepancy in number of atoms and therefore density may become troublesome if the data is to be compared between methods. Since the primary

interest at the moment is the trend and not the absolute numbers, these discrepancies are overlooked. For a particular characterization – the atomic density with the change of number of atoms under different field gradients, for instance – only one method is used and never to be directly compared with the result of another.

3.3.2 Trap Lifetime from Loading Profile

Assuming there are no collisions between trapped atoms, the change in number of atoms with time is $N(t) = N_0(1 - \exp\{-t/\tau\})$ (Eq. (2.44)) where τ is the trap lifetime, and N_0 is the steady state number of atoms. The lifetime of the trap is found by collecting the fluorescence signal during the loading. An example of this signal is shown in Fig. 3.16. The lifetime is extracted by fitting the data to $\ln(N_0 - N(t)) = \ln(N_0) - t/\tau$ (Fig. 3.17). The lifetime is simply the inverse of the slope of this linear fit.
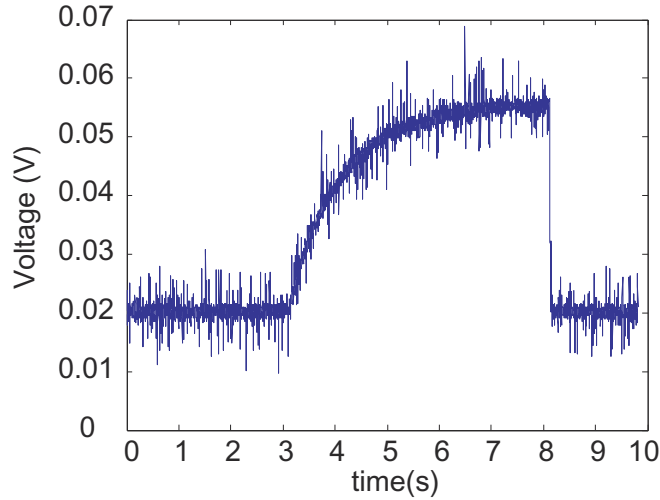
Figure 3.16: An example of fluorescence signal during trap loading.

3.3.3 Cloud Radius

The fluorescence image of the cloud is taken using a grayscale CCD camera. The value in each pixel is averaged over many images to reduce noise due to the fluctuation in number of atoms. The data collection is controlled by a program written in LabVIEW which also
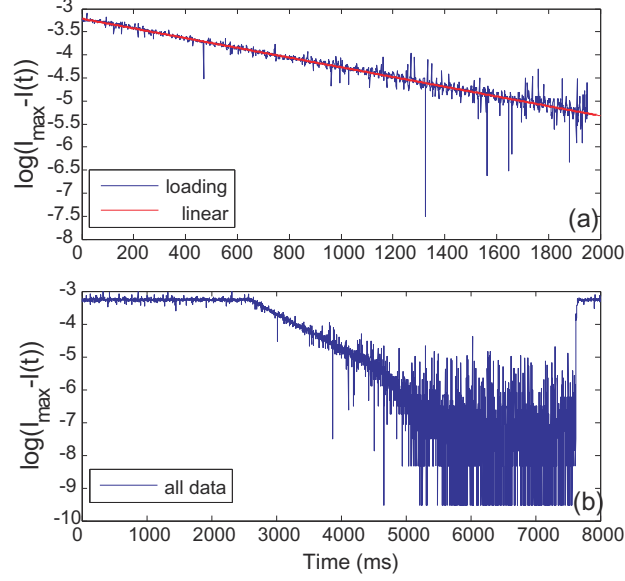
Figure 3.17: An example of linear fitting of trap loading data. (a) The fitting procedure is done only on the loading part. (b) The log of the signal from the entire period.

controls the camera operation mode and exposure. The CCD camera is triggered by a signal from a function generator which also synchronizes the trapping beam shutdown. This method is used to capture the image of both the steady state cloud and the expanded cloud in temperature measurement (Section 3.3.4).

The profile of a well-optimized cloud is typically Gaussian with minor distortion that are often visible only during analysis of the cloud profile. For a cloud that is not yet fully optimized, such as those in Fig. 3.18, the profile can have fringes as shown in Fig. 3.18(a) which are results of spatially dependent polarization gradient cooling discussed in Section 2.2.3. The Sisyphus cooling depends on the splitting between ground state sublevels which can have a beat pattern if the three pairs of trapping beams are not crossing at the right angles. The varying cooling force is the reason that causes the interference fringes. A perfect alignment of the cooling beams should give a fringe-free cloud as shown in Fig. 3.18(b) which can still have distortion due to the non-uniformity of the trapping beam profile which distorted the trap from the ideal harmonic shape.

Because of the possibility of having distorted cloud profiles, I developed two methods
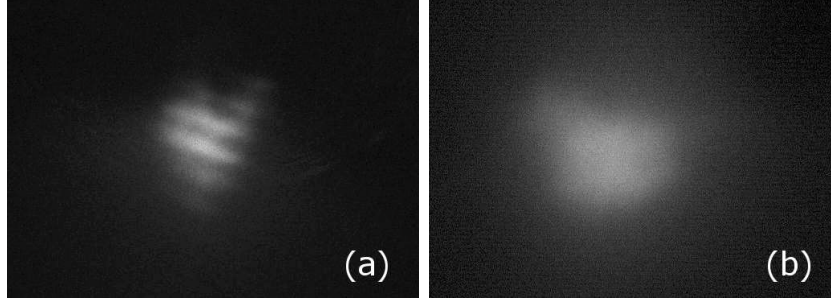
Figure 3.18: An example of a cloud under the influence of interference as discussed in Section 2.2.3 (a) and one that is not (b). The cloud in (b) is distorted by non-uniformity in the trapping beam profile.

of determining the cloud size from an image: the Gaussian fit method and the area fit method. Both analyses are done in MATLAB.

Gaussian Fit

This is the primary method that is used as the clouds generally have Gaussian profiles. Care should be taken with the image of the xy-direction since the camera is in fact pointing at a 45° angle with respect to the horizontal trapping beams. Therefore, the cloud profile in the xy-dimension is half a projection of x-dimension and half of y-dimension which can result in an asymmetric Gaussian profile. If the trap is optimized with equal trapping beam intensity on both x and y dimensions, no difference in the profile of the two dimensions should be observed in both the steady state profile and during the expansion. In this case, the Gaussian fit method will give an accurate representation of the cloud size. The azimuthal symmetry will also allow us to disregard the fact that the image is a projection onto the 45° plane.

The profile of the cloud is assumed to follow the Gaussian distribution

$$y = A \exp\{-\frac{(x - x_0)^2}{2\sigma^2}\} \tag{3.10}$$

where y is the CCD signal representing the intensity of the cloud image at a particular position in one dimension. The size of the Gaussian is defined to be the position from

64

the maximum of the profile to where the signal is $1/e$ of the maximum value. In this case, the size of the cloud will be $\sqrt{2}\sigma$ according to the notation used.

Since Matlab has an algorithm for polynomial fitting, the equation is modified to have polynomial form:

$$\ln y = -\frac{x^2}{2\sigma^2} + \frac{x_0 x}{\sigma^2} + \left(\ln A - \frac{x_0^2}{2\sigma^2}\right). \tag{3.11}$$

The value of $\sqrt{2}\sigma$ can be extracted from the coefficient of x^2. The goodness of fit is determined using the R-squared from the least squared method. This method is use for linear regression, but it can also be modified to use with nonlinear fit as well [55].

The fitting procedure is as follows. The images of the cloud are taken and averaged as previously described. For images with background patterns (speckle patterns, for instance), the image of the background is taken separately and subtracted from the cloud image before analysis. The center of the cloud is determined by summing up each column (for finding the center in the horizontal or xy-dimension) or row (for vertical or z-dimension). The position of the maximum is determined by a Gaussian fit to average out the fluctuations. The second step is summing 10 rows (or columns) around the center and fitting the profile to a Gaussian function (Fig. 3.19). This is done for the two dimensions separately. The width of the Gaussian function in pixels is then converted into millimeters by taking into account the magnification of the imaging system ($\times 1$ in this case) and the physical size of a CCD pixel ($3.75 \times 3.75 \ \mu m^2$).

Area Fit

This method is strictly used for estimating the atomic density, as it does not provide separate information for xy and z dimensions. It is used mostly when the cloud takes a shape that cannot be accurately captured using the Gaussian fit method. Generally, proper optimization uses the steps mentioned in Section 3.2 will avoid having such a skewed cloud. In experiments such as trap compression and cloud translation it is possible
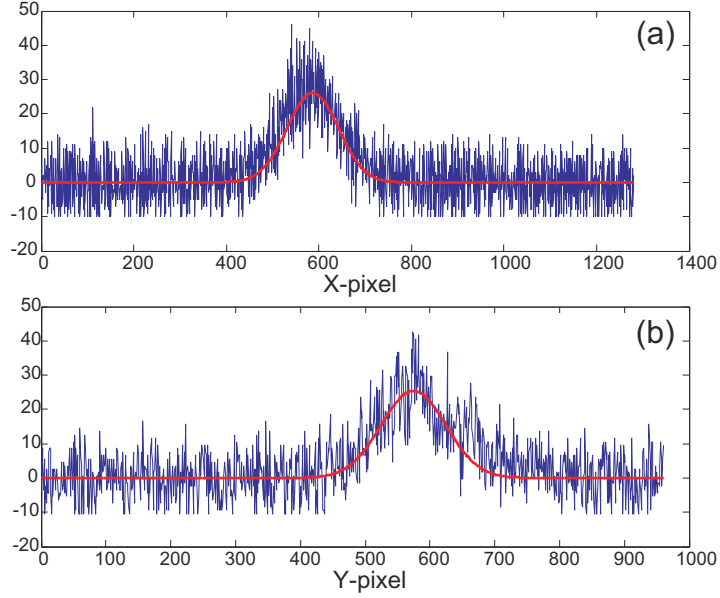
Figure 3.19: An example of the cloud profiles from one image (without averaging) along the horizontal (a) and vertical (b) dimension and its Gaussian fit. The noise observed here can be greatly reduced by averaging over several images.

to observe a cloud of various distorted shapes as a result of changes in the trap condition that cannot be accounted for in the optimization process.

The area fit method measures the area of the cloud in the image by counting pixels with values higher than a cutoff. Using the model of a Gaussian cloud, the cutoff is set to $1/e$ of the highest value. First, the image of the cloud is averaged to remove large fluctuations. The program then searches for the highest value in the picture to calculate the cutoff. The program counts the number of pixels with values above this cutoff and converts it into an area. The volume is extrapolated by assuming that there is a spherical cloud with the same cross section that gives approximately the same volume. This method has been tested with Gaussian cloud and compared to the Gaussian fit method. The radii and volume are found to be the same. Due to the comparable results, I am quite confident in using this method with the clouds that are not Gaussian. It should be kept in mind that for the clouds that have very distinctly non-Gaussian profiles, a more elaborate model for extrapolating the volumes will be needed.

3.3.4 Temperature Measurement

As mentioned in Section 2.2, the ensemble of trapped atoms can have average velocity components that differ from dimension to dimension due to each dimension of the trap having different cooling and trapping forces. To account for the anisotropy during characterization, the temperature of each dimension has to be measured separately. This definition of temperature is not the same as the definition given by thermodynamics. However, this is a common jargon used with the MOT, because it is more convenient to keep track of changes during characterization using this definition. Since the transverse magnetic field is azimuthally symmetric, the force on the x and y dimensions should be equal for an optimized trap and therefore the transverse velocity components should also be azimuthally symmetric. Therefore, the temperature of the transverse dimension of the cloud can be measured directly from the image although the camera is placed at $45°$ without the need to account for this tilting.

The temperature of a particular dimension can be measured by the rate of cloud expansion along the dimension without the influence of the trapping forces. To see how this works, we first assume the atoms to have a Maxwell-Boltzmann velocity distribution in one dimension of

$$f(v_\mathrm{i}) = \sqrt{\frac{m}{2\pi k_\mathrm{B}T_\mathrm{i}}} \exp\left(-\frac{m}{2k_\mathrm{B}T_\mathrm{i}}v_\mathrm{i}^2\right). \tag{3.12}$$

The initial atomic distribution is taken to be a Gaussian function $n(r_0) = n_0\exp\{-r_0^2/R_0^2\}$ where R_0 is the initial cloud radius and r_0 is the position variable at time $t = 0$. Without the influence of the trap, the atoms move to different positions according to the velocities they initially have. If we are observing at a position r from the cloud center, once a time t has passed the atoms which are at r will be the ones that have the velocity and initial position such that $r = vt + r_0$. To find how many will reside at r, we have to integrate over all the initial positions of the atoms, r_0. The velocity distribution is assumed to be

independent of the position. Therefore, the atomic distribution at time t and position r is the integration over the distribution of the initial atomic positions multiplied by the probability of an atom in position r_0 having the velocity $v = (r - r_0)/t$:

$$n(r,t) = \int_{-\infty}^{\infty} \sqrt{\frac{m}{2\pi k_B T}} \exp\{-\frac{m}{2k_B T} \frac{(r - r_0)^2}{t^2}\} n_0 \exp\{-r_0^2/R_0^2\} dr_0. \tag{3.13}$$

Equation 3.13 is a convolution of two functions. Therefore, we can compute this using the Fourier transform property of the convolution which states that [56]

$$\mathscr{F} \left[\int_{-\infty}^{\infty} G(x_0) H(x - x_0) dx_0 \right] = \mathscr{F} [G(x)] \mathscr{F} [H(x)]. \tag{3.14}$$

The Fourier transformation is defined by

$$\mathscr{F} [G(x_0)] = \int_{-\infty}^{\infty} G(x_0) \exp\{-\imath 2\pi k x\} dx. \tag{3.15}$$

From this theorem, Eq. (3.13) can be computed much more easily by first performing the Fourier transformation on each distribution separately, joining the function in the momentum space, and performing an inverse Fourier transformation. Since the function for both atomic distribution and velocity distribution are Gaussian, the result of the calculation is also a Gaussian function. The width of the resulting Gaussian distribution is

$$R^2(t) = R_0^2 + \frac{2k_B T}{m} t^2. \tag{3.16}$$

Expression 3.16 is the expansion of the cloud width under the assumption that the velocity distribution is not disturbed during the expansion. Hence, the trap, meaning both the magnetic field and the trapping light, has to be shut down during the expansion. This condition also prevents us from monitoring the expansion continuously since there cannot be any interaction with light and therefore no fluorescence photons. The expansion is recorded by taking still pictures of the cloud after it is allowed to expand for a set period

of time. Typically, an image of the cloud is taken every 1 ms from an expansion time of 1 ms to 10 ms. The pictures for each shutdown interval are averaged over 5 to 15 images, and the cloud radius is measured using the Gaussian fit method described in Section 3.3.3. The expansion rate is estimated by performing linear regression on the plot of t^2 and R^2 as shown in Fig. 3.20, and the temperature of the particular dimension can be extracted from the slope. During this process, the repumping beam need not be
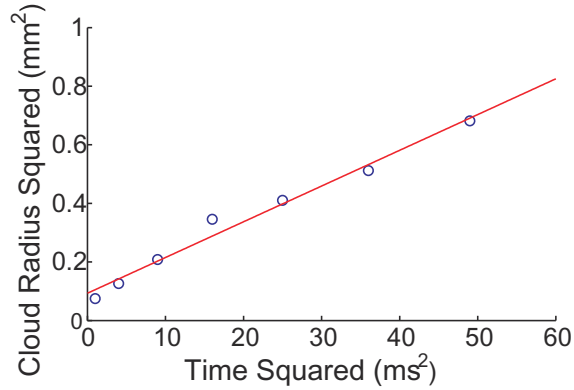
Figure 3.20: An example of data fitting for temperature measurement.The temperature in this example is $\sim 120\mu K$.

shut down since the majority of the atoms are in the $F = 2$ states due to the cyclic trapping transition. If some of them are not, they will interact with the repumping laser only once and gain a recoil energy which is negligible compared to the initial kinetic energy of the ensemble.

This ballistic expansion can be interrupted by other factors aside from the trap forces. One is the collisions with hot atoms which makes the cold atoms move randomly rather than in straight line as previously assumed. This limits the time where Eq. (3.16) is valid during the expansion. The data gathered from the setup so far is usable to approximately 10 ms after the trap shutdown. It has been demonstrated that it is possible to observe the expansion up to 30 ms under appropriate conditions [43].

Chapter 4

Results of MOT Characterization

After trap optimization, changes in cloud properties can be measured by varying trap parameters. The main parameters of interest are trapping beam intensity and magnetic field gradient. However, alignment and intensity profile can also affect cloud properties. To reduce variability during characterization, some parameters need to be kept constant. In our system, the coherence time of a quantum information process is dependent on the loss rate of atoms from the cloud. One parameter that affects this coherence time is the trap lifetime. In this chapter, the first focus will be on the effect of background pressure on the trap lifetime. A getter current setting can then be extracted so the remainder of the characterization can begin. Characterization will first be performed in steady state MOT where change in cloud regime will be demonstrated. Afterward, the effect of the field gradient on the steady state MOT will be studied as a baseline for a trap compression experiment. The transient compression of atomic density will be investigated and discussed in the section that follows. Lastly, I will examine the effects of cloud translation by shifting the magnetic field's zero-point.

4.1 The Effect of Background Pressure

The background pressure affects the loss rate of a MOT as discussed in Section 2.3.3. The loss of atoms will in turn affect the coherence time of a quantum information process performed by the ensemble. There are, of course, other factors that can affect the coherence time. However, in order to rule out the effect of hot collisions, a suitable value for the background pressure must be set.

The pressure gauge used for the vacuum chamber is the one attached to the ion pump which has a minimum resolution of 10^{-8} Torr. The pressure in the system is below 10^{-8} Torr and does not rise significantly enough to be detected once the chamber is filled with rubidium vapor. Therefore, no quantitative measurement can be made on the actual background pressure in the current setup.However, rubidium vapor is produced by heating rubidium salt coated on electric wires, called getters, with electrical current. Hence, the background pressure will increase proportionally with the amount of current running through the getters. The power in these wires can be directly controlled from the getter's power source albeit at a resolution of half an ampere which is quite crude.
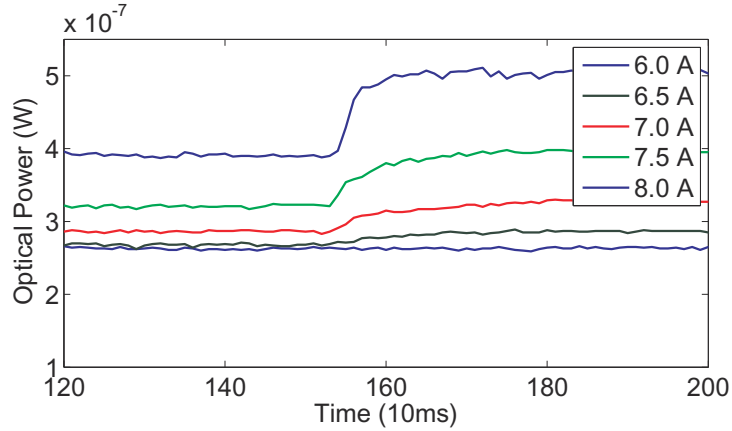
Figure 4.1: Fluorescence signal at the MOT loading for different getter currents. The first part of the signal comes from background atoms which increases as the background pressure increases. The cloud signal is superimposed on this background.

From this experiment, an optimal current can be determined to give the longest possible lifetime without significantly compromising the number of atoms collected in the trap. As shown in Fig. 4.1, the number of atoms in the steady state trap increases as the getter current increases. Using the method described in Section 3.3.2, the trap lifetime can be extracted from the loading curve and is shown in Fig. 4.2 as a function of the getter current. According to this data, the best compromise is to operate the setup at a getter current of 7 A which has a lifetime of 0.97 s. This value comes right before the

background pressure significantly reduces the lifetime. The lifetime is longer with lower getter current but with a reduction in the number of trapped atoms. At a current below 6 A, the fluorescence signal is too small to identify the loading curve and perform the fitting due to the low number of atoms. This makes a getter current of 6 A the lowest operational limit we have for our setup.
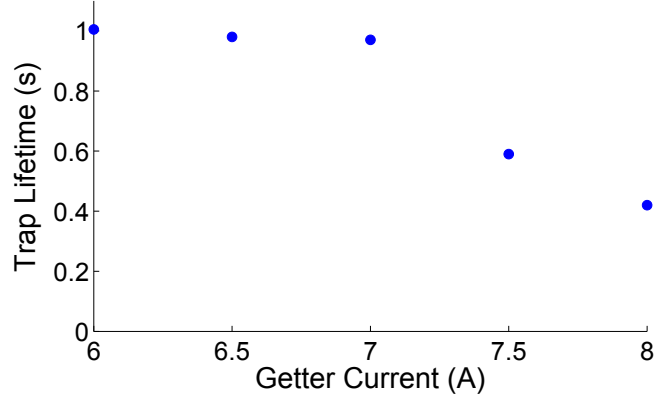
Figure 4.2: Measured trap lifetime as a function of getter current.

If the lifetime can be compromised, the getter current can be used to control the number of atoms as seen in Fig. 4.1. However, the extent of control using this method still needs to be determined. It would be a great advantage if a simple relation between the getter current and the steady state number of atoms can be found. In the simplest case, the change in the number of atoms is directly proportional to the resistive heating which depends on the square of getter current. By taking a closer look at a plot on log-log scale, this relation turns out to be nonlinear therefore suggesting a more complicated correlation. With this relation undetermined and poor resolution on the getter current, loading atoms by changing getter current is not used in any experiment. Figure 4.3 shows the change in fluorescence signal at steady state, which is directly proportional to the number of atoms, with getter current. The cubic fit is to give a suggested trend but is not meant to be used for prediction as the resolution for the getter current is already 0.5

A.
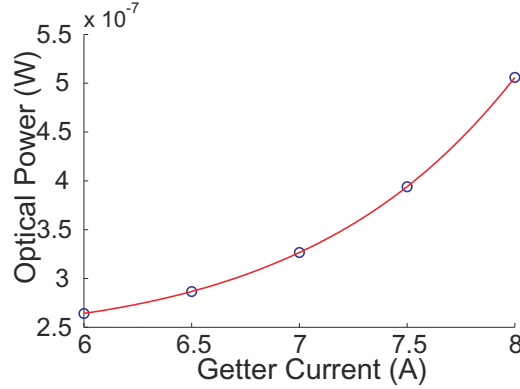
Figure 4.3: The fluorescence power after the cloud reaches steady state at different getter currents. The line is a cubic fit to give a suggested trend.

4.2 Regime Transition with Trap Intensity

Once a suitable getter current is determined, the investigation into the regimes of the steady state cloud can begin. The most obvious difference between the temperature limited and the multiple scattering regimes lies in the change of atomic density with respect to the number of atoms. The density increases with the number of atoms in the temperature limited regime, whereas the density is independent of the number of atoms in the multiple scattering regime (as discussed in Section 2.3.4). Ideally, the number of atoms should be changed while trap conditions should remain stable in order to demonstrate the transition between both regimes. With the limitations from Section 4.1 in mind, another option arises from a method used in Ref. [43]. The trapping beam intensity can be varied to control the number of atoms in the trap. The detuning is set to ?20 MHz throughout this experiment.

The temperatures of the xy and z dimensions are measured to evaluate whether the cloud is at sub-Doppler temperature which is below 146 μK for Rubidium 87 as stated in Table 3.1. The sub-Doppler temperature is also a positive indication of the trap

being in the temperature limited regime, although the temperatures in and of themselves cannot be used to classify the regime. Figure 4.4 shows the temperatures for the vertical dimension (the coil axis) and the horizontal dimension (the transverse plane) for three different trap intensities. The lines in the figure are used to guide the eyes only and are not linear fit lines. For an intensity of 30 mW/cm^2, temperatures below the Doppler limit are observed.
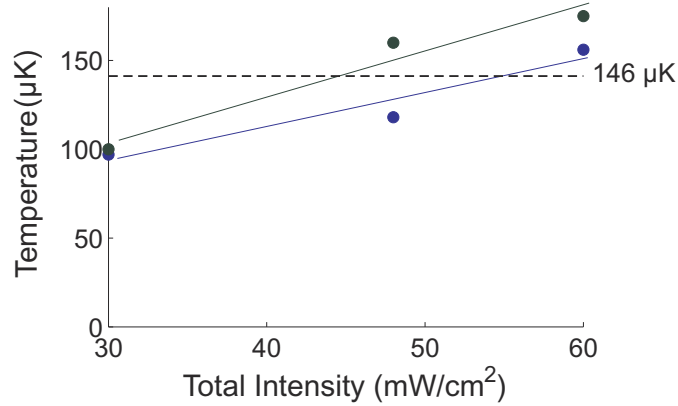
Figure 4.4: Cloud temperatures at $\Delta = -20$ MHz with varying total trapping intensity. The blue dots are the temperatures in the xy-dimension and the green dots are temperatures in the z-dimension. The data at 30 mW/cm^2 show the temperatures below the Doppler limit of 146 μK for both dimensions of the cloud. The lines drawn are to guide the eyes only and are not for fitting the data to any trend.

Theoretically, the temperature changes linearly with the trapping beam intensity according to Eq. (2.50). This is confirmed experimentally in Refs. [42, 43]. Our data follows this trend; however, since there are only three data points, it is not possible to conclude that the trend is linear.

For each trapping beam intensity, the number of atoms and the cloud radius is measured. From this measurement a density is calculated. Figure 4.5(b) shows an increase of the density up to a peak before dropping down as trap intensity increases. This can be explained if the cloud is in the multiple scattering regime. A more intense trapping beam results in a higher scattering rate which in turn increases the probability of re-scattering
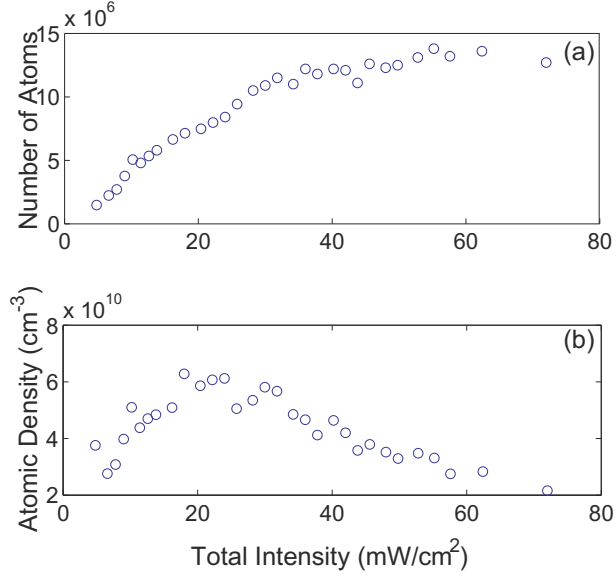
Figure 4.5: (a) Atomic density and (b) number of atoms with the change in trapping field intensity at a magnetic field gradient of 14.5 G/cm.

resulting in an increase of repulsive photon pressure. This peak appears when the ensemble transitions from the temperature limited regime to the multiple scattering regime. The regimes can be readily visualized by looking at Fig. 4.6 which is a plot of atomic density against the number of atoms. The plot exhibits the same trend as observed in Refs. [23, 43] with the first part of the trend showing an increase in atomic density with number of atoms before reaching a plateau. These are the trends predicted by the theory of the temperature limited and the multiple scattering regime respectively. The third part, which is a decrease of atomic density with number of atoms, corresponds to the decrease in density in Fig. 4.5(b) where the number of atoms barely changes (Fig. 4.5(a)). This, as mentioned earlier, can be easily explained for a cloud in multiple scattering regime. These data confirm that the cloud in our MOT is indeed in either of these two regimes and therefore the atomic density in our setup is limited by the atomic density of the multiple scattering regime.
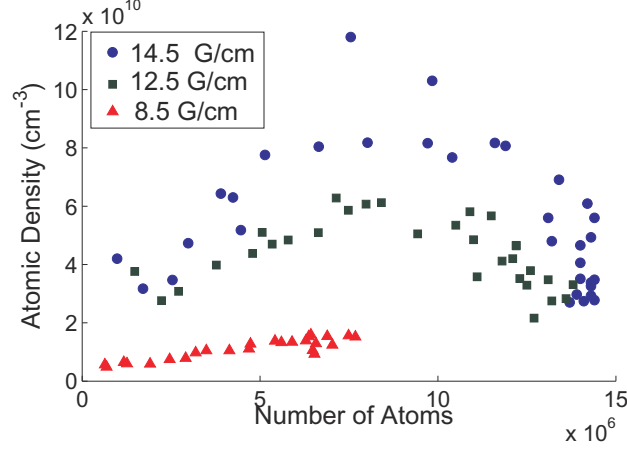
Figure 4.6: Atomic density changes with number of atom at three different field gradients.

4.3 The Effect of Field Gradient on the Steady State Cloud

Before proceeding to cloud compression, the effect of field gradient on the steady state atomic cloud was investigated in order to provide some baseline on the cloud behavior for the compression experiment. In this part of the experiment, the intensity of the trapping beam is 6 mW/cm^2 per beam and the detuning is kept at -8.3 MHz.

Theoretically, the radius of a cloud in the temperature limited regime should scale as $\left(\frac{dB}{dz}\right)^{-1/2}$. This is derived from the simple relation between the cloud radius and the temperature:

$$
\begin{aligned}
\frac{1}{2}\kappa r^2 &= \frac{1}{2}k_B T \\
r &= \sqrt{\frac{k_B T}{\kappa}} \\
r &= \sqrt{\frac{\hbar k k_B T}{\alpha \mu_B}} \left(\frac{\partial B}{\partial z}\right)^{-1/2} .
\end{aligned}
\tag{4.1}
$$

In the multiple scattering regime, the cloud radius depends on the number of atoms which makes the relation between the field gradient and the cloud radius much more complicated.

The change in cloud radius with gradient is plotted using log values in Fig. 4.7. The

slopes of linear fits of these data determine the power of $\frac{\partial B}{\partial z}$. Theoretically, it would be -0.5 in the temperature limited regime. The log-log plot of the data actually shows two different slopes on each dimension, the z-dimension being less noticeable. These two parts on the xy-dimension are fitted separately using linear fit and the slopes are found to be -0.59 and -0.22. This change suggests a transition from the temperature limited regime to the multiple scattering regime as the gradient increases. The critical value the gradient is mentioned in Section 2.4.1 although it is not possible to predict the exact value. The reduction in slope suggests a modification in the trapping force which governs the size of the cloud.
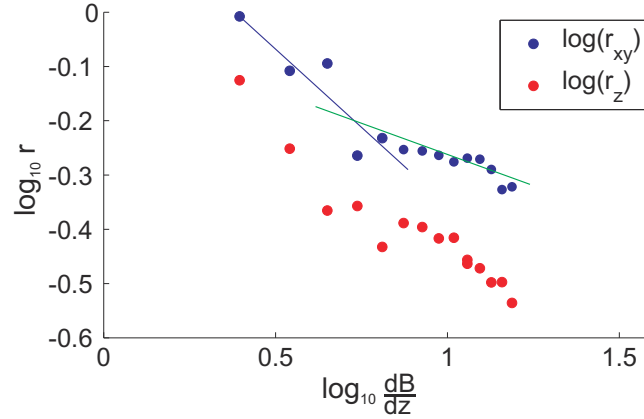
Figure 4.7: Cloud radii as a function of field gradient, plotted using logarithmic values. The blue dots are the radii in the xy-dimension. The red dots are the ones in the z-dimension.

Cloud temperatures were also measured in a changing magnetic field gradient. The gradient theoretically should have no effect on the temperature. This is because the theory is derived from the cooling force only and should work well with small atomic clouds that reside at the center of the trap where the magnetic field is small. Therefore, the scaling of temperature with gradient stated in Eq. (2.50) is related to the temperature limited regime. When the cloud becomes larger, such as when it transitions into the multiple scattering regime, the effect of the magnetic field gradient will appear. Vorozcovs *et. al.* [43] has reported such an observation where the temperature is found to rise

with gradient below 1 G/cm until it reaches a plateau. At very high gradients such as used in Ref. [44], the effect is reversed; i.e., the temperature drops because of the reducing trap depth. These effects are discussed in more detail in Section 2.4.1.

An increase in temperature with gradient was observed as shown in Fig. 4.8 at a trapping beam intensity of 4.4 mW/cm^2. At a higher trap intensity of 15 mW/cm^2, which implies stronger cooling and trapping forces, the trend over all the data in Fig. 4.9 is a small reduction of -3.3 μK $\cdot$ cm/G in the xy-dimension and -0.73 μK $\cdot$ cm/G in z-dimension. With the possibility of other parameters (laser detuning, trapping beam intensity, etc.) changing slowly at the same time it is impossible to conclude that such a small trend is due to the change in gradient only. The temperature can be said to show no change over the range of investigated gradient.
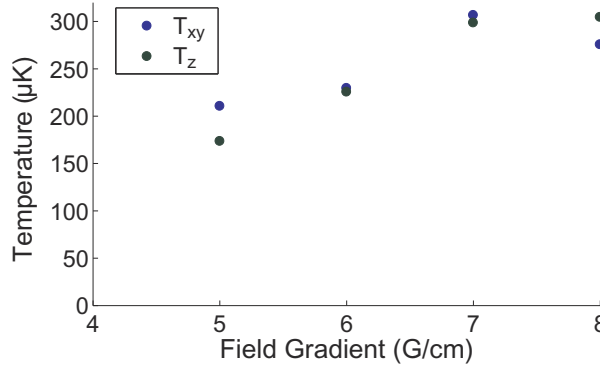
Figure 4.8: Cloud temperatures as a function of field gradient for $I = 4.4$ mW/cm^2. The blue dots are the temperature of the xy-dimension and the green dots are the temperature in the z-dimension. The trends show an increase in temperature with magnetic field gradient.

The intensities used here are lower than typically reported for MOT where a total intensity is often as high as 100 mW/cm^2 or even above. Therefore, the friction coefficient α in our setup will be different from those reported. The spring constant is also directly proportional to α. At the total intensity of 100 mW/cm^2, α is ~ 1.5 times of that at the total intensity of 26.4 mW/cm^2. The scaling of κ in Fig. 4.9 is therefore faster than in
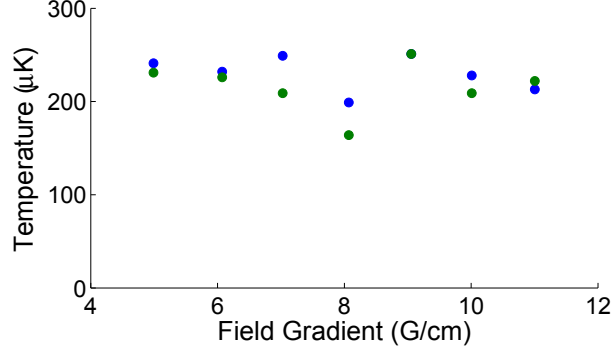
Figure 4.9: Temperatures of the cloud with field gradient for 15 mW/cm^2. The blue dots are the temperatures in the xy-dimension and the green dots are the temperatures in the z-dimension. The trend over all the data is a small reduction of $-3.3\ \mu K \cdot cm/G$ in the xy-dimension and $-0.73\ \mu K \cdot cm/G$ in z-dimension. In light of other fluctuations, this trend can be dismissed, and the temperatures can be concluded to show no change with magnetic field gradient over this range.

Fig. 4.8 where the increase in temperature is not observed.

4.4 Trap Compression

According to Eq. (2.47) and Eq. (2.49), the density of the atomic cloud will continue to increase with magnetic field gradient. This does not take into account the reduction of the trap depth which results in loss of atoms. The trap can end up small – with only a few atoms – but dense, and this will limit the number of atoms participating in atom-light interactions. The way to increase the atomic density while still retaining a high number of atoms in the trap is to transiently compress the atomic cloud.

The procedure starts with trapping atoms at low gradient, in our case around 10 G/cm, as our trap does not allow us to go much lower without losing the cloud altogether. Once the trap reaches steady state, it is temporarily compressed by increasing the magnetic field gradient. This procedure has been reported to heat up the cloud and cause significant loss in the number of atoms. In Ref. [25], the trap is red-detuned further to counter the heating and the loss which I also investigate.

79

In this experiment, the initial detuning for the trap is -8.3 MHz, the trap intensity is 6.3 mW/cm^2 per beam, and the initial field gradient is 10 G/cm. After the trap has reached the steady state, the coil current is increased in five equal steps for 2 ms each before it is held at the maximum value for a set period of time, generally tens of milliseconds. The trap is then reverted back to its original condition. The highest field gradient currently achievable in the setup is 35 G/cm which is much lower than the 228 G/cm in Ref. [25]. Although the condition is more similar to the setup in Ref. [47], it must be noted that they implement the compression on a dark MOT while here it is a regular MOT, and therefore the parameters and results cannot be directly compared.

The data regarding the number of atoms and the cloud size are taken every 2 ms, starting 5 ms after the compression sequence begins (t=0). First, I investigate the effect of increasing red-detuning on the atomic density during the compression sequence as implemented by Petrich *et al.* [25]. The field gradient is increased to 30 G/cm and held there for 50 ms. At this gradient, there is no transient increase in the atomic density. The data in Fig. 4.10 show that the increase in red-detuning does not affect the atomic density. The number of atoms during trap compression, however, decreases with increasing red-detuning (Fig. 4.11). Therefore, at a gradient of $\sim$30 G/cm, increasing the red detuning is not beneficial in terms of increasing the atomic density or preserving the number of atoms. The detuning is thus kept constant in the later part of the experiment.

The change in number of atoms and cloud size with time is recorded for different compression gradients. The result in Fig. 4.12 shows a 1.6 fold increase in atomic density compared to the final density at a gradient of 35 G/cm. The density peaks at $\sim$15 ms after the trap reaches the compression gradient which is roughly 25 ms after the compression sequence started. After repeating the experiment on a later date, it became apparent that the time it takes for the atomic density to reach its peak is not always the same and depends to some extent on the trap forces. One of the repeats is done at a trapping
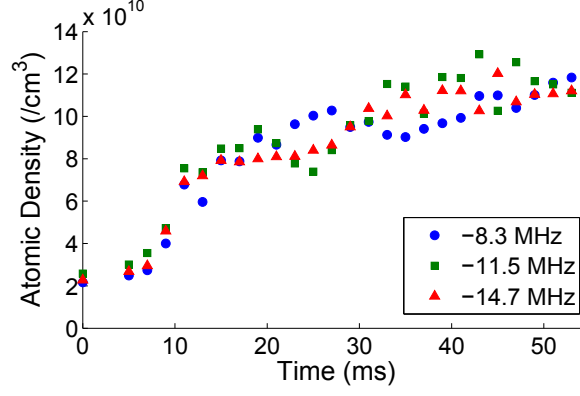
Figure 4.10: Atomic densities after the start of the compression sequence. Different data sets correspond to different detunings. The final gradient is 30 G/cm.
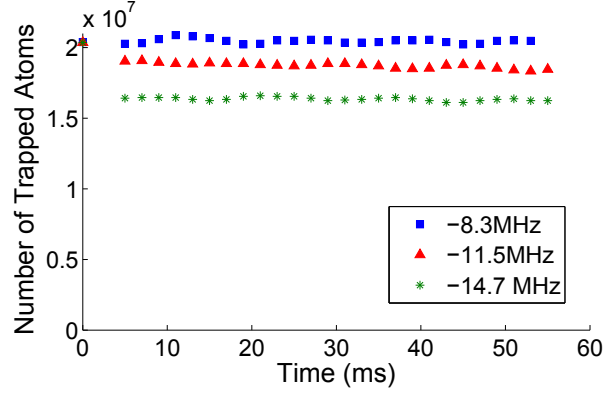
Figure 4.11: The number of atoms measured for the same initial condition but at different detunings during compression. The final gradient is 30 G/cm.

beam intensity of 7.4 mW/cm^2 per beam, and the peak time is $\sim$7 ms after the trap reaches the final gradient. This suggests that the peak occurs faster with stronger forces. However, a model has not yet been developed to predict the time and transient increase of atomic density.

One explanation as to why there is a transient increase or a delay is in the fact that the atoms are very slow at these temperatures, and therefore there is a lag times for the cloud to respond to the change in trapping force. By increasing the spring constant through increasing the field gradient, the force of the harmonic trap at a particular distance becomes stronger and pulls the atoms towards the center of the trap. This will increase the density once all the atoms come to the center of the trap. However, there
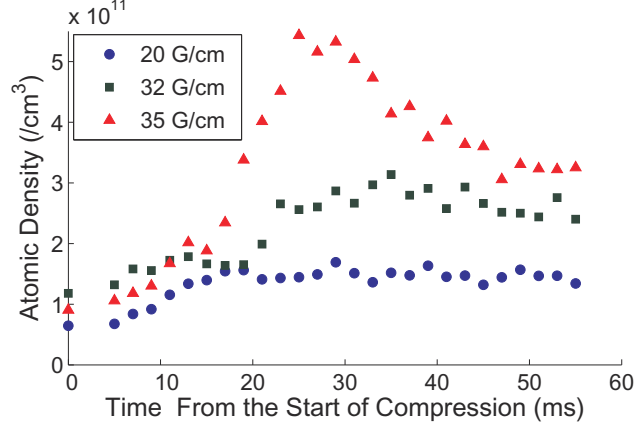
Figure 4.12: Atomic densities after the start of the compression sequence. Different data sets correspond to different magnetic field gradients.
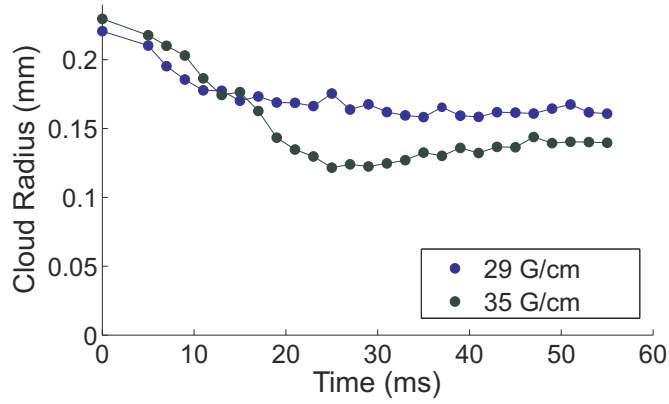
Figure 4.13: Atomic cloud radii after the start of the compression sequence. The blue dots are the cloud radii where no transient increase in density is observed. The green-dot set has a transient increase at the dip in radius.

is a density limit which a steady state trap can maintain. If this limit is not reached, the trap will be able to maintain the new density. However, if the density becomes too high for the trap, the trap cannot support the density and a reduction will occur either from a reduction in trap depth, an extra repulsive force such as photon-pressure force, collisional loss, or all processes combined. This process creates the observed transient peak. The time scale of the delay can be roughly estimated by inferring the mean velocity of the atoms. If the cloud has a temperature of $\sim$130 μK and a radius of 0.23 mm (as in the datum of the trap before compression, presented at time 0 in Fig. 4.13), the time of

flight required to get from one end of the trap to the center without cooling or colliding is 1.5 ms. This will be the fastest possible time since the motion of the atom is actually random due to the random kicks from fluorescence photons. This estimation also ignores any forces that might act on the atom during its travel.

Figure 4.13 shows the change in the cloud radius during the compression process. The data set which shows transient compression also shows a dip in the cloud radius when the transient compression occurs. This hints at a repulsive force acting to reduce the cloud density. Therefore, the reduction in atomic density after the transient peak is not just the effect of losing atoms but also from the increase in cloud size. This feature suggests that the transient increase in atomic density occurs in the multiple scattering regime where the photon-pressure force limits the atomic density in steady state. The dip in cloud radius can also be used to predict when the atomic density will reach its peak in the compression process although software must first be developed to estimate the size of the cloud in real time.

The temperature change due to trap compression is also investigated. The magnetic field gradient of 10 and 26 G/cm are used as initial and final gradients, respectively, with a trapping beam intensity of 6 mW/cm^2 on the z-axis and 6.8 mW/cm^2 in the xy-direction. The initial detuning is -8.3 MHz but is set to be shifted to -14.7 MHz at the start of the compression sequence. The data are taken 20 ms after the trap condition is held constant, which is 30 ms after the compression sequence start. This is roughly the time where the atomic density reaches its peak.

T	10 G/cm	26 G/cm	w/o detuning	w/ detuning
T_{xy} (μK)	176	137	173	132
T_z (μK)	203	161	194	164

Table 4.1: Comparison of cloud temperatures with no compression (first two columns) and with compression (last two columns).

Table 4.1 shows the results of the study. The first two columns are the tempera-

tures for the steady state trap at different gradients. The trap at 26 G/cm shows lower temperature suggesting a reduction of trap depth. These results are used as a baseline for the last two columns which are the temperatures from the compressed trap. The compression with and without an increase in red-detuning is compared with its steady state counterpart. I find that without detuning, the temperature does not significantly change from its initial temperature. Once an increase in red-detuning is applied, the temperatures significantly drops. The decrease of temperature with an increase in red-detuning is already known from the steady state trap. This is because the increase in red-detuning reduces the scattering force and therefore the trap is able to trap slower atoms compared to when the detuning is closer to resonance. For compressed MOT, the red-detuning also provide compensation to the larger Zeeman shift due to the increase in gradient. In our experiment, the gradient does not increase enough to make the increase red-detuning a necessity. Figure 4.14 shows the change in temperature with increase of red-detuning during the trap compression.
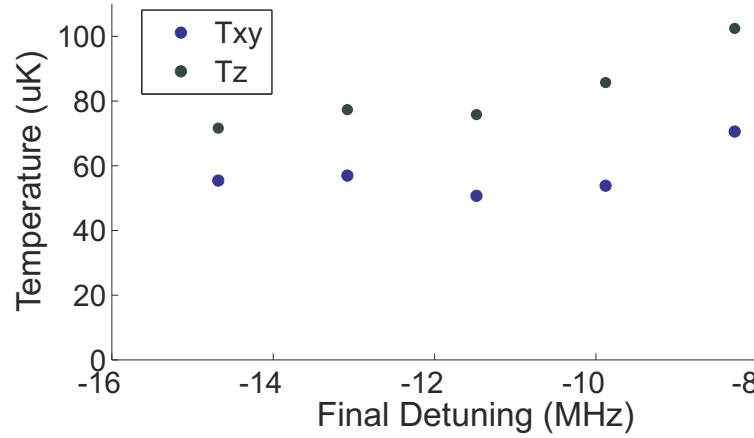
Figure 4.14: Temperatures of the compressed cloud with detuning 30 ms after the compression sequence starts.

The ratio of the number of atoms participating in the atom-light interaction around a tapered nanofiber, as described in Chapter 1, can be found using Eq. (1.1). The ratios

from the experimental data are $\frac{n_2}{n_1} = 1.7$ and $\frac{r_2}{r_1} \approx \frac{1.2}{1.4}$ (from the 35 G/cm data in Fig. 4.13). The ratio of the number of atoms interacting with the evanescent field is then

$$\frac{N_2}{N_1} = 1.5. \tag{4.2}$$

This is an increase from the number of atoms obtainable in steady state. However, it should be noted that the increase in density alone does not translate to an increase in participating atoms in a straightforward manner. The change in the cloud radius must be taken into account as it is also a factor in this model. A dramatic increase in atomic density might not be beneficial if it also leads to a dramatic decrease in cloud radius as well.

4.5   Translation

The general method for translating a MOT cloud is to modify the magnetic field so the zero-point is shifted. In this experiment, a shift along the coil axis is achieved by introducing a small current imbalance into the anti-Helmholtz coils. The current imbalance is a few percent of the balanced current in one coil. I have calculated the field gradient and found it to change only slightly within the first 10% of introduced imbalance which at least guarantees that the trap condition will not be drastically changed by the change in current. This restriction on the current imbalance will also limit how far we can shift the cloud. For a gradient of 10 G/cm, a 10% imbalance results in a 3 mm shift. Considering that a large cloud has a diameter of around 1 mm, this will allow the formation of the cloud at a reasonable distance from a tapered nanofiber.

The simulation of the magnetic field gradient predicts a linear translation of the magnetic field zero-point. This is verified by tracking the translation of the cloud after 10 ms of stepwise ramping and 20 ms of holding the trap parameters. With a trapping beam intensity of 6.3 mW/cm^2 per beam and a coil current of 8 A per coil, a current

imbalance up to 5% is introduced. Linear translation is observed in both z and xy directions (Fig. 4.15(a)). This three dimensional movement is because the coils are not perfectly on axis with one another.
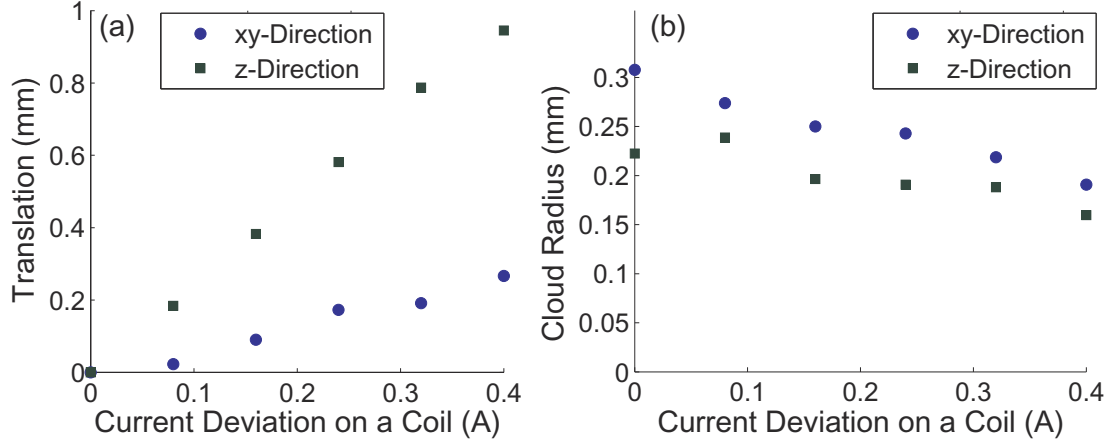
Figure 4.15: (a) Cloud radii and (b) positions as function of current imbalance.

Translation does not change the number of trapped atoms noticeably until a 10% current imbalance is introduced. The cloud can either gain or lose atoms due to translation. The change in number of atoms is due to the change in trap condition since the intensity profile of the trapping beams are not perfectly uniform. This can also contribute to a fluctuation in temperature and a change of cloud shape with the position of the cloud. The cloud shape can be improved by small adjustments in the alignment of the trapping beams, although it will also affect the shape of the cloud before the translation. The setup has to be optimized for a good compromise between both positions in terms of shape and number of atoms.

For the particular set of data in Fig. 4.15(b), the trap radius decreases while the number of atoms remains constant, suggesting that compression occurs with the translation. Cases where expansion occurs are also observed before the optimization process. This observation suggests a possibility of using the translation process to increase the atomic density during the cloud transfer, although the outcome is less predictable than using

magnetic compression.

Chapter 5

Conclusion and Outlook

Magneto-optical trapping, despite being a standard technique for producing a cold atomic cloud, is subject to many parameters that make quantitative comparison between different MOT setups difficult and not always insightful. Therefore, it is necessary for each research group to characterize the properties of the atomic cloud from their MOT before further experiments can be performed. There are theoretical explanations for the behavior of a steady state MOT cloud that can be used semi-empirically to predict the response of the cloud to a change in any of its major parameters: the trap intensity, the trap detuning, the magnetic field gradient, and the number of atoms.

The goal of my investigation is to obtain a cold and dense atomic cloud for experiments in atom-light interaction. The temperature of the cloud is related to the average velocity of the atoms in the ensemble. Slower atoms will take more time to escape from the laser beams intended for atom-light interaction and therefore allow coherent evolution to persist over a longer time. The strength of atom-light interaction increases with the number of atoms participating in the process. We are interested in interfacing a MOT cloud with evanescent fields from a tapered nanofiber with a penetration depth of about a wavelength. For this study, atomic density is a more relevant parameter than the total number of atoms in the cloud. Current investigation has been aimed at finding how low a temperature is attainable and finding techniques to increase the atomic density while retaining that temperature.

In this thesis, I investigate the effects that the trapping parameters have on the properties of a steady state atomic cloud. The atomic cloud is most likely to be in either the temperature limited regime or the multiple scattering regime. These two regimes are

distinguished by the existence of a repulsive force between atoms. This force is a result of having high probability of re-scattering photons, limiting the atomic density obtainable. In the multiple scattering regime, the atomic density does not depend on the number of atoms. In the temperature limited regime, however, where this force is negligible, the cloud density increases with the number of atoms. The loading of atoms is controlled using the trapping beam intensity. I observe an increase in atomic density with number of atoms up to about 30 mW/cm^2, after which the atomic density reaches a peak as predicted by the theory of the multiple scattering regime. The atomic density observed in our experiment does not remain constant over large changes in intensity but decreases after reaching a plateau where the cloud transitions into the multiple scattering regime. This is a result of increasing the re-scattering rate by increasing the number of photons being scattered, thus confirming that the cloud can transition between the two regimes in our setup, provided that appropriate parameters are used. This also shows us that the atomic density of a steady state cloud is limited by what is obtainable in the multiple scattering regime.

The temperature of the cloud is measured and found to increase with trap intensity. A temperature below the Doppler limit of 146 μK is observed at an intensity of 30 mW/cm^2. Since the atomic density and the temperature are interconnected in the steady state, it is impossible to control them separately.

A way to increase the atomic density to beyond the steady state limit in the multiple scattering regime is to transiently compress the cloud. The effect of the compression is investigated and found that the temperature after the compression does not change significantly from its initial temperature. The lack of heating is likely due to the small gradient used in my experiment, which goes up to 35 G/cm. This is rather small compared to the final gradient reported by Petrich *et. al.* [25] at 228 G/cm, which results in heating of the trap. There is a loss of atoms associated with trap compression, but the degree

varies from day to day, most likely from small shifts in the beam alignment or in the intensity profile which leads to changes in the trapping conditions. The temperature can be reduced by red-detuning the trapping beam while compressing as shown in Table 4.1, although this does not appear to help in reducing the loss of atoms. The most significant results of this study show that transient compression does not always occur, and that atomic density does not always peak at the same time for repetitions of the experiment from day-to-day. There is a possibility of determining almost in real time when the atomic density peaks by looking at the change in cloud radius, but a program tho track the cloud size must first be developed. The data with the transient increase in density shows a distinct dip in radius with the minimum radius occurring at the same time as the density peak.

The translation of the cloud is achieved by introducing a current imbalance in the magnetic coils. As verified through simulation, for a current imbalance of less than 10% of the balanced value, the magnetic field gradient around zero-point changes very little. The zero-point is verified through experiment to shift linearly with the current imbalance as predicted by the simulation. However, due to the non-uniformity of the intensity profile of the trap beams, the trapped cloud can exhibit changes in shape and number of atoms. While generally the number of atoms in the trap changes very little, often not significant enough to be detected below the current imbalance of 10%, the change in the shape of the cloud can be drastic, resulting in either expansion or compression at the end of the translation.

To assess the usefulness of these results for an atom-light experiment, we need to consider the details of the planned experiment. The next stage of the experiment is to incorporate a tapered nanofiber into the MOT setup and observe an EIT signal from the fiber modes. The change in the fiber's transverse area adiabatically reduces the size of the guided mode that results in an increase in intensity on the order of 10^4 times that

of the input intensity. Therefore, the optical nonlinearity can be greatly enhanced. Our goal is to implement the scheme for cross-phase modulation as purposed by Schmidt and Imamoğlu [13] which uses an EIT system scheme to reduce light absorption.

This fiber will be prepared in the nanophotonics lab led by Dr. Paul Barclay. The aimed waist at this stage is 500 nm, smaller than the wavelength intended to use in the EIT experiment which is 780-795 nm. In this regime, the propagation modes through the fiber will exhibit an evanescent field surrounding the tapered region. To obtain an estimation of the cloud temperature needed, we consider the worst case scenario. Here, an atom moves on the shortest path between the fiber surface and the edge of the evanescent field (not meticulously defined here, but it can be considered as the distance where the intensity is $1/e$ of that at the fiber surface). Since our wavelength is about 1.5 times the fiber diameter, the evanescent field will not penetrate very far. Let's assume that the field exists in a diameter that is about the same size as the wavelength in which the penetration depth for ~ 800 nm wavelength will be about 150 nm. The coherence time of a quantum information process with atoms has a fundamental limit of about a microsecond due to spontaneous emission that interrupts coherent evolution. The velocity that would take an atom to the edge of the light field during this time period is 0.15 m/s, which corresponds to a temperature of ~ 120 μK. This is below the Doppler limit that I have achieved in the setup. Therefore in terms of temperature, the result from our cloud is satisfactory. The transient increase in atomic density that I achieved is 1.7 times that of the steady state. An estimation is done in Section 4.4 to provide an idea of how this would translate into the increase in number of atoms participating in a future experiment. An increase of 1.5 times the steady state is estimated. Due to limitations on the coil currents, this is the best I can obtain from the current setup.

The ultimate test is to experimentally interface the atomic cloud with the tapered nanofiber and measure the difference in absorption between the compressed and steady

state cloud to estimate the actual increase in number of atoms. A part of my work in my Master's program is in preparing the setup for the future experiment.

To be able to insert a fiber into the vacuum chamber, another MOT setup has been designed to accommodate the fiber system. The fiber bracket, first designed by Mirko Lobino – a previous post-doctoral fellow in the lab – is re-examined and modified for the new vacuum chamber along with a fiber feedthrough [57]. The system is tested for leaks and found to consistently maintain a pressure below 10^{-8} Torr. Major leaks, if any, come mainly from the feedthrough which is suspected to be significantly deformed under a high pressure difference. These leaks can be sealed by tightening the nut around the feedthrough, but this will limit the number of times the feedthrough can be reused, and several duplicates of the piece has been made.

The pulling of the tapered nanofiber is still underway as the pulling system needs to be optimized for pulling down to a waist of a micron. The parameters for this step of pulling are generally kept constant for the entire pulling process which has been reported to be highly repeatable [58]. To the best of my knowledge, the parameters currently used only guarantee a pulling down to roughly a few microns. The goal is to have a 500 nm fiber – this has not been proven to be obtainable with the current pulling algorithm. The LabVIEW program controlling the pulling has now been modified to be able to instantaneously switch between two sets of parameters to follow the two-step algorithm done by Nayak [27]. These parameters are not yet optimized for a repeatable process.

Another mechanical setup has been designed and assembled for transferring the tapered nanofiber onto the bracket and into the vacuum chamber. Exposure to moisture and dust has to be taken into consideration in the experiment since it can lead to heating and melting of the fiber once optical field is injected. This is a result of low heat conduction in vacuum and high intensity of the light field around the tapered region. To keep the exposure to air after the pulling at a minimum, a metal box is modified

so that the bracket can be attached to its lid and the lid is then attached to a set of translational stages. The design allows the lid to be quickly removed from the pulling stage and attached to the box. Dismounting the bracket from the lid will need to be done in a clean box which has yet to be set up.

In the implementation of a giant optical nonlinearity, we would need to interface the atomic cloud with a field containing a few photons. The challenge would be to distinguish between signals that are gigahertz apart and are at intensities of a few photons, especially when they are copropagating along a tapered nanofiber. One way of doing so is to use a cavity filter which can be designed to have a transmission linewidth in order of tens of MHz and a high extinction ratio to ensure the authenticity of the signal. This is most often done by assembling a spherical Fabry-Perot cavity from two separate pieces of mirror, often one with a curved surface and one with a flat surface (hemispherical cavity). This design, however, needed to be stabilized by an additional optical signal which adds significant noise to a system with only a small signal to work with. On the other hand, there are etalons, cavities built often from a single substrate with two flat mirror surfaces (coplanar cavity). These are typically designed for high mechanical stability without the need for any optical locking signal. However, the coplanar geometry limits the extinction ratio obtainable from this design. To achieve both mechanical stability and high extinction ratio, we designed a monolithic cavity filter built from a single substrate with one curved mirror surface, mimicking the design of hemispherical Fabry-Perot cavity. I have characterized one of these cavities which has an extinction ratio of 45 dB, a full-width-half-maximum of ~ 80 MHz, and a peak transmission of 60%. These are suitable characteristics for a filter to be used in the atom-light experiment which often has narrow linewidth of tens of MHz. The detail of the design and the characterization are published in Ref. [59].

Now the characterization of the MOT within the parameters of our setup is completed.

The steady state MOT and the compressed MOT both show expected behaviors similar to what is reported previously in the literature, although the clouds are in different parameter space. Methods of controlling the atomic density and temperatures of the cloud have been investigated. Any further investigation would involve modification of the current setup either to provide higher cooling and trapping forces or to include the tapered nanofiber. This will be left to future students who and hopefully we will see the enhancement in optical nonlinearities that are anticipated.

Appendix A

Atom-Light Interaction

In order to derive the force on the atoms inside a magneto-optical trap, we first need to understand how light and atoms interact and how this interaction results in forces on the atoms. From a quantum mechanical point of view, the interaction between light and atoms can be summed up as interchanges of energy quanta. An atom gains a quantum of energy by absorbing a photon and transitioning to a higher energy state, or it loses energy by emitting a photon and transitioning to a lower energy level. The energy of the photon will be that of the energy gap between the two levels. The photon also carries a momentum of $\hbar\mathbf{k}$ which changes the atomic momentum after the interaction. This means that the interaction with photons, aside from changing the internal atomic state, also changes the atomic momentum. In this appendix, I will give a brief description of the atomic structure, the change of the atomic state under the influence of an external field, and the force on the atom due to a light field.

A.1   Brief Review of Atomic Structure

In the simplest case, the atom is assumed to be an alkali atom; i.e. there is only one valence electron. Electrons in other energy states are assumed to shield the effect of most of the protons in the nucleus, leaving what is effectively equivalent to a Hydrogen atom. A discussion on the energy levels of Hydrogen atoms can be found in various textbooks on atomic physics. The following discussion will be a summary of the one given in Ref. [31].

The energy levels are affected by spin-orbit ($\hat{\mathbf{L}} \cdot \hat{\mathbf{S}}$) coupling which arises from the electron moving inside the electric field from a proton. This electron experiences an

effective magnetic field which causes the energy levels of different spin states to become non-degenerate. The energy structure from this interaction is called the fine structure which is labeled by $\hat{\mathbf{J}} = \hat{\mathbf{L}} + \hat{\mathbf{S}}$ indicating the electron's total angular momentum. There is also the hyperfine structure arising from the interaction between the nuclear magnetic moment and the magnetic field generated by the electron, which is a coupling between $\hat{\mathbf{I}}$, the nuclear spin, and $\hat{\mathbf{J}}$. The hyperfine levels are labeled by $\hat{\mathbf{F}} = \hat{\mathbf{I}} + \hat{\mathbf{J}}$, which is also an angular momentum.

In literature involving alkali atoms, the atomic state is synonymous with the state of the valence electron. A more careful distinction is required if the atoms have more than one valence electron.

A.2 Internal State Evolution from Atom-Light Interaction: Semi-Classical Model

The energy exchange between an atom and a photon results in the transition of the atom into a different energy level. In this simple model, the atom has two energy levels: the ground state $|g\rangle$, being the lower energy level, and excited state $|e\rangle$. These two levels are separated by an energy gap of $\hbar\omega_0$. To follow the derivation in Ref. [60], the state of the atom can be represented as a density matrix

$$\hat{\rho} = \begin{pmatrix} \rho_{ee} & \rho_{eg} \\ \rho_{ge} & \rho_{gg} \end{pmatrix} \tag{A.1}$$

where ρ_{ii} is the population of the i state, and ρ_{ij} represents the coherence between state j and state i. Hence, ρ_{ij} and ρ_{ji} must be complex conjugates.

When the optical power is much higher than that of a few photons, the light field can be described as classical electromagnetic wave $\mathbf{E} = \vec{\mathcal{E}}_0 \cos(\omega t - kz)$ where $\vec{\mathcal{E}}_0$ is the slow-varying amplitude with its vector defining the polarization of the wave. Since an

atom is much smaller than a wavelength, we can apply the dipole approximation where the amplitude of the wave is taken to be constant in space and therefore we only need to consider the waveform in time. This allows us to describe the electromagnetic wave as

$$\mathbf{E} = \frac{\vec{\mathcal{E}}_0}{2} \exp\{-i\omega t\} + \frac{\vec{\mathcal{E}}_0}{2} \exp\{i\omega t\} \tag{A.2}$$

In the absence of the atom-light interaction, the Hamiltonian of the atom is

$$H_0 = \frac{\mathbf{p}^2}{2m} + \hbar\omega_0 |e\rangle\langle e| \tag{A.3}$$

As of now, we are only interested in the internal degree of freedom, and therefore the momentum term can be ignored. The atom-light interaction is included into the system by adding the Hamiltonian

$$\hat{H}^{(\mathrm{I})} = -\hat{\mathbf{d}} \cdot \mathbf{E}(t). \tag{A.4}$$

The derivation of this Hamiltonian from classical electromagnetism can be found in Ref. [61]. The elements in the dipole operator $\hat{\mathbf{d}}$ are governed by the selection rules. Since it is impossible for an atom to go through the interaction and still remain at the same state, the dipole operator cannot have diagonal elements. The operator in matrix form is

$$\hat{\mathbf{d}} = \begin{pmatrix} 0 & d \\ d^* & 0 \end{pmatrix} \tag{A.5}$$

The matrix elements signify the transition of the atom to another state. Since $|e\rangle\langle g|$ and $|g\rangle\langle e|$ are complex conjugates of one another, the matrix elements for these two transitions are also complex conjugates.

With a time-dependent interaction term, obtaining the population dynamics is not straightforward. We can use either time-dependent perturbation theory or the interaction picture. If we want to consider a more general case where the ensemble of atoms can be in a mixed state, the calculation using the interaction picture in density matrix

97

formalism is a more straightforward method. However, we will look into the solution from time-dependent perturbation theory, as can be found in Ref. [31], to simplify the calculation. The solution is shown to depend on the detuning $\Delta = \omega - \omega_0$, which is the frequency difference between the light field and the resonant frequency of the atomic transition. Therefore, we will formulate the Hamiltonian in the interaction picture to show dependency on the detuning and not the absolute frequency by defining

$$
H_0 = \begin{pmatrix} \hbar\omega & 0 \\ 0 & 0 \end{pmatrix} \tag{A.6}
$$

$$
H^{(\mathrm{I})} = - \begin{pmatrix} \hbar\Delta & \mathbf{d} \cdot \mathbf{E} \\ \mathbf{d}^* \cdot \mathbf{E} & 0 \end{pmatrix} \tag{A.7}
$$

The Hamiltonian in the interaction picture can be found by using the unitary operator $\hat{R} = \exp\{\imath \hat{H}_0/t\hbar\}$ which in matrix form is

$$
\begin{aligned}
\hat{R} &= \mathbb{I} + \imath\hat{H}_0 t/\hbar + \frac{1}{2!}(\imath\hat{H}_0 t/\hbar)^2 + \dots \\
&= \begin{pmatrix} \exp\{\imath\omega t\} & 0 \\ 0 & 1 \end{pmatrix}
\end{aligned} \tag{A.8}
$$

This operator is applied to the total Hamiltonian $H_0 + H^{(\mathrm{I})}$. Since $\hat{R}$ commutes with $\hat{H}_0$, the final form of the system Hamiltonian in interaction picture is

$$
\begin{aligned}
\hat{H}_{\mathrm{I}} &= \hat{R}\hat{H}\hat{R}^\dagger \\
&= \hat{R}H^{(\mathrm{I})}\hat{R}^\dagger \\
&= - \begin{pmatrix} \hbar\Delta & \mathbf{d} \cdot \mathbf{E}\exp\{\imath\omega t\} \\ \mathbf{d}^* \cdot \mathbf{E}\exp\{-\imath\omega t\} & 0 \end{pmatrix} \tag{A.9} \\
&= - \begin{pmatrix} \hbar\Delta & \mathbf{d}/2 \cdot (\vec{\mathcal{E}}_0 + \vec{\mathcal{E}}_0\exp^{\imath 2\omega t}) \\ \mathbf{d}^*/2 \cdot (\vec{\mathcal{E}}_0\exp^{-\imath 2\omega t} + \vec{\mathcal{E}}_0) & 0 \end{pmatrix} \tag{A.10}
\end{aligned}
$$

Using the rotating wave approximation (RWA), the rapidly oscillating term in Eq. (A.10) is neglected due to it being averaged to zero. This is the equivalent of neglecting the high frequency term $\omega + \omega_0$ in the solution from time-dependent perturbation theory.

The direction of the dipole moment is taken to be the same as the polarization of the field. Therefore, the final form of the Hamiltonian in interaction picture is

$$\hat{H}_{\mathrm{I}} = - \begin{pmatrix} \hbar\Delta & \frac{d\mathcal{E}_0}{2} \\ \frac{d\mathcal{E}_0}{2} & 0 \end{pmatrix}, \tag{A.11}$$

assuming $d^* = d$ for simplicity. Defining $\tilde{\rho}$ as the density in the interaction picture, the equation for system evolution is

$$\begin{aligned} \frac{d\tilde{\rho}}{dt} &= \frac{\imath}{\hbar}\left[\tilde{\rho}, \hat{H}_{\mathrm{I}}\right] \\ &= \begin{pmatrix} \frac{\imath\Omega}{2}(\tilde{\rho}_{\mathrm{ge}} - \tilde{\rho}_{\mathrm{eg}}) & \frac{\imath\Omega}{2}(\tilde{\rho}_{\mathrm{gg}} - \tilde{\rho}_{\mathrm{ee}}) + \imath\Delta\tilde{\rho}_{\mathrm{eg}} \\ \frac{\imath\Omega}{2}(\tilde{\rho}_{\mathrm{ee}} - \tilde{\rho}_{\mathrm{gg}}) - \imath\Delta\tilde{\rho}_{\mathrm{ge}} & \frac{\imath\Omega}{2}(\tilde{\rho}_{\mathrm{eg}} - \tilde{\rho}_{\mathrm{ge}}) \end{pmatrix} \end{aligned} \tag{A.12}$$

where $\Omega = d\mathcal{E}_0/\hbar$.

Aside from the interaction driven by the external field, the atoms in excited state also spontaneously emit photons and decay to the ground state. This process is dictated by the broadband vacuum modes of the light field [29, 32]. These modes are collectively called the reservoir which also requires its own Hamiltonian. The evolution of the density matrix is therefore

$$\frac{d\rho}{dt} = \frac{\imath}{\hbar}[\hat{\rho}, \hat{H}_{\mathrm{Light}}] + \frac{\imath}{\hbar}[\hat{\rho}, \hat{H}_{\mathrm{Reservoir}}] \tag{A.13}$$

The second term in Eq. (A.13) is found to be [29]

$$\frac{\imath}{\hbar}[\tilde{\rho}, \hat{H}_{\mathrm{Reservoir}}] = \begin{pmatrix} -\tilde{\rho}_{\mathrm{ee}}\Gamma & -\tilde{\rho}_{\mathrm{eg}}\Gamma/2 \\ -\tilde{\rho}_{\mathrm{ge}}\Gamma/2 & \tilde{\rho}_{\mathrm{ee}}\Gamma \end{pmatrix} \tag{A.14}$$

which signifies the decoherence for each element of the density matrix. By including this,

the dynamic equations become

$$\frac{d\tilde{\rho}_{ee}}{dt} = -\frac{\imath\Omega}{2}\left(\tilde{\rho}_{eg} - \tilde{\rho}_{ge}\right) - \Gamma\tilde{\rho}_{ee} \tag{A.15}$$

$$\frac{d\tilde{\rho}_{gg}}{dt} = \frac{\imath\Omega}{2}\left(\tilde{\rho}_{eg} + \tilde{\rho}_{ge}\right) + \Gamma\tilde{\rho}_{ee} \tag{A.16}$$

$$\frac{d\tilde{\rho}_{eg}}{dt} = \left(\imath\Delta - \frac{\Gamma}{2}\right)\tilde{\rho}_{eg} + \frac{\imath\Omega}{2}\left(\tilde{\rho}_{gg} - \tilde{\rho}_{ee}\right) \tag{A.17}$$

$$\frac{d\tilde{\rho}_{ge}}{dt} = -\left(\imath\Delta + \frac{\Gamma}{2}\right)\tilde{\rho}_{ge} - \frac{\imath\Omega}{2}\left(\tilde{\rho}_{gg} - \tilde{\rho}_{ee}\right) \tag{A.18}$$

The simplest case for solving these equations is when the atom is in the steady state. By setting the left hand sides of Eq. (A.15) – (A.18) to zero and using an additional relation $1 = \tilde{\rho}_{gg} + \tilde{\rho}_{ee}$ indicating a total probability of unity, the elements are found to be

$$\tilde{\rho}_{ee} = \frac{1}{2}\frac{\Omega^2/2}{(\Gamma/2)^2 + \Delta^2 + \Omega^2/2} \tag{A.19}$$

$$\tilde{\rho}_{eg} = \frac{\Omega\left(2\Delta - \imath\Gamma\right)}{2\Omega^2 + 4\Delta^2 + \Gamma^2} \tag{A.20}$$

$$\tilde{\rho}_{ge} = \frac{\Omega\left(2\Delta + \imath\Gamma\right)}{2\Omega^2 + 4\Delta^2 + \Gamma^2} \tag{A.21}$$

The photon scattering rate per atom is given by the decay rate of the transition multiplied by the population in the excited state, which is the portion of the ensemble that can emit photons. Therefore, in the steady state, the scattering rate is

$$\mathcal{R}_{\text{scat}} = \Gamma\rho_{ee}$$

$$= \frac{\Gamma}{2}\frac{\Omega^2/2}{\Delta^2 + (\Gamma/2)^2 + \Omega^2/2} \tag{A.22}$$

$$= \frac{\Gamma}{2}\frac{I/I_{\text{sat}}}{1 + 4\Delta^2 + I/I_{\text{sat}}} \tag{A.23}$$

where I is the intensity and $I_{\text{sat}} = \frac{\pi}{3}\frac{\hbar c\Gamma}{\lambda^3} = 2\left(\frac{\Omega}{\Gamma}\right)^2$ is the saturation intensity of the transition. This results in the scattered power of $\hbar\omega\mathcal{R}_{\text{scat}}$. We can define the scattering cross section σ such that the scattered power is written as $I\sigma$, where I is the input

intensity. Therefore,

$$
\begin{aligned}
\sigma &= \frac{\hbar\omega\mathcal{R}_{\text{scat}}}{I} \\
&= \frac{\hbar\omega\Gamma}{2I_{\text{sat}}}\frac{1}{1+4(\Delta/\Gamma)^2+I/I_{\text{sat}}}
\end{aligned}
\tag{A.24}
$$

A.3   Light Force on an Atom

So far, we are only interested in the internal atomic states. The external degrees of freedom are also affected by the interaction due to the exchange of momentum between the photons and the atom. The formalism of the forces on atoms will follow that of Ref. [32], which is also similar to Ref. [62].

There are two kinds of forces in atom-light interaction: the dipole force due to an intensity gradient and the radiation pressure force due to scattering, which are reactive and dissipative forces. Although the dipole force can be treated purely classically with transparent objects, we will forgo the classical treatment for the semi-classical treatment with atoms which is more relevant to our problem. Since we are interested in atoms in motion, the dipole approximation has to be lifted as hot atoms can travel considerable distance (compared to an optical wavelength) in a short period of time.

In the Heisenberg picture, the evolution of the momentum operator follows the equation

$$
\frac{\partial\hat{p}}{\partial t} = \frac{\imath}{\hbar}[\hat{H}(\mathbf{r}),\hat{p}].
\tag{A.25}
$$

Since generally $\hat{H}(\mathbf{r})$ can be approximated to polynomial form, it is straightforward to show that $[\hat{H}(\mathbf{r}),\hat{p}] = \imath\hbar\nabla\hat{H}(\mathbf{r})$. This allows us to simplify the dynamic equation of the momentum operator to

$$
\frac{\partial\hat{p}}{\partial t} = -\nabla\hat{H}(\mathbf{r}).
\tag{A.26}
$$

The force on the atom which is a quantum particle is the average of the change in

101

momentum, leading to

$$\mathbf{F} = -\langle \nabla \hat{H}(\mathbf{r}) \rangle \tag{A.27}$$

The terms that are position dependent in our system are the terms involving the electromagnetic wave. For this problem, we define the field to be

$$\mathbf{E}(\mathbf{r}, t) = \frac{\mathcal{E}_0}{2} \exp\{-\imath(\omega t + \Phi(\mathbf{r}))\} + \frac{\mathcal{E}_0}{2} \exp\{\imath(\omega t + \Phi(\mathbf{r}))\} \tag{A.28}$$

The term $\Phi(\mathbf{r})$ signifies the phase due to change in position which for plane wave is $-\mathbf{k} \cdot \mathbf{r}$. Here, we do not assume a plane wave form for the purpose of generalization. The Hamiltonian of the system is

$$\hat{H} = \hbar\omega - \mathbf{d} \cdot \mathbf{E} \, |e\rangle\langle g| - \mathbf{d} \cdot \mathbf{E} \, |g\rangle\langle e| \tag{A.29}$$

It is possible to have coupling between the external degrees of freedom, such as position and momentum, and the internal degrees of freedom. In the MOT, where the internal degrees of freedom are in steady states, the internal and external degrees of freedom can be decoupled. To be able to use the steady state solution we obtained from the previous part, the Hamiltonian is transformed to the interaction picture and the RWA is used to obtain the force in the form:

$$\mathbf{F} = \frac{\hbar}{2} \langle |e><g| \rangle \langle \nabla \left(\frac{\Omega(\mathbf{r})}{2} \exp\{-\imath\Phi(\mathbf{r})\} \right) \rangle + \frac{\hbar}{2} \langle |g><e| \rangle \langle \nabla \left(\frac{\Omega(\mathbf{r})}{2} \exp\{\imath\Phi(\mathbf{r})\} \right) \rangle \tag{A.30}$$

where $\langle |e><g| \rangle = \mathrm{Tr}\,(\tilde{\rho}|e><g|)$ can be replaced by the steady state $\tilde{\rho}_{ge}$ from Eq. (A.21). After some rearrangement, the force is shown to be

$$\mathbf{F} = \hbar\Omega(\mathbf{r}) \left[\frac{\nabla\Omega(\mathbf{r})}{\Omega} \mathrm{Re}(\tilde{\rho_{ge}} \exp\{-\imath\Phi(\mathbf{r})\}) - \nabla\Phi(\mathbf{r})(\mathrm{Im}(\tilde{\rho_{ge}} \exp\{-\imath\Phi(\mathbf{r})\})) \right] \tag{A.31}$$

The first term is the dipole force which depends on the change in amplitude of the electromagnetic wave over space. The second term is the scattering force which depends on the change in phase over space, a property that happens for every traveling wave and

therefore is always present. This is the force that is responsible for the cooling in the MOT.

To find an explicit form, we make the assumption that $\Phi = -\mathbf{k} \cdot \mathbf{r}$. By exchanging $\tilde{\rho}_{\text{ge}}$ for $\tilde{\rho}_{\text{ge}} \exp\{-\imath\Phi(\mathbf{r})\}$ in the calculation for the internal state, we are able to find the steady state solution for the real and imaginary part of $\tilde{\rho}_{\text{ge}} \exp\{-\imath\Phi(\mathbf{r})\}$. This substitution is the same as applying the dipole approximation (as in the previous section). This gives explicit forms for the forces as follows:

$$\mathbf{F}_{\text{dipole}} = -\frac{\hbar\Delta}{4} \left(\frac{\nabla\Omega^2}{\Delta^2 + (\Gamma/2)^2 + \Omega^2/2} \right) \tag{A.32}$$

$$\mathbf{F}_{\text{scattering}} = \hbar\mathbf{k}\frac{\Gamma}{2} \left(\frac{\Omega^2/2}{\Delta^2 + (\Gamma/2)^2 + \Omega^2/2} \right) \tag{A.33}$$

The actual force per scattered photon is $\hbar\mathbf{k}\Gamma$ with the rest of the term being the probability of applying the force. The scattering force is in the same direction as the laser. This is because the momentum of the spontaneously emitted photons is random in direction and therefore is averaged to zero over time. The absorbed photons have the same direction and therefore cannot be averaged out.

Bibliography

[1] Steven Chu. Nobel lecture: The manipulation of neutral particles. *Rev. Mod. Phys.*, 70:685–706, Jul 1998.

[2] E. L. Raab, M. Prentiss, Alex Cable, Steven Chu, and D. E. Pritchard. Trapping of neutral sodium atoms with radiation pressure. *Phys. Rev. Lett.*, 59:2631–2634, Dec 1987.

[3] Paul D. Lett, Richard N. Watts, Christoph I. Westbrook, William D. Phillips, Phillip L. Gould, and Harold J. Metcalf. Observation of atoms laser cooled below the doppler limit. *Phys. Rev. Lett.*, 61:169–172, Jul 1988.

[4] A. Imamoğlu, D. D. Awschalom, G. Burkard, D. P. DiVincenzo, D. Loss, M. Sherwin, and A. Small. Quantum information processing using quantum dot spins and cavity qed. *Phys. Rev. Lett.*, 83:4204–4207, Nov 1999.

[5] Alexander I. Lvovsky, Barry C. Sanders, and Wolfgang Tittel. Optical quantum memory. *Nature Photonics*, 3:706 – 714, 2009.

[6] J. J. Longdell, E. Fraval, M. J. Sellars, and N. B. Manson. Stopped light with storage times greater than one second using electromagnetically induced transparency in a solid. *Phys. Rev. Lett.*, 95:063601, Aug 2005.

[7] M. A. Nielsen and I. L. Chuang. *Quantum Computation and Quantum Information*. Cambridge University Press, 2000.

[8] Hsiang-Yu Lo, Yen-Chun Chen, Po-Ching Su, Hao-Chung Chen, Jun-Xian Chen, Ying-Cheng Chen, Ite A. Yu, and Yong-Fan Chen. Electromagnetically-induced-transparency-based cross-phase-modulation at attojoule levels. *Phys. Rev. A*, 83:041804, Apr 2011.

[9] P. K. Lam and B. C. Buchler. Atom-light interactions: The nonlinearity of single photons. *Nat Photon*, 5:580–581, 2011.

[10] M. D. Lukin and A. Imamoğlu. Nonlinear optics and quantum entanglement of ultraslow single photons. *Phys. Rev. Lett.*, 84:1419–1422, Feb 2000.

[11] A. B. Matsko, I. Novikova, G. R. Welch, and M. S. Zubairy. Enhancement of kerr nonlinearity by multiphoton coherence. *Opt. Lett.*, 28(2):96–98, Jan 2003.

[12] D. J. Alton, N. P. Stern, Takao Aoki, H. Lee, E. Ostby, K. J. Vahala, and H. J. Kimble. Strong interactions of single atoms and photons near a dielectric boundary. *Nat Phys*, 7:159–165, 2011.

[13] H. Schmidt and A. Imamogdlu. Giant kerr nonlinearities obtained by electromagnetically induced transparency. *Opt. Lett.*, 21(23):1936–1938, Dec 1996.

[14] Julio Gea-Banacloche. Impossibility of large phase shifts via the giant kerr effect with single-photon wave packets. *Phys. Rev. A*, 81:043823, Apr 2010.

[15] Bing He, Andrew MacRae, Yang Han, A. I. Lvovsky, and Christoph Simon. Transverse multimode effects on the performance of photon-photon gates. *Phys. Rev. A*, 83:022312, Feb 2011.

[16] Jeffrey H. Shapiro. Single-photon kerr nonlinearities do not help quantum computation. *Phys. Rev. A*, 73:062305, Jun 2006.

[17] Jeffrey H. Shapiro and Mohsen Razavi. Continuous-time cross-phase modulation and quantum computation. *New J. Phys.*, 9:16, Jan 2007.

[18] K. P. Nayak, P. N. Melentiev, M. Morinaga, Fam Le Kien, V. I. Balykin, and K. Hakuta. Optical nanofiber as an efficient tool for manipulating and probing atomicfluorescence. *Opt. Express*, 15(9):5431–5438, Apr 2007.

[19] S. M. Spillane, G. S. Pati, K. Salit, M. Hall, P. Kumar, R. G. Beausoleil, and M. S. Shahriar. Observation of nonlinear optical interactions of ultralow levels of light in a tapered optical nanofiber embedded in a hot rubidium vapor. *Phys. Rev. Lett.*, 100:233602, Jun 2008.

[20] Fam Le Kien and K. Hakuta. Slowing down of a guided light field along a nanofiber in a cold atomic gas. *Phys. Rev. A*, 79:013818, Jan 2009.

[21] Fam Le Kien, J.Q. Liang, K. Hakuta, and V.I. Balykin. Field intensity distributions and polarization orientations in a vacuum-clad subwavelength-diameter optical fiber. *Optics Communications*, 242(46):445 – 455, 2004.

[22] Limin Tong, Jingyi Lou, and Eric Mazur. Single-mode guiding properties of subwavelength-diameter silica and silicon wire waveguides. *Opt. Express*, 12(6):1025–1035, Mar 2004.

[23] C. G. Townsend, N. H. Edwards, C. J. Cooper, K. P. Zetie, C. J. Foot, A. M. Steane, P. Szriftgiser, H. Perrin, and J. Dalibard. Phase-space density in the magneto-optical trap. *Phys. Rev. A*, 52:1423–1440, Aug 1995.

[24] E. A. Cornell and C. E. Wieman. Nobel lecture: Bose-einstein condensation in a dilute gas, the first 70 years and some recent experiments. *Rev. Mod. Phys.*, 74:875–893, Aug 2002.

[25] Wolfgang Petrich, Michael H. Anderson, Jason R. Ensher, and Eric A. Cornell. Behavior of atoms in a compressed magneto-optical trap. *J. Opt. Soc. Am. B*, 11(8):1332–1335, Aug 1994.

[26] John Weiner, Vanderlei S. Bagnato, Sergio Zilio, and Paul S. Julienne. Experiments and theory in cold and ultracold collisions. *Rev. Mod. Phys.*, 71:1–85, Jan 1999.

[27] Kali Prasanna Nayak. *Optical Nanofibers for Manipulating Atoms and Photons.* PhD thesis, University of Electro-Communications, Chofu, Tokyo, December 2008.

[28] Guillem Sague Cassany. *Cold atom physics using ultra-thin optical fibres.* PhD thesis, Rheinischen Friedrich-Wilhelms-Universitat Bonn, Bonn, Germany, 2008.

[29] Y. B. Band. Light and matter: Electromagnetism, optics, spectroscopy and lasers. chapter Chapter 9, Quantum-Optical Process, pages 294–318. John Wiley and Sons, 2006.

[30] D.A. Steck. Rubidium 87 d line data. 2001.

[31] C. J. Foot. *Atomic Physics.* Oxford University Press, 2005.

[32] P. Meystre. *Atom Optics.* Springer, 2001.

[33] J. Dalibard and C. Cohen-Tannoudji. Laser cooling below the doppler limit by polarization gradients: simple theoretical models. *J. Opt. Soc. Am. B*, 6(11):2023–2045, Nov 1989.

[34] P. J. Ungar, D. S. Weiss, E. Riis, and Steven Chu. Optical molasses and multilevel atoms: theory. *J. Opt. Soc. Am. B*, 6(11):2058–2071, Nov 1989.

[35] B. Sheehy, S-Q. Shang, P. van der Straten, S. Hatamian, and H. Metcalf. Magnetic-field-induced laser cooling below the doppler limit. *Phys. Rev. Lett.*, 64:858–861, Feb 1990.

[36] V. G. Minogin, M. A. Olshany, and S. U. Shulga. Laser cooling of atoms below the single-photon classical limit. *J. Opt. Soc. Am. B*, 6(11):2108–2111, Nov 1989.

[37] Klaus Mølmer. Friction and diffusion coefficients for cooling of atoms in laser fields with multidimensional periodicity. *Phys. Rev. A*, 44:5820–5832, Nov 1991.

[38] A. M. Steane, M. Chowdhury, and C. J. Foot. Radiation force in the magneto-optical trap. *J. Opt. Soc. Am. B*, 9(12):2142–2158, Dec 1992.

[39] K Berg-Sorenson, Y Castin, E Bonderup, and K Molmer. Momentum diffusion of atoms moving in laser fields. *J. Phys. B: At. Mol. Opt. Phys.*, 25:4195, 1992.

[40] D. W. Sesko, T. G. Walker, and C. E. Wieman. Behavior of neutral atoms in a spontaneous force trap. *J. Opt. Soc. Am. B*, 8(5):946–958, May 1991.

[41] B. R. Mollow. Power spectrum of light scattered by two-level systems. *Phys. Rev.*, 188:1969–1975, Dec 1969.

[42] C. D. Wallace, T. P. Dinneen, K. Y. N. Tan, A. Kumarakrishnan, P. L. Gould, and J. Javanainen. Measurements of temperature and spring constant in a magneto-optical trap. *J. Opt. Soc. Am. B*, 11(5):703–711, May 1994.

[43] Andrejs Vorozcovs, Matthew Weel, Scott Beattie, Saviour Cauchi, and A. Kumarakrishnan. Measurements of temperature scaling laws in an optically dense magneto-optical trap. *J. Opt. Soc. Am. B*, 22(5):943–950, May 2005.

[44] S. Yoon, Y. Choi, S. Park, W. Ji, J. Lee, and K. An. Characteristics of single-atom trapping in a magneto-optical trap with a high magnetic-field gradient. *J. Phys. Conf. Ser.*, 80(012046), 2007.

[45] Wolfgang Ketterle, Kendall B. Davis, Michael A. Joffe, Alex Martin, and David E. Pritchard. High densities of cold atoms in a *dark* spontaneous-force optical trap. *Phys. Rev. Lett.*, 70:2253–2256, Apr 1993.

[46] C. G. Townsend, N. H. Edwards, K. P. Zetie, C. J. Cooper, J. Rink, and C. J. Foot. High-density trapping of cesium atoms in a dark magneto-optical trap. *Phys. Rev. A*, 53:1702–1714, Mar 1996.

[47] Marshall T DePue, S Lukman Winoto, D.J Han, and David S Weiss. Transient compression of a mot and high intensity fluorescent imaging of optically thick clouds of atoms. *Optics Communications*, 180(13):73 – 79, 2000.

[48] A. Höpe, D. Haubrich, G. Müller, W . G. Kaenders, and D. Meschede. Neutral cesium atoms in strong magnetic-quadrupole fields at sub-doppler temperatures. *Europhys. Lett.*, 22(669), 1993.

[49] Z. Hu and H. J. Kimble. Observation of a single atom in a magneto-optical trap. *Opt. Lett.*, 19(22):1888–1890, Nov 1994.

[50] K. B. MacAdam, A. Steinbach, and C. Wieman. A narrow-band tunable diode laser system with grating feedback, and a saturated absorption spectrometer for cs and rb. *Am. J. Phys.*, 60:1098, December 1992.

[51] J. E. Debs, N. P. Robins, A. Lance, M. B. Kruger, and J. D. Close. Piezo-locking a diode laser with saturated absorption spectroscopy. *Appl. Opt.*, 47(28):5163–5166, Oct 2008.

[52] John David Jackson. *Classical Electrodynamics, Third Edition*. Wiley, 1998.

[53] T. Bergeman, Gidon Erez, and Harold J. Metcalf. Magnetostatic trapping fields for neutral atoms. *Phys. Rev. A*, 35:1535–1546, Feb 1987.

[54] Lucia Duca. Implementation and testing of a magneto-optical trap for neutral [8]7rb atoms for quantum information processing. Master's thesis, Alma Mater Studiorum - Universita' di Bologna, 2009.

[55] A. Colin Cameron and Frank A.G. Windmeijer. An r-squared measure of goodness of fit for some common nonlinear regression models. *Journal of Econometrics*, 77(2):329 – 342, 1997.

[56] K.F. Riley, M.P. Hobson, and S.J. Bence. *Mathematical Methods for Physics and Engineering, third edition.* Cambridge University Press, 2006.

[57] Eric R.I. Abraham and Eric A. Cornell. Teflon feedthrough for coupling optical fibers into ultrahigh vacuum systems. *Appl. Opt.*, 37(10):1762–1763, Apr 1998.

[58] Lu Ding, Cherif Belacel, Sara Ducci, Giuseppe Leo, and Ivan Favero. Ultralow loss single-mode silica tapers manufactured by a microheater. *Appl. Opt.*, 49(13):2441–2445, May 2010.

[59] Pantita Palittapongarnpim, Andrew MacRae, and A. I. Lvovsky. Note: A monolithic filter cavity for experiments in quantum optics. *Review of Scientific Instruments*, 83(6):066101, 2012.

[60] Alexander I Lvovsky. Elements of atomic physics. In *Nonlinear and Quantum Optics: Lecture notes*. http://qis.ucalgary.ca/quantech/673/notes/phys673notes.pdf.

[61] C. C. Gerry and P. L. Knight. In *Introductory to Quantum Optics*, chapter Chapter 4, Emission and absorption of radiation by atoms, pages 74–114. Cambridge University Press, 2005.

[62] G. Gilbert, A. Aspect, and C. Fabre. In *Introduction to Quantum Optics: From the Semi-classical Approach to Quantized Light*, chapter Chapter 8, Laser manipulation of atoms. From incoherent atom optics to atom lasers, pages 599–647. Cambrigde University Press, 2010.